Università
Ca'Foscari
Venezia

Master's Degree Programme in

Sustainable Chemistry and Technologies

Final Thesis

Ca' Foscari
Dorsoduro 3246
30123 Venezia

Characterization of ceramic biomaterials for dental implant applications

Supervisor
Ch. Prof. Giuseppe Pezzotti
Ch. Prof. Alvise Benedetti

Graduand
Michele Santini
Matriculation Number 850235

Academic Year
2018 / 2019

Abstract

Nowadays, zirconia is an attractive material in dental implant applications due to its high mechanical properties and natural white colour which make it the ideal candidate material for the production of strong and aesthetically attractive implants. However, in addition to its aesthetic and mechanical properties, zirconia is considered to be an inert biomaterial, therefore it has limited interactions with biological environments and has limited osseointegration. This characteristic has allowed the development of dental implants with modified surfaces, which speed up the osseointegration process but, at the same time, increase the possibility of peri-implantitis or the adhesion of bacteria on the surface and zirconia does not have antibacterial properties. Therefore, an alternative was proposed to reduce the above problem through the use of an active bioceramic material: silicon nitride. Specifically, a coating of silicon nitride was applied to the surface of zirconia, thus maintaining the mechanical properties of zirconia, but stimulating osteointegration and making the material antibacterial thanks to the properties of silicon nitride. Silicon nitride is a ceramic biomaterial that has bioactive effects, such as antibacterial properties and promotes cell proliferation, which cannot be obtained with oxide materials. In this work, concepts such as advanced ceramic materials, biomaterial and an analysis of the properties of Si_3N_4 and ZrO_2 were introduced first. Then the concept of bone tissue was introduced to give a detailed insight into the process of cellular osseointegration and defined the action of bacteria on dental prosthesis. In addition, the epidermal staphylococcal bacteria and human osteosarcoma (SaOS-2) cell lines that have been used for this work are described. Four types of samples were analysed: polished zirconia; rough zirconia; zirconia coated with silicon nitride and stoichiometric silicon nitride as positive control. First, the morphology and surface properties were evaluated through a pre-characterization of the samples, using spectroscopic and microscopic techniques such as: Laser microscopy, Raman, FT-IR, XPS, SEM and cross-sectional analysis. The results showed that silicon nitride coating is a biphasic composite in which Si_3N_4 hard particles are dispersed in a nano crystalline and/or amorphous silicon matrix. In addition, the coating led to an increase in surface roughness, increasing the possibility of interaction with biological tissues. Subsequently, the surfaces of the samples were treated in vivo with staphylococcus epidermidis bacteria to allow the study of antibacterial effect and with osteoblastic cells of the SaOS-2 line to stimulate cell proliferation.

Various biological and bacterial markers were used to allow in vivo characterization. Bacterial analysis was performed using Raman, Fluorescence microscopy and WST techniques, while the analysis of SaOS-2 cell lines was characterized using Fluorescence microscopy, WST, Raman and SEM techniques. Bacterial tests were performed after 12, 24, 48 hours of exposure and showed low antibacterial activity for all samples. This is a predictable characteristic in zirconia, which by nature has no antibacterial activity, while for the silicon nitride coated zirconia sample it is probably due to a low concentration of nitride on the surface of the sample. The tests with SAOS-2 solutions were performed after 10 days of exposure and led to the formation of bone tissue with high collagen maturity, high carbonate/phosphate ratios and good levels of tissue mineralization, but less cell proliferation than stoichiometric Si_3N_4. Bone tissue quality parameters measured with Raman spectroscopy were comparable to healthy human bone tissue.

Summary

Chapter 1

Introduction

A dental implant allows the rehabilitation of edentulous areas of the jaws by surgical insertion into the bone of a dental prosthesis. The first rudimentary dental implant ever found dates back to about 600 B.C. and was made from shell fragments embedded in the mandible, an example of the ingenuity of the Maya population. The Etruscans at about 500 B.C. used fragments of animal bone in substitution of missing teeth. The first uses of ceramic materials for making dental prostheses date back to the end of the 18th century. Until then, the most common prostheses were made of hippopotamus ivory or reused natural teeth. One example was George Washington who brought one of the first mobile dental implants that was made of lead and animal teeth. The main problem that were encountered was the rejection of the implant with the organism. For the implant to be successful, the external body and bone must fuse together through a process known as osseointegration. Later in 1952, an orthopaedic surgeon discovered the first boneintergration process with a titanium cylinder that had fused with the bone of a rabbit's femur. Then in 1965, Brånemark successfully inserted the first titanium dental implant into a human: the "modern implantology" [1] [2] was born. The success of the first titanium dental implant quickly led to a significant development of the process. In particular, today, a titanium alloy screw with a machined surface (rough or smooth or coated) is used, which helps to improve the osseointegration process. The favourable properties have made titanium the material of choice for dental implant applications. In fact, modern oral implantology is predominantly based on titanium due to its properties of high biocompatibility, favourable tissue response and adequate corrosion resistance. The main problem that were encountered was also good mechanical properties, such as a relatively high elastic modulus (Young's modulus), which allows good loading stress during mastication. All these features have made titanium implants with the longest traceable record of predictable clinical performance, with a cumulative success rate of 98.8% for 15 years [3] and an increase in implant types. Currently, 98% of the dental implants produced worldwide are titanium implants. Titanium, however, is

no longer considered a completely bio-inert material, but can be an allergen [4] [5] [6]. Indeed, high concentrations of titanium have been found in the vicinity of oral implants [7], in regional lymph nodes [8], in serum and in urine [9], which are potentially dangerous for the human body. In addition, the dark grey titanium implant is aesthetically unpleasant, there is also the problem of the taste of the metal [10] And, since some patients are allergic to specific metals, they require to be treated exclusively with dental implants without metal [11].

Today, the main features that allow a good implant, in addition to the osteointegration process, are: a prevention of bacterial adhesion that can cause perimplantitis with the progressive loss of bone and consequently of the prosthesis; resistance to mechanical stress; pleasant sensation in the mouth and good aesthetics. Zirconium oxide or "Zirconia" (ZrO_2) is among the most widely used ceramic biomaterials on the market today for the fabrication of fixed partial dentures and crowns [12]. The natural white colour of zirconium and its high mechanical properties make it the ideal candidate material for the production of strong and aesthetically attractive implants [13]. Technological development has allowed the introduction of new biomaterials, in particular advanced ceramic materials with metal-free properties and mechanical properties similar to those of titanium. Zirconium oxide or "Zirconia" (ZrO_2) is among the strongest ceramic biomaterials on the market today for the fabrication of fixed partial dentures and crowns [14] [15]. Zirconia at room temperature is stable in the monocline form, which has relatively low mechanical properties [16]. At temperatures above 1170 °C, the monoclinic zirconia transforms into the more compact tetragonal phase, which then, if not stabilized, disintegrates by cracking upon cooling. In order to maintain the integrity of tetragonal zirconia compounds, it is stabilized by the addition of oxides, thus avoiding t-m transformation during cooling [16]. Tetragonal zirconia at room temperature has a high fracture toughness which is associated with a stress-induced t-m transformation that hinders crack propagation. Nevertheless, the fracture toughness of zirconia is compromised in aqueous or heavily moist environments [17] [18]. In addition to its aesthetic and mechanical properties, zirconia is considered an inert biomaterial, which means that it has limited interactions with biological environments. In fact, in vitro and in vivo tests on zirconia have shown no mutagenic or carcinogenic compatibility [19] and a low affinity with bacterial plaque [20]. However, zirconium exhibits limited bone integration, in particular with adhesion to biological tissues, in particular bone [21]. Many types of zirconia surface treatments have been performed to improve biological activity and promote its integration into existing biological tissues: bonding with active phases such as hydroxyapatite [22], coatings [23], surface laser modifications [24] and texturing [25]. In this work, an innovative laser coating treatment with Si_3N_4 powders was

applied to the surface of the zirconia. Silicon nitride is a ceramic biomaterial that presents bioactive effects [26] [27] [28] that cannot be obtained with oxide based materials, as antibacterial properties and promotes cell proliferation[26]. However, Si_3N_4 has too high mechanical properties (hardness, toughness, resistance to cyclic load, etc.) that do not make it the most attractive for dental implant applications. In fact, Si_3N_4 has a high elastic modulus (young's modulus) which requires higher processing costs and in addition the stress load resulting from mastication could damage the bone or break the implant. The silicon nitride coating on zirconia was applied to preserve the mechanical properties of zirconium oxide but, at the same time, to stimulate osteointegration and antibacterial properties due to the properties of silicon nitride. The resistance to bacterial colonization, the ability to stimulate osteoblast differentiation and bone tissue production of Si_3N_4, has already been successfully applied for the application of prosthetic implants, as in the case of spinal fusion cages [29] [30] [31]. Several studies have shown [32] [26] [27] [28] [33] [34] [35] [36] [37] that the beneficial effects of silicon nitrides are due to the presence of nitrogen in the crystalline lattice, and in particular the formation and release of NH_4^+ nitrogen species. These species stimulate cell proliferation and damage common bacterial strains [38] [39] and silicon ions that actively contribute to the formation of mineralized bone tissue [32] [37] [35] [33]. The present work is intended to be a possible new improvement for dental prosthesis technology and also represents a further study in the understanding the mechanisms of cell proliferation and the antibacterial effect. The stoichiometric Si_3N_4 is used as a reference that will allow an unequivocal understanding of the role of each element. The thesis paper is divided into six chapters respectively:

1- Introduction

2- Materials: This chapter gives an introduction to the meaning of Biomaterials and Advanced ceramic materials. Then silicon nitride is introduced and respectively the production methods, general properties and the meaning of biocompatibility and antibacterial activity are described. Subsequently zirconia is introduced and the properties are described. Afterwards bone tissue is described with particular reference to Hydroxyapatite (HA), bases of osteointegration and factors that influence osteointegration and the concepts of bacterial inflammation on prosthesis are introduced. Finally, cellular and bacteria treatments for osteosarcoma cells (SAOS-2) and staphylococcus epidermidis bacteria are exposed.

3- Methods: This chapter describes in detail the instruments used. Initially an introduction of general Raman and IR spectroscopy is made, then Raman spectroscopy is introduced through a theory and instrumentation, subsequently FT-IT spectroscopy is exposed. Afterwards fluorescence microscopy is described through an introduction of fluorescence microscopy and

its instrumentation, moreover the marker and Stain used to analyse FM images are described in detail. Then the instruments SEM (scanning electron microscope), XPS (x-ray photoelectron spectroscopy) and laser Microscopy are introduced. Finally, all the experimental procedures are listed.

4- Result: This chapter describes the results of the experiments and can be divided into three sub-chapters. In the first sub-chapter the results of substrate characterization are presented, through the use of technical techniques: laser microscopy, FT-IR, Raman, XPS, SEM and Cross-sectional analysis. The second sub-chapter presents the results of the characterization of Staphylococcus epidermidis bacteria through the use of Raman, fluorescence microscopy and WST techniques. Finally, the third sub-chapter presents the results of characterization of SaOS-2 line cells through the use of fluorescence microscopy, WST, Raman, quality index and SEM techniques.

5- Discussion: This chapter discusses the results obtained.

6- Conclusion

Chapter 2

Materials

2.1 Biomaterials

According to the II International Consensus Conference on Biomaterials hold in Chester, Great Britain, in 1991 a biomaterial can be defined “as a material intended to interface with biological systems to evaluate, treat, augment or replace any tissue, organ or function of the body” [40].
First of all, in order to consider the biomaterial, there are two important properties that need to be taken into account, first of all to consider the biomaterial:

- *Biocompatibility*: it consists in the characteristic of establishing "not unfavourable" interactions with the organisms with which it comes into contact;
- *Biofunctionality*: it consists in the characteristic that a device must be able to reproduce a certain function, from a physical and mechanical point of view.

The subcategories of biocompatible material are numerous and are classified mainly in two distinct orders, called biostable and biodegradable, on the basis of the consequences on the material after grafting. The former includes materials that, once placed in situ, do not undergo substantial chemical and/or physical changes over time (dental prostheses). On the other hand, the latter includes materials that, once implanted, undergo substantial chemical and/or physical transformations that cause them to disappear over time.
This is not the only possible classification, another one considers instead the material-organism interaction, hence the definitions of biotoxic, bioactive, bioinert, bioreabsorbable.
In particular, the term *biotoxic* refers to materials that cause a rejection reaction by the biological tissue due to chemical and/or galvanic processes.
Bioinert materials are chemically and physically stable materials and have minimal interactions with surrounding tissues. These materials allow a good coexistence between organism and implant. In dental implants, the most common materials are: Ti, ZrO_2 and Si_3N_4.

Bioactive groups together all those materials that favour direct biochemical interactions with the biological tissue, which can grow on the surface of the material itself. All this allows the establishment of a solid mechanical bond between the natural tissue and the prosthetic implant. Typical examples of bioactive materials are some ceramic materials, such as hydroxyapatite and Si_3N_4 [41].

Lastly, *bioreabsorbable* materials undergo a progressive degradation within the biological system, without causing rejection reactions or toxic effects. The calcium phosphates belong to this class as the tricalcium phosphate, the porous hydroxyapatite and some bioglass. These are generally bioactive and are gradually replaced by biological tissue. Because of these characteristics, they are particularly useful when the replacement prosthesis has to occupy a limited space but they are also widely used for the controlled drug delivery.

Finally, a final distinction is made on the basis of the chemical nature: polymeric biomaterials, metal, ceramic and composite [42] .

2.2 Advanced ceramic materials

The common use of the term ceramic includes all non-metallic inorganic materials, consisting of metallic and non-metallic elements bound together by ionic or covalent bonds or, usually, by a hybrid of these. They are generally obtained by heating processed raw materials to obtain a rigid structure. These include advanced ceramic materials that are obtained from highly selected and pure raw materials and include: oxides, carbides, nitrides, silicide. Some of the most important advanced ceramic materials for structural uses are alumina (Al_2O_3), silicon nitride (Si_3N_4), silicon carbide (SiC) and zirconia (ZrO_2), combined with other refractory oxides [43]. Advanced ceramics are materials made in such a way as to offer unique characteristics through the control of composition and microstructure. The physical-mechanical properties of a polycrystalline ceramic therefore depend on the microstructure that is determined by the processing phases (synthesis), and the choice of raw materials. Essential is the way in which they are processed and fired, which are all factors that can influence the properties of the material [16]. Furthermore, the properties of ceramic materials are generally controlled by the atomic order, ordered if the structure is crystalline, disordered if amorphous, and on a larger scale, by the shape and arrangement of the grains and phases, and by the size and volume fraction of pores it contains [44].

2.3 Silicon Nitride

Silicon nitride (Si_3N_4) is a non-oxidic ceramic very rare in nature because it was found only in meteorite rock particles formed when the atmosphere was chemically reducing and rich in ammonia, the crust contained large quantities of silicon and other nitrides [45]. Synthesized by Deville and Wöhler in 1859 [45] and ignored until the 1950s, when it was used for various refractory applications. In the 1980s, the potential of Si_3N_4 ceramics was recognised due to its properties such as mechanical strength, thermal shock resistance, high temperature stability, hardness and wear resistance [46]. As a result, it is now one of the most studied ceramics. Today's major industrial applications include high performance bearings, turbine blades and glow plugs, i.e. applications requiring a material with extreme strength and toughness and high fracture resistance, strength and low wear [47] [48]. Si_3N_4 is also used in the automotive, turbomachinery and power industries, where it has a significant advantage due to its low density (half that of bearing steel), low friction, corrosion resistance and reliable performance under extreme conditions [49]. In aircraft and spacecraft high performance, where the operating conditions of very demanding bearings such as high vacuum ($<10^{-6}$ torr), extreme temperatures (e.g., 230 to 150 °C). Si_3N_4 finds its space also used in the manufacture of bearings subjected to extreme performance: large temperature differences, long service life (about 10-15 years without maintenance and subjected to stress and fatigue) and low friction [50].

The material properties of Si_3N_4 have been developed in medical fields as well, as it has proven to be biocompatible [51] [52]. It is used in spinal casting implants and is being developed for the coupling of components of hip and knee joint prostheses. In addition, Si_3N_4 has been tested in surgical screws and plates as a starting material [29] [30] [31]. The constraints of the widespread use of technology concern the production of most technical ceramics: i.e. the cost of materials and processing, the need for reproducibility, reliability and precision in production.

2.3.1 Property

There are three different crystallographic structures of silicon nitride (Si_3N_4), α, β and γ [53]. The α and β structures are the most common forms of Si_3N_4 and can be produced under ordinary pressure conditions. The γ phase can only be synthesized under high pressures (17 GPa) and

temperatures (2100 K) [54]. The forms α and β-Si_3N_4 have hexagonal structures, which consist of Si_3N_4 tetrahedra at a shared angle [55].

Respectively α-Si_3N_4 presents the lattice parameters of a=0.775 nm; c=0.52 nm and an ABAB.. sequence, while β-Si_3N_4 presents the lattice parameters of a=0.76 nm; c=0.29nm (about half of α) and an ABCDABCD.. sequence. The AB planes are the same for α and β, while the CD planes for β are conceptually similar to the AB sequence except for a 180° rotation along the c-crystallographic axis (Fig. 2.0).

The form α is converted into β at a high temperature above 1400°C, while the reverse process is energetically unfavourable (irreversible transformation) [3]. Therefore, the transformation from α to β is permanent.

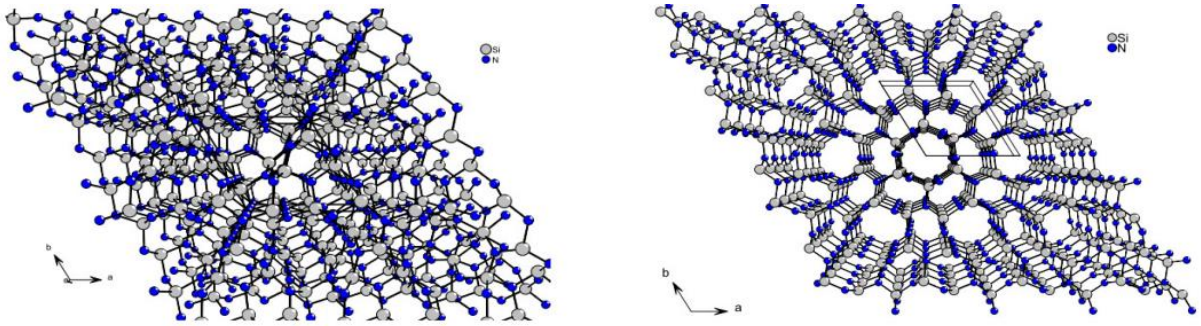

a b

Figure 2.0: Crystal structure stacking model of a) α- Si_3N_4, b) β- Si_3N_4

Silicon nitride has a predominantly covalent Si-N chemical bond (the silicon atom is surrounded by four nitrogen atoms). This type of bond is very strong and extremely directional and determines the characteristics of hardness and resistance to wear and the low coefficient of thermal expansion.

The tribological properties of Si_3N_4 are divided into mechanical (friction and abrasion) and chemical properties. Like most metal and other non-oxide materials, Si_3N_4 is protected by a thin layer of oxide (SiO_2) about 2-5nm thick [56]. When this coating is removed by erosion or wear, the surface quickly repairs itself through re-oxidation, thus limiting degradation. The surface passivation layer occurs due to its thermodynamic instability in oxidizing or humid environments. In addition, the surface in contact with Si_3N_4 is subject to oxidative degradation especially in the presence of moisture. This phenomenon is also present at low temperatures either in liquid water or in humid conditions [57] [58] [59] [60] [61] [62] [63]. it is hypothesized that it can also be operative for in vivo joints [64] [65] [66]. Chemical wear occurs through the following Si_3N_4 surface reactions [67]:

$$Si_3N_{4\,(s)} + 6O_{2\,(g)} \rightarrow 3SiO_{2\,(s)} + 2N_{2\,(g)} \qquad \Delta G_{(298\ K)} = -1922\ [KJ/mol] \qquad (2.0)$$

$$Si_3N_{4\,(s)} + 6H_2O_{\,(l)} \rightarrow 3SiO_{2\,(s)} + 4NH_{3\,(g)} \qquad \Delta G_{(298\ K)} = -565\ [KJ/mol] \qquad (2.1)$$

However, Si_3N_4 has a more complex surface chemistry, since Si-N, Si-N-O and Si-O bonds [56] [68] [69] [70] [71] [72]are present in the near-surface region. By moving towards the surface, the passivated layer is also present and oxygen enters the lattice. Both Si-N-O and Si-O bonds are usually present in the outermost surface layers. In addition, when the Si-O layer increases due to oxidation, the layer becomes chemically equivalent to silica (SiO_2). This process can happen when Si_3N_4 is exposed to moisture or air the Si-N bonds react to form neutral (Si-NH_2, Si-OH) or ionic (Si-NH_3^+, Si-OH_2^+, Si-O^-) functional groups [69] [73] [74] [75] [76] The chemical reactions describing these surface motions are [69] [74]:

$$Si_3N_{4\,(s)} + 2H_2O_{\,(l)} \rightarrow Si\text{-}NH_{2\,(s)} + Si\text{-}OH_{(s)} \qquad (2.2)$$

$$Si\text{-}NH_{2\,(s)} + H2O_{(l)} \rightarrow Si\text{-}OH_{(s)} + NH_{3\,(g)} \qquad (2.3)$$

The strong smell of ammonia gas detected while working in a wet environment with Si_3N_4 is a confirmation of these reactions. The dissociation of function groups (Si-NH_2 and Si-OH) in water occurs through acid-base reactions [69] [77] [78]:

$$Si\text{-}OH_2^{+}{}_{(s)} \leftrightarrow Si\text{-}OH_{(s)} + H^+_{(aq)} \qquad (2.4)$$

$$Si\text{-}NH_3^{+}{}_{(aq)} \leftrightarrow Si\text{-}NH_{2(s)} + H^+_{(aq)} \qquad (2.5)$$

$$Si\text{-}OH_{(s)} \leftrightarrow Si\text{-}O^-_{(s)} + H^+_{(aq)} \qquad (2.6)$$

The main reactions at homeostatic pH are (2.5) and (2.6), while protonation of one of a silanol group (2.4) is unlikely to occur. These reactions are dependent on the pH variable and the balance can be shifted to both right and left. The pH at the point where the net charge of the considered species is equal to zero is called the isoelectric point (IEP) [79]. The IEP of pure Si_3N_4 is pH ~ 9.3 - 9.7 due to the presence of high surface concentration of amine (Si-NH_2) [70] [80], while pure SiO_2 has an isoelectric point of 2-3. Ammine has a reduction potential that requires high pH and Si_3N_4 rarely has a negative charge. On the other hand, SiO_2 has a highly favourable reduction potential (6) [81]. IEP, it has been demonstrated, as the surface thickening SiO2 oxide layer, defined as "passivation layer". In Si_3N_4 the pH change leads to a different composition of the passivation layer, in particular: ~ 9 pH only pure Si_3N_4 to ~2 pH only pure SiO_2 [70] [76]. There is therefore a correlation, through IEP measurement it is possible to measure the passivation layer.

In tribo-chemical wear, the passivated film acts as a solid lubricant for the joint components. The Si-OH and Si-O oxide film is quite effective in protecting the joint surfaces, which results in low material wear. In particular, the joint surfaces are very smooth and are generated by the colloidal film which causes low friction between the components [82].

Si_3N_4 may be produced from interlaced fibrous grains with a completely dense microstructure, called "*in situ* toughening", which causes a change in the reticular microstructure. The modification of the in situ hardening microstructure occurs through the formation of an elongated or whiskers-like structure of the grains, is of great interest. The precise composition of the additives used and the heat treatment during the manufacture of the Si_3N_4 material also promotes the growth of elongated grains (Fig. 2.1). This generates a self-reinforcing effect due to greater cohesion in the structure. These structural changes promote the formation of elongated grains in Si_3N_4 situ toughening, which provide hardening mechanisms that are limited or absent [83]. Therefore, elongated grains cause greater fracture toughness due to mechanisms such as crack deflection, micro-fracture, and grain extraction and binding actions [84]. Fig. 2.1 shows how the propagation of a crack through the in-situ toughened material becomes more tortuous. In addition, the propagation of a crack in Si_3N_4 in situ toughening (rod elongated grains) deflects the crack (crack deflection) along the edges of the elongated grains and has been shown to provide energy dissipation mechanisms that reduce the tendency of the crack to grow rapidly. Mechanical strength and toughness are significantly increased.

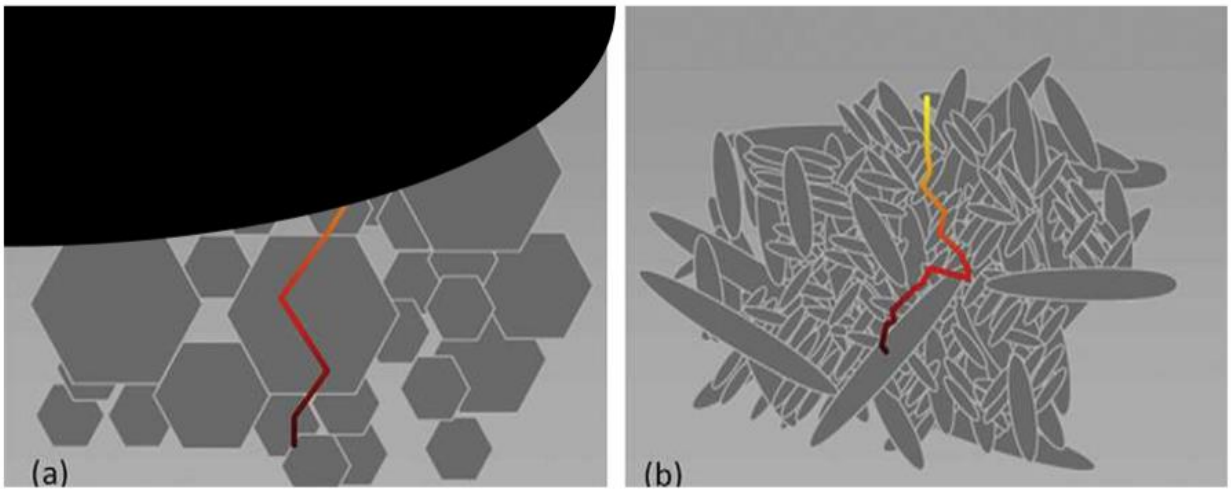

Figure 2.1: Illustrations show the differences in crack propagation modes for (a) conventional ceramics and (b) in situ toughened silicon nitride ceramics.

This material has an optimal combination of flexural strength, wear resistance and fracture toughness for surgical applications such as: total joint arthroplasty (joint reconstruction) [85]

[86] [87] [88], or in arthrodesis devices and bone scaffolds using highly porous constructs [89] [90] [91] [92].

2.3.2 Production Methods

Si_3N_4 can be synthesized in several methods using Si_3N_4 powders as the starting reagent. In order to be suitable, it must be submicrometric with variable granulometry. So that it can guarantee an excellent packaging. A final product can be made by "coarse" particles with a size of 10-15 µm; "medium" particles of 1-2 µm; "fine" particles of 0,1-0,5 µm [93] [94]. In order to obtain Si_3N_4 powders the main synthesis techniques are:

Direct Si nitridation process: Silicon dust (Si) is heated in N_2 (nitrogen atmosphere) to a temperature in the range 1200-1400 °C, where the Si reacts with N_2 to form Si_3N_4 and binds the particles together [95]:

$$3\,Si_{(g)} + 2\,N_{2\,(g)} \rightarrow Si_3N_4 \qquad (2.7)$$

During the reaction, the weight of the silicon sample increases progressively due to the chemical combination of silicon and nitrogen. The reaction is facilitated by the use of transition metals as catalysts [96] [97] [98] and coarse particles and agglomerates are generally produced which require grinding to obtain a suitable powder. The resulting powders are α-Si_3N_4, which are converted to β-Si_3N_4 only during densification [94] [96] [97] [98].

Carbothermal reduction/nitridation of silica: Silica and carbon are reacted in the presence of nitrogen; first silica reduction and then nitriding. The reaction is conducted at a temperature in the range 1250-1300 °C. was the first method used for the production of Si_3N_4 [99].

$$SiO_{2\,(g)} + 2\,N_{2\,(g)} + 6\,C \rightarrow Si_3N_4 + 6\,CO_{(g)} \qquad (2.8)$$

This method is now considered the most economical industrial method for the production of high purity α-Si_3N_4 powders.

Vapor-phase at high temperatures: $SiCl_4$ (silicon tetrachloride) and ammonia are made to react and reaction can be conducted in gaseous phase or in solution.

$$3SiCl_{4(g)} + 4NH_{3(l)} \rightarrow Si_3N_4 + 12HCl_{(g)} \qquad (2.9)$$

The calcination temperature is fundamental; at about 1420 °C α-Si_3N_4 equiaxial grain is produced, while, calcination at temperatures above 1460 °C produces β Si_3N_4 whiskers.

The general process of powder densification is the sintering process, which consists in submitting the form to the green state to a temperature and pressure program.

The process is described by Frenkel's ball model according to which two adjacent particles are joined through diffusion mechanisms. The reaction mechanism is related to the Gibbs free energy reduction $\Delta GT = \Delta Gv + \Delta Gb + \Delta Gs$; in which $\Delta Gs = \gamma \Delta A$ is the term referred to the surface reduction and is the predominant term. The terms ΔGv and ΔGb refer to volume variation and grain edge variation respectively. Additives (metal oxides) are added to the Si_3N_4 powder. The process involves an interaction between the additives with the passivated layer (SiO_2) on the surface of Si_3N_4. The additives react by forming a liquid phase that surrounds the Si_3N_4 particles, thus promoting the densification process. Upon cooling, the liquid phase solidifies to form an amorphous (glassy) or partially crystallized glassy phase at the grain boundaries of Si_3N_4.

At the sintering temperature there is the dissolution of phase α and the precipitation of phase β. At the end of the process there is a β structure with elongated grains in a glassy matrix that will form the grain edges. The most common metal oxide additives are magnesia (MgO), alumina (Al_2O_3) and yttrium (Y_2O_3) [7] [8] [47], because they have thermal properties very similar to Si_3N_4 which avoid problems such as internal stress and different thermal expansions. In fact, through the use of additives the main modified properties of silicon nitride are the thermal properties. This is because, during the cooling process, the liquid phase (passive phase) that was formed during sintering solidifies as crystalline silicon yttrium, yttrium and oxygenated aluminium, which is called: SiYAlON. In addition, the presence of additives modifies the surface chemistry of Si_3N_4, because the hydrolysed functional groups Al-OH and Y-OH are formed in passive regions.

During the sintering process, the powder and additives are subjected to pressure, thus avoiding porosity problems. In fact, an ambient pressure sintering process has a porosity of 15-25 % which results in low mechanical properties. The common pressure sintering methods used in Si_3N_4 are hot pressing (HP) and hot isostatic pressing (HIP). HP subjects the ceramic material to pressures up to 40 MPa and temperatures of 1600°C. About 5% of additives are added. The result is a piece with a porosity of 2 %. However, this process is only suitable for obtaining simple shapes and therefore the subsequent machining is carried out on the workpiece. HIP the material is subjected to pressures of 150-200 MPa and temperatures of about 2000°C. The result is a workpiece with a perfect homogeneity and density with an addition of only 1 % of additives.

2.3.3 Biocompatibility

Ceramics such as ZrO_2 and Al_2O_3 are the main combined materials in orthopaedic applications thanks to their excellent biocompatibility, low friction and better wear quality, which has allowed a technological development compared to the Co-Cr alloy [100] [101]. Nowadays, however, the interaction of living tissue at the molecular level with bioceramics (ZrO_2 and Al_2O_3) is well known and established [102]. The new frontiers of technological development for new biomaterials with more advanced properties has introduced the study of silicon nitride. Several studies have tested the biocompatibility of Si_3N_4 through different cell lines (MG-63, SAOS-2, L929) [103] [104] [105] and in vivo/vitro experiments [106]. In addition, Si_3N_4 has been shown to be bioceramic and it can promote cell adhesion, normal proliferation and differentiation [107]. This makes silicon nitride biocompatible [108] [109] [110] [111] [112] [113] [114] and attractive for various orthopaedic applications [115] [116] [117] [118] [102].

The biocompatibility of an orthopaedic implant depends on its surface characteristics, such as chemistry, topography (roughness or smoothness) and biophysical properties (e.g. surface energy, surface load, degree of hydration). These characteristics can have a strong effect on the response of cells, tissues and bacteria. An efficient orthopaedic implant must be able to adapt to bone defects or an unusual anatomy of the patient with a dense, porous architecture or composed of a graduated porosity to suit specific applications [103]. In addition, surface characteristics can strongly influence the performance of an in vivo implant [119].

Si_3N_4 bioceramics can be sintered with smooth or micro-rough surface topography with an oxidized surface layer of silicon oxide equivalent composition (Si-O-N). In addition, heat or chemical treatment can be used to vary the chemical composition of the surface to SiO2 that changes the hydrophilic [120] [121] [122]. This different surface topography allows Si_3N_4 to make orthopaedic implants with a microrough surface that provides greater osteointegration and smooth surface for a greater antibacterial effect.

It has been shown that in osteointegration, silicon is incorporated into hydroxyapatite (HA) by assisting, in the synthesis of glycosaminoglycans and proteoglycans, by ion replacement [32]. In fact, hydroxyapatites replaced by silicon, porous silicon and silicon/silica nanoparticles have been developed to accelerate the osteointegration process. These materials share the common mechanism of bioactivity enhanced by Si_3N_4 [26] [27] [28]. In protein synthesis, nitrogen is essential for bone growth and tissue repair [33]. Cell metabolism consists of transforming H_2O, CO_2 and three inorganic compounds of nitrogen nitrate (NO_3^-), ammonium (NH_4^+) and di-

nitrogen (N_2) into more complex bio-molecules [34]. Silicon nitride (used as a biomaterial) has been shown to have H_4SiO_4, NH_4^+, NO_3^-, and N_2 abundantly and readily available during biological interactions [35]. The modulable chemistry of silicon nitride [36] provides it with metabolic interactions between eukaryotic and prokaryotic cells (bacteria) and prokaryotic cells on its inorganic surface [37] [35].

2.3.4 Antibacterial activity

Silicon nitride ceramic material (Si_3N_4) has been used in spinal cord implants showing antibacterial effects against both Gram-positive and Gram-negative bacteria [123]; however, physical-chemical interactions between Si_3N_4 and bacteria are not yet fully investigated. In order to comprehend the antibacterial effect, it is first necessary to understand the mechanisms of bacterial adhesion to the Si_3N_4substrate. These mechanisms are complex and depend on many factors, such as the morphological and chemical characteristics of the surfaces. Surface topography has a fundamental role in the bacteria/substrate interaction that influences both adhesion and biofilm formation. In general, rough surfaces promote adhesion and colonisation. The surface chemistry of Si_3N_4 has demonstrated the existence of a limited diffusion thermodynamic driving force, which converts silicon nitride to silicic acid $Si(OH)_4$ and ammonia (NH_3). NH_3 on the surface increases the local pH; i.e. from ~ 5.5 to ~ 8.5 [38] and highly alkaline environments can delay or prevent bacterial adhesion and biofilm formation. An increase in pH, reduces the ability of the bacteria to adhere to the substrate, which leads to a deterioration in the maturation of the biofilm. In particular, the pH influences the most abundant polyanions in cytoplasmic membranes lipids (lipoteichoic acid and teichoic acid) that are linked to peptidoglycan (PG) [39] [38].

In addition, the change in pH involves chemical interactions between the substrate and the metabolic components that lead to the autolysis (cellular self-destruction) of PG. In particular, activation of autolysin, leading to peptidoglycan hydrolases, which strongly alters peptidoglycan turn over, is promoted. PG degrades and causes a decompensation to the osmotic cell balance from a respiring to a depolarized status [38] [39]. An example of cell lysis for beating Staphylococcus epidermidis is shown in Fig. 2.2 [39].

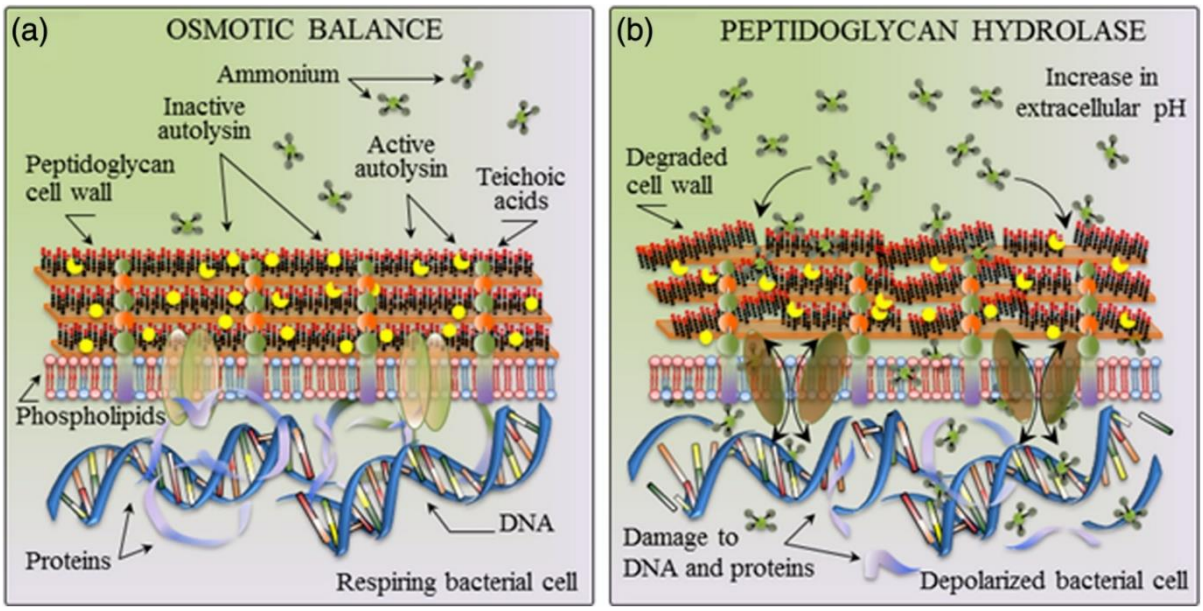

Figure 2.2: (a) Schematic model of S. epidermidis bacterial membrane in osmotic equilibrium and (b) in depolarized status after being affected by peptidoglycan hydrolase [39].

2.4 Zirconia

Zirconia (ZrO_2), one of the most studied ceramic materials, is used in various sectors, especially for its thermal and mechanical properties. In the metallurgical field it is used for the manufacture of refractory materials, opacifiers for ceramics and foundry sand [124].

With its interesting physical properties, i.e. hardness, resistance to wear and refractory (resisting high temperatures for long periods without reacting chemically with other materials) zirconia has been developed for applications such as extrusion dies, machine wear parts and piston liners.

Another important property related to the control of the composition and modification of the microstructure is the "phase transformation toughness". Toughness is the ability of a material to absorb energy and deform plastically before breaking; defined as energy density (J/m3) [125]. The main limitation to applications in ceramic materials is their low toughness. The possibility of increasing the toughness of zirconia by phase transformation, i.e. the resistance they are able to oppose to crack propagation, has led to numerous technological developments. In the 1990s, zirconium began to find its place in prosthetic dentistry, particularly in implantology [126] [127] due to its properties as a ceramic material, specifically for its colour and translucency [128] biocompatibility and elastic modulus (Young's modulus).

Studies were developed to investigate the bone-implant interaction, which proved to be better than alumina-covered implants, even after some long time using [129]. Currently, research in Implantology is introducing new materials that can facilitate osseointegration, hindering instead bacterial colonization and thus preventing peri-implantitis.

2.4.1 Property

The unique property of zirconia is its ability to create polymorphic structures (Fig. 2.3).. At atmospheric pressure, these are of three types: the monocline phase (m-ZR), the tetragonal phase (t-ZR) and the cubic phase (c-ZR);

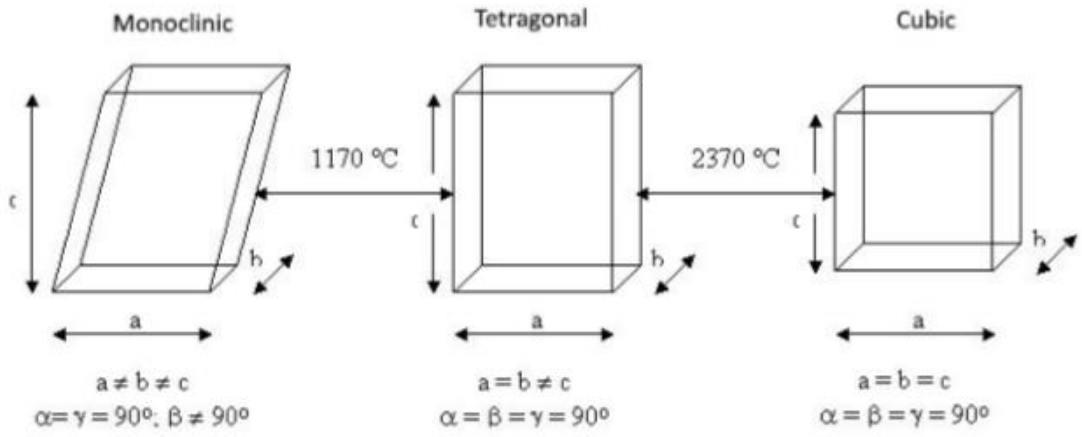

Figure 1.3: Allotropic forms of zirconia

The stable crystalline structure for pure zirconia at room temperature and atmospheric pressure is monocline (m). The monocline phase is transformed into tetragonal (t) at about 1170°C, and the transformation is accompanied by a volume contraction of about 5% during heating and an equivalent expansion during cooling [16]. As the temperature increases, at about 2370°C zirconia transforms from tetragonal to cubic (c), with a volume variation of about 2.3% [131], and melts at 2716°C [132] [133]. These lattice transformations are athermic (they do not transmit heat), adiffusional (without atomic diffusion), and involve a lattice deformation [134]. The volume variations associated with these transformations are sufficient to cause the formation of cracks that compromise the stability of ceramics, so pure zirconia components are unsuitable for structural applications. However, the control of the transformations, and in particular that from t-ZR to m-ZR, is the basis of the tenacity mechanism of zirconium-based

ceramics and can lead to significant increases in mechanical properties. The grains of t-ZR, when embedded within a densely sintered structure, cannot expand freely and become m-ZR. As a result, the grains remain at room temperature in the metastable tetragonal phase. The transformation from tetragonal to monocline can then be induced by the application of external stresses ("stress induced transformation") that tend to dilate the structure of the crystalline lattice. Immediately [135] [136] [17] [18] after a crack begins to form, the grains of t-ZR close to the crack are able to expand and transform, returning to the m-ZR phase. The expansion adjacent to the crack compresses the crack and arrests the process (Fig. 2.4 [135]). The final result is that, in the propagation of a crack inside the material, part of the energy is dissipated to induce the phase transformation from tetragonal to monocline. In this way, the fracture toughness of the material is definitely improved. The "energy absorption" during the tetragonal-monocline transformation at room temperature in partially stabilized zirconia was recognized as a tenacity mechanism in 1975 [136].

Toughened zirconia has been developed in three different forms: FSZ fully stabilized zirconia; PSZ Partially Stabilized Zirconia; TZP Tetragonal Zirconia Polycrystals [137].

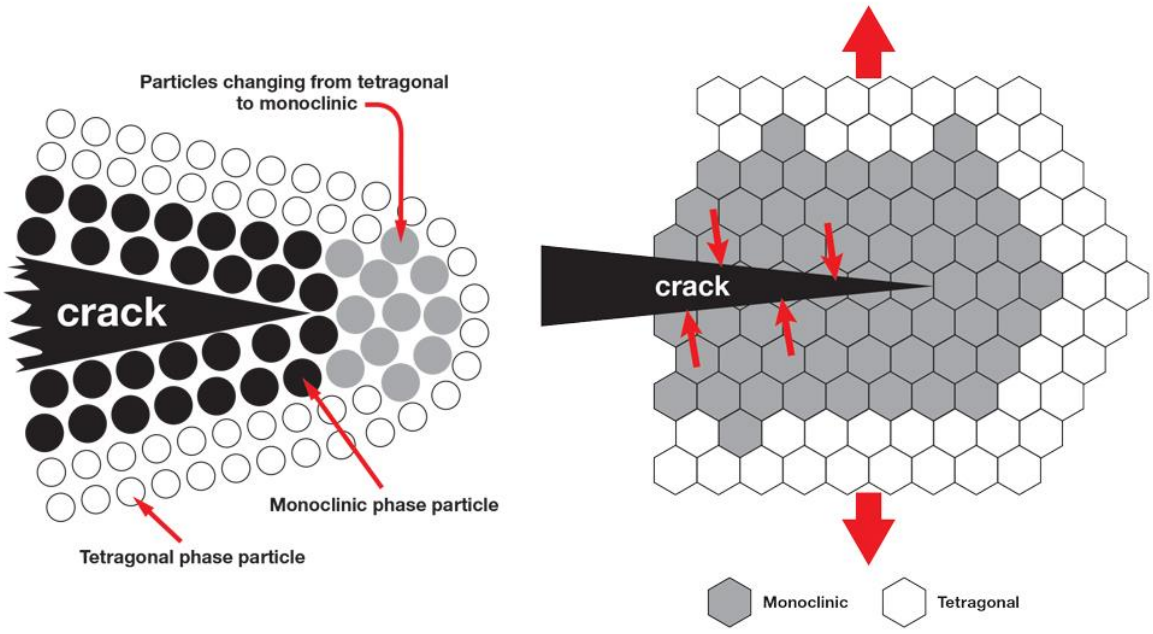

Figure 2.4: Schematic representation of the area subjected to stress due to the propagation of a crack. Zirconia changes from the tetragonal phase to the monocline phase.

The three materials have in common the presence of stabilized tetragonal zirconia and the fact that the increase in toughness is related to the tetragonal-monocline transformation.

What distinguishes them is the mechanism of stabilization of the tetragonal phase. In PSZ and TPZ t-ZR is stabilised by the addition of oxides, usually magnesium oxide (MgO), yttrium

oxide (Y_2O_3), calcium oxide (CaO) and cerium oxide (Ce_2O_3). The addition of oxides, disadvantages the formation of tensioned monocline phase at room temperature, and makes stable (metastable) the crystalline cubic and tetragonal structures, more symmetrical [138]. These metastable phases have a structure similar to that of pure zirconia, but have doping ions substituted at the Zr^{4+} atomic sites and have a fraction of oxygen sites vacant to maintain charge neutrality [139]. Since the mobility of cations in zirconia is rather low and oxygen vacations are locally ordered, the cubic and tetragonal metastable phases have prolonged stability at room temperature [140].

In FSZ the zirconia is the cubic phase with the addition of 8% of Y_2O_3, normally used for oxygen sensors, and fuel cell electrolytes. In PSZ Partially Stabilized Zirconia 2-5 mol% of Y_2O_3 is added, depending on the grain size [140]. PSZ zirconia is therefore characterized by the addition of lower concentrations of dopants than FSZ, hence the designation "partially stabilized". PSZ zirconia is heated to form zirconia in the cubic phase only, then cooled in a controlled way to develop a dispersion of tetragonal zirconia precipitates within the cubic matrix. Normally, the t-ZR should turn into the monocline shape during cooling, but to do so it should expand. The high strength of the surrounding cubic zirconia prevents this expansion, so that the tetragonal shape is maintained up to room temperature. The tetragonal structure is subject to transformation into the monoclinic phase when a stress force is applied, for example by an advancing crack. TZP zirconia essentially has tetragonal zirconia as the only metastable phase in the self-tenacity prerogative for the transformation of the tetragonal-monocline phase after the application of a load.

Factors that may cause structural conversion from tetragonal to monocline may be abrasive processes that can induce compressive stresses to a depth of several microns below the surface. Or, the t-m transformation may be caused by the roughness process that increases the volume of monoclinic grains as a result of the expulsion of some debris from the surface of the material. Moreover, a structural conversion from tetragonal to monocline is a spontaneous process known as aging and occurs in the temperature range between 200◦ and 300◦C in the presence of water vapour [17] [18]. The three types of zirconia FSZ, PSZ, TZP have high mechanical resistance and high toughness. A ceramic material with an internal mechanism capable of inhibiting crack propagation was made available, limiting immediate brittle rupture.

2.5 Samples

In this work, zirconia and silicon nitride were used as substrates. The zirconia samples were: polished zirconia (ZR) and rough zirconia (rough ZR). The rough zirconia samples were prepared using a diamond tip to create oriented scratches on the surface of the material.
Silicon nitride was used as a bulk ceramic. Silicon nitride was used as a bulk ceramic silicon nitride (SN) and as a cladding on the surface of a zirconia substrate (Coating SN). The coating was done through a laser. The work of this thesis does not analyses the coating method.

Silicon nitride (*SN*) | Coated Zirconia (*Coating SN*) | Zirconia smooth (*ZR*) | Zirconia rough (*ZR rough*)

Figure 2.5: Surface images of the samples used for this work.

2.5.1 Silicon Nitride

The silicon nitride samples were in the form of discs (diameter 12 mm, thickness 1 mm) and were supplied by Sintx Corp. (Salt Lake City, Utah, USA). The material consisted of a two-phase microstructure comprising β- Si_3N_4 acicular grains separated by a continuous sub-micrometric film of Si-Y-Al-O-N. In order to obtain the ceramic powder, the bulk samples were mechanically ground to a powder with an average particle size of 15 μm. The conditions applied to get a Si_3N_4-cladding on zirconia were the following: laser wavelength 1064 nm, maximum pulse energy: 70 joules, peak power 17 kW, voltage range 400 V, pulse time 4 ms, and spot size 2 mm. The device operated under a constant flow of nitrogen gas to limit the decomposition and oxidation of Si_3N_4. It was necessary to repeat the operation three times in order to obtain a homogeneous coating with thickness, t = 15 ± 5 μm, over the entire surface of the substrate. A motorized x-y stage with a lateral accuracy of 10 μm was used to align the sample with the laser source.

2.5.2 Zirconia

The material consisted in stabilized zirconium oxide samples containing 3% yttrium and were obtained from a commercial producer (Kyocera, Kyoto, Japan). To produce a "roughening effect" on otherwise smooth zirconia substrates, abrasions were carried out over the entire surface using a diamond cutting disc (tip diameter: 25 μm) under an applied load of 20 ± 5 N. Once the surface was covered with unidirectional scratches, the direction of scratching was rotated about 90° and the operation was repeated again.

2.6 Bone tissue properties and characteristics

Bone tissue is a connective tissue that is physically identified by the combination of inorganic and organic substance, combined to form a fundamental amorphous substance. The components of the organic part are collagen I, ossein and a glycoprotein called osteo-mucoid; derived from extracellular matrix. In the inorganic substance, which in adults accounts for about 60-70% of the total bone mass, are calcium phosphate (86%) in the form of hydroxyapatite crystals $Ca_{10}(PO_4)_6(OH)_2$, calcium carbonate $Ca_3(PO4)_2$ (12%), magnesium phosphate (1.5%), calcium fluoride (0.5%) and iron oxide (traces). Elasticity and tensile strength are provided by the organic component, while stiffness and hardness are provided by the mineral component (due to the important presence of hydroxyapatite): these characteristics make the fabric ideal for structural and support functions. From the point of view of mechanical properties, an increase in the mineral content makes the bone brittle and brittle, a decrease makes it softer and more deformable [141].

Collagen represents 65-80% of the dry mass of specialized connective tissues (similar to tendons, skin, joint capsules and cartilage), but it is the only protein with significant tensile strength-resistance properties. This characteristic derives from the molecular configuration of the collagen macromolecule, one of the largest molecules of our organism with a filamentous structure and entirely made up of molecules of tropocollagen. Biological and environmental factors influence its typically three-dimensional configuration. Using transmission electron microscopy (SEM), it can be seen the fibrils are assembled with each other with a phase shift of a quarter of their length. Each individual unit of tropocollagen consists of three peptide chains, the intracellular synthesis of which occurs independently. Each chain contains

approximately 1000 amino acids. Most of the chains (called alpha chains) are ordered precisely and with frequent repetition of the glycine-proline-hydroxyproline, glycine-proline-x or glycine-x-proline sequences where x is another amino acid. Collagen by nature has a high percentage of glycine, proline and hydroxyproline. Among these three is glycine which, being smaller in size, allows its compact arrangement necessary to assemble the three alpha chains in the tropocollagen. Among the organic components there are other protein components Osteocalcin (OC), Osteonectin, Osteopontin (OPN) that have the function of modulating the mineralization and adhesion between the cells and the bone matrix. [142]. The bone tissue cells that provide for the growth, production and resorption of bone tissue are: *Osteo-progenitor*, *Osteoblasts*, *Osteocytes* and *Osteoclasts* (Fig. 2.6) [143].

Osteo-progenitor cells are of mesenchymal origin with stem properties: they can proliferate and differentiate into osteoblasts. Normally they are used to be found in the periosteum and endosteum: when reactivated, they provide the formation of new bone tissue.

O*steoblasts* are mature cells that release extracellular matrix to form new bone tissue. Osteoblasts are massive cells, rich in alkaline phosphatase and highly polarized towards the deposition front, where the collagen and protein fibres of the bone matrix (including OP, OPN) secrete. The new organic matrix deposited and not yet mineralized is called osteoid. Its average thickness is of the order of 10mm with a growth rate of 0.5mm / day. The initial stages of deposition are rather fast. Subsequently, the deposition slows down and the osteoblasts progressively modify the form only from high and voluminous cells to horizontal cells with less and less cytoplasm. As the deposition progresses, other osteogenic cells reach maturation and begin to release extracellular matrix, embedding the osteoblasts on the osteoid in the matrix that the new cells deposit.

O*steocytes* are the osteoblasts included in the extracellular matrix. As a result, the new osteocytes are subjected to the mineralization process. Osteocytes maintain contact with osteoblasts by cytoplasmic prolongations, which have numerous gap junctions, creating a cytoplasmic network. They have an oval-shaped body, with a major axis parallel to the bone surface. Numerous cytoplasmic connections emerge from the body and are immersed in the mineralized matrix. The neo formed osteocytes continue to release extracellular matrix within their own bone gap. The cell volume decreases by one third and the cell becomes dormant.

Osteoclasts are the cells that specialize in removing the bone matrix. They are not cells that live in bone tissue, but are formed when the bone matrix has to be removed and disappear at the end of the process. The principle of function is in contact with the bone matrix and via an acidic pH (5.2) they erode the surface. Through an acid catalysis promoted by the enzyme acid hydrolase,

and through the hormone calcitonin, produced by the thyroid, the activity of the osteoclasts is inhibited [144].

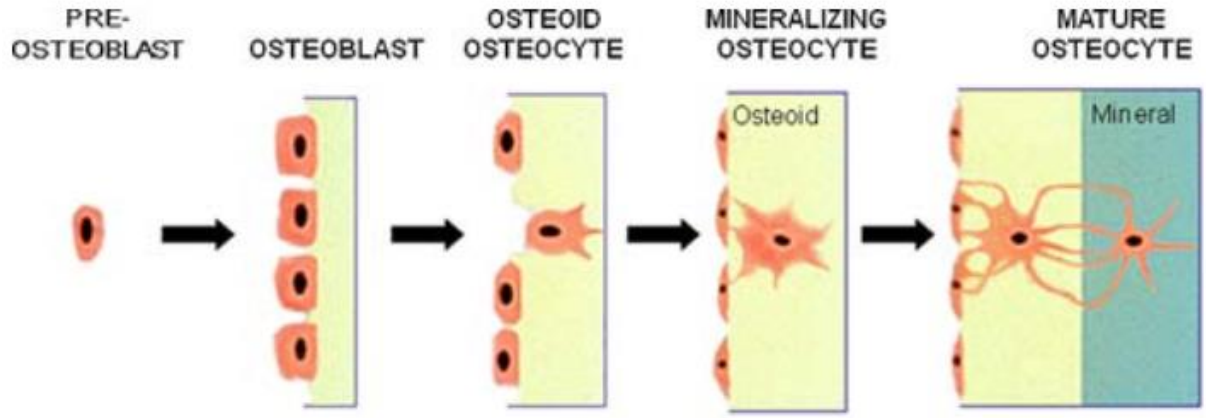

Figure 2.6: Example of bone growth through cells: osteo-progenitor, osteoblasts, osteocytes.

2.6.1 Hydroxyapatite (HA)

Since the Hydroxyapatite (HA) is the main component of the tooth, it is essential to deeply know its entire structure. HA is a natural mineral whose chemical formula $Ca_{10}(PO_4)_6(OH)_2$ has a crystalline structure with hexagonal symmetry and spatial group $P6_3/m$ with lattice parameters a = b = 9.432 Å, c = 6.881 Å [145] [146]. As shown in Figure 2.7.

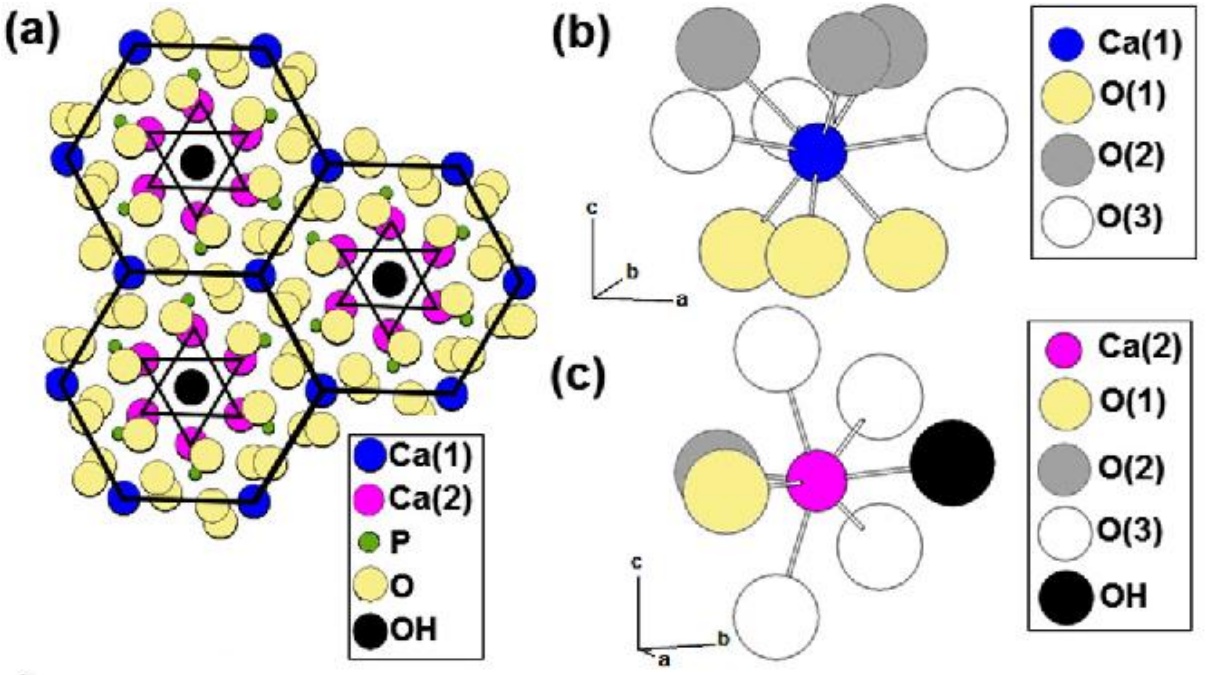

Figure 2.7: The crystal structure of hydroxyapatite.

The structure contains tetrahedra of PO_4 held together by Ca and OH^- ions; calcium ions are present four as Ca(I) and six as Ca(II). HA, $Ca_{10}(PO_4)_6(OH)_2$, for bones and teeth is used as a model, however, apatites are rarely found in pure stoichiometric form because they can incorporate a wide variety of impurities. Depending on the impurities it is classified into three types: the first has $Ca_{10}(PO_4)_6X_2$, X = F^-, CO_3^{2-}, octacalcium phosphate $Ca_8H_2(PO_4)_6{\cdot}5H_2O$ (OCP), tetracalcium phosphate $Ca_4(PO_4)_2O$ (TTCP). The second type includes polymorphic forms of tricalcium phosphate (TCP), $Ca_3(PO_4)_2$. Finally, the third type is Ca-PO_4 sheet-containing compounds which includes dehydrated dicalcium phosphate $CaHPO_4.2H_2O$ (DCPD), anhydrous dicalcium phosphate $CaHPO_4$ (DCPA) and monocalcium phosphates, $Ca(H_2PO_4)_2{\cdot}H_2O$ and $Ca(H_2PO_4)_2$ [147].

HA is thermally unstable, depending on its stoichiometry at temperatures from about 800-1200°C it begins to decompose. Stoichiometry is very significant if the work of osteoblastic cells is studied or thermal processing of the material takes place. The stoichiometric molar ratio of calcium and phosphorus in HA is 1.67. This ratio, Ca/P, if it is higher than the stoichiometric value you are in an acidic environment and the higher the solubility of HA will be [148].

HA is the inorganic phase of teeth and bone [149] [150], and for biomedical applications it is an essential and attractive material [151] [152] [153] [154]. In HA, replacements to phosphate groups, calcium ions or the hydroxyl group can occur. These replacements help living tissue to maintain a normal metabolism. The main substitution takes place with CO_3^{2-} which is a variation between 3 and 8%. Replacements occur mainly with ions such as Mg^{2+}, Na^+, K^+, Cl^-, F^- and many other ions [155] [156] [157]. The replacement rate varies depending on the age of the HA [158]. Recent studies have shown that the concentration of CO_3^{2-} increases with age, while the concentration of HPO_4^{2-} decreases. These substitutions also change properties such as lattice parameters, mechanical properties, morphology, magnetic properties and stability [159] [160] [161] [162] [163] [164] [165] [166] [167] [168]. For instance, substitution with F^- to OH^- ions decreases the solubility in acids [169]. While carbonate ions interact with the ionic interactions that establish the structure of apatite. Carbonate ions exchange with hydroxyl (type A carbonate), or PO_4^{3-} tetrahedra (type B carbonate) [170] [171].

2.6.2 Bases of osteointegration

The field of rehabilitation of edentulous patients was enriched by the innovation introduced in the mid-twentieth century by a Swedish professor, Per-Ingvar Brånemark, who had the merit of having developed an implant method based on well-defined criteria and reliable predictions. He is responsible for the concept of osteointegration, defined as "the direct structural and functional union between bone and surface of an implant under load" and the start of "modern implantology" (Brånemark, 1985) [1] [2]. In the early 1960s, after three decades of research and development, consisting of clinical and laboratory studies, an dental implant technique "capable of replacing missing natural teeth with elements similar to dental roots" was established [1]. The discovery that led to the definition of osseointegration was a study of bone by in vivo optical microscopy: a metal optical chamber, made of titanium, was incorporated into the tibia of a rabbit. After the consequent regeneration of the bone, the chamber was removed and it was noticed that it had been "incorporated" into the bone. There was also perfect adhesion between the bone tissue and the irregularities of the titanic surface. Subsequent experiments led to the fabrication of dental implants using titanium screws (Fig. 2.8). There is an affinity of bone with titanium and the oxide layer that forms on its surface. Different bonds, such as van der Waals forces, hydrogen bonds and local chemical bonds, have the ability to unite the biomolecules to the TiO2 layer [2] [172]. Since the 90's, the experimentation of new possible biocompatible materials with the human body has been started. Given the negative effects of TiO2, such as the retraction of the gum towards the prosthesis therefore an effect not aesthetically pleasing; problem of the metal-taste; problem of a possible migration of metal particles in the human body. New possible ways for more efficient osseointegration have been studied using metal-free materials such as Zirconia ZrO_2 in the case of dental prostheses [173].

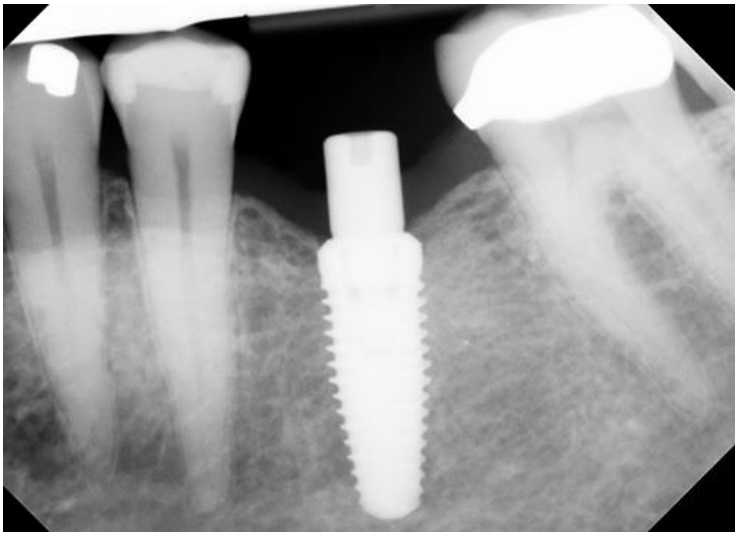

Figure 2.8: X-ray image of a dental bone implant integrated in the jawbone [174]

2.6.3 Factors that influence osteointegration

The process of osseointegration on an implant surface involves rather complex stages and the involvement of many factors. Among the most important are the microstructure and surface chemistry, which influence the process both quantitatively and qualitatively. Studies by Osborn and Newesley [1] have shown that bone neoformation occurs through two phenomena, distance osteogenesis and contact osteogenesis. In the first case, the release of the extracellular matrix and the subsequent mineralization made by the osteoblasts takes place in a direction that goes from the bone to the implant, i.e. the bone gradually surrounds the screw. In the second process, osseointegration occurs in the opposite direction, from the implant to the bone [2]. Once the cells have polarized, extracellular matrix production begins, with the aim of giving a precise structure to the bone-implant interface, which, after calcification, is transformed into an osteoid matrix and finally into bone tissue. Methods of roughening the surface have been developed to ensure proper and satisfactory osseointegration. Rough surfaces are preferred to smooth surfaces because they absorb more of the biomolecules involved in the processes described above. A rough surface favours cell adhesion and consequently proliferation. An example of this is the difference between climbing a smooth or rough mountain. If the wall is smooth it is almost impossible to climb, while if it is rough and therefore with handholds the climbing becomes easy. Cell adhesion works in the same way, the rougher the wall, the greater the cell adhesion.

Osteointegration is also linked to the concepts of osteo-induction and osteoconduction. The first definition indicates the stimulation of osteoprogenitor cells to the osteoblastic differentiation, a phenomenon that gives rise to osteogenesis, then "induces" it. Osteoconduction, on the other hand, concerns the growth of bone on a surface, and therefore implies the existence of more or less osteoconductive surfaces, i.e. surfaces capable of better or worse promoting the adhesion and adaptation of cells to the implant site. The success of a good osseointegration , i.e. the adhesion between implant and new bone), is the concrete result of a previous osteoinduction and osteoconduction [174].

2.7 Bacterial inflammation on prosthesis

The long-term maintenance of osteointegration depends on the state of health of the peri-implant tissues. Inflammation of peri-implant tissues due to bacterial inflammation may lead to marginal bone resorption. Oral hygiene aims to eliminate pathogenic bacteria that can cause inflammation of the peri-implant mucosa and loss, even partial, of osseointegration. The behaviour of the peri-implant mucosa depends on the quality of the soft tissues, the depth to which the implant is immersed, the type of surface material of which the implant is made and the morphology of its surface (rough or smooth) [175].

Inflammatory lesions that develop in the tissues around implants are recognized as peri-implant diseases. Peri-implant disease comprises two forms: *Peri-implant* mucositis corresponding to gingivitis; defined as a reversible inflammatory reaction of the soft tissues surrounding a working implant. *periimplantitis* (Fig. 2.9) corresponding to peri-implant disease; definite as inflammatory reactions associated with loss of supporting bone tissue around a working and irreversible implant [176] [177]. Therefore the periimplantitis is an inflammatory disease where, the bacteria cause an infection of the soft and hard peri-implant tissues that lead to a progressive retraction of the bone until then the implant is expelled. The implant becomes unstable and has to be removed. Periimplantitis usually occurs after 5 to 6 to 7 even 9 years. This disease also causes biological damage, both to the jawbone and the mandible. The treatment of periimplantitis is prevention, there is no treatment. Periimplantitis forms more easily if the surface is rough because the bacteria adhere more easily to the surface. Consequently, the only possible treatment is to do a small operation removing the bacteria and consequently smoothening the implant surface, so as to avoid future bacterial adhesion. The

aim is to transform the rough surface into a smooth surface that has much less adhesion to bacteria. This is the treatment, however, is only effective in 50% of cases. The reason for using rougher surfaces than is to ensure a faster osseointegration, thus a faster patient rehabilitation [178] [179].

Figure 2.9: Effect of peri-implantitis; the image shows bone loss caused by bacterial inflammation.

2.9 Cellular and bacteria test

2.9.1 Osteosarcoma cells (SAOS-2)

SAOS-2 is a human tumour cell line first isolated in 1973 by Fogh [180], specifically tumour Osteoblastic cells. This allows a large number of cells to be obtained in a very short time; they can also easily differentiate the same way in which osteoblasts naturally differentiate themselves. These characteristics allow the use of SAOS-2 for the study of bone tissue growth. Furthermore, SAOS-2 is ideal for the study of bone tissue development in vitro because of its ability to produce an extracellular matrix competent for mineralization [181] [182] [183].

SAOS-2 has been shown to have a collagen structure very similar to that synthesized by human osteoblasts, while lysine is in a state of hydroxylysine caused by the enzyme lysyl hydroxylase (modification of the protein structure: glycosylation of lysine) [184] [185] .
Another important feature is that the activity of alkaline phosphatase which is still high over time. The alkaline phosphatase present in the extracellular matrix completes the process of bone mineralization, promoting the deposition of the mineral material on the organic matrix of the bone being formed. As regards growth factors and cytokines, the values of the SAOS-2 cell line are comparable to those of normal osteoblasts [186].

2.9.2 Staphylococcus epidermidis bacteria

Staphylococcus epidermidis bacteria were used to analyse the interaction between the surface of the ceramic material and the bacteria. Staphylococcus epidermidis bacteria were used to analyses the interaction between the surface of the ceramic material and the bacteria, but not only, a detailed analysis is also carried out on the antibacterial activity of this type of ceramic surface. Staphylococcus epidermidis are gram + bacteria belonging to staphylococci family (cluster growth), diameter 8-1.5μm with production of colonies of 2-3mm. They are usually present on the human skin and in the mucous membranes. They are potentially pathogenic and manage to be dangerous as they can lead to infection if they can penetrate inside the human body (during surgery or due to wounds).
Staphylococcus epidermidis need to be cultivated like other staphylococci in common culture media and the optimal growth temperature is around 25-40 °C with an optimum between 30 and 37 °C. Staphylococcus growth is usually favoured at neutral pH between 6-0-7.0. The pH of the saliva is between 6.7 -7.4 [187].
S. epidermidis is able to adhere to the synthetic surfaces of biomaterials and to form a stable biofilm that leads to persistent infections [188] [189]. They are therefore able to adhere also dental implants of Ti or ZrO_2 [190]. The bacteria during the formation of the biofilm, secrete extracellular polymeric substances that include lipids, proteins, polysaccharides and others. These substances protect the bacterial colony from external attacks [191] [192]. Treatment of biofilm-related infections is extremely difficult. Moreover, the immune system is inefficient in eliminating bacterial inflammation that requires extreme doses of antibiotics. Biofilm contains

bacteria up to 1000 times more resistant to bactericidal drugs than their planktonic predecessors [193].

In addition, bacteria released from biofilm often trigger remote secondary reactions to some patients who have compromised immune systems. The need therefore arises to use biocompatible materials capable of eliminating the serious problem of bacterial contamination.

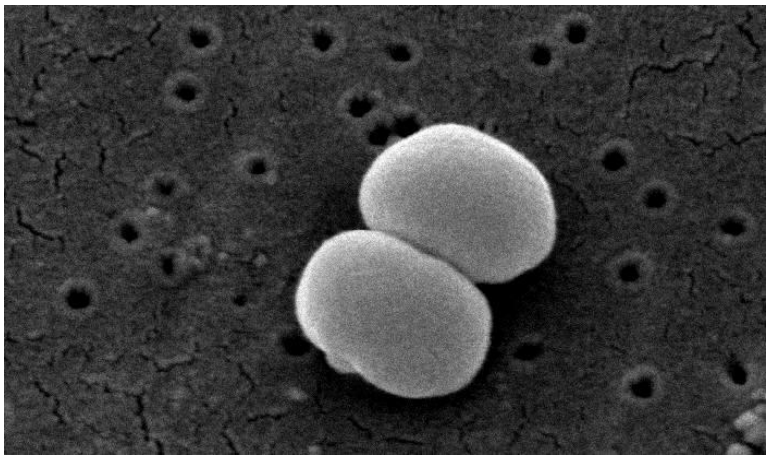

Figure 2.10: Staphylococcus epidermidis

Chapter 3

Methods

3.1 Introduction to Spectroscopy

The photons of electromagnetic radiation can interact with matter. Following this phenomenon, the radiation can spread, be absorbed or not interact with it. If the photons have energy greater or equal to the energy gap between the ground energy state and the excited state, absorption can occur. Instead the scattering does not require an energy absorption, the interaction can take place anyway. In particular, the study of the intensity and frequency of photons before and after interactions with matter is the basis of all optical spectroscopic techniques.

Raman spectroscopy utilizes scattering as a physical effect which can give some information about the materials and molecules analysed, such as its distribution and size, and molecular identification is also possible. An electromagnetic radiation with a broad spectrum from NIR to UV is used and the energy difference between the two different energy states is measured.

FT-IR spectroscopy exploits the absorption of a radiation of the infrared region through a photon that causes the direct excitation of the molecule from a low energy state to an excited one. The frequency of the radiation corresponds to that of a vibration. Other spectroscopic techniques exploit the adsorption process such as X-ray absorption spectroscopy, NMR, acoustic spectroscopy.

Electromagnetic radiation can be described according to a physical description as a wave-particle dualism that propagates in space at a constant speed, through physical vestments such as: wavelength λ, frequency v, amplitude and velocity. The electromagnetic radiation, therefore, can be thought of as particles with discrete energies called photons. The physical relations between these vestments and photonic energy are described by the relations:

$$\lambda = c / \nu \tag{3.1}$$

$$\nu = 1 / \lambda = \nu / c\,\nu \tag{3.2}$$

$$E = h\nu\,\nu \tag{3.3}$$

Where h represents the Plank constant (6.63 x 10-34 J s), ν the frequency (Hz), c the speed of light (3.0 x 108 m/s) and λ the wavelength and ν the wavelength number. The electromagnetic spectrum has been divided into different categories of electromagnetic radiation. The narrow energy band of electromagnetic radiation visible to the human eye is called visible light. Figure 3.0 classifies the bands into an electromagnetic spectrum, including, γ, X-rays, ultraviolet, visible, infrared, microwave and radio, all with different energies.

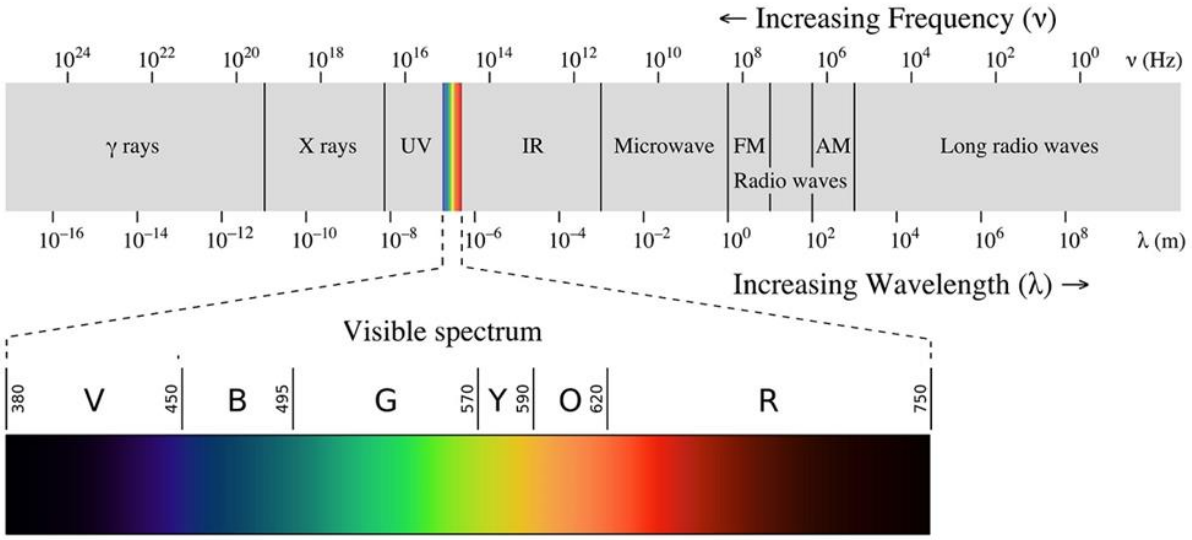

Figure 3.0: The electromagnetic spectrum associated with different types of radiation.

3.1.1 Raman and Fourier-Transform Infrared Spectroscopy

It is considered a hetero-nuclear hetero-atomic molecule A-B consisting of two atoms of mass m1 and m2 bound by a spring of elastic constant k. For a discussion of classical physics, the atoms vibrate following Hook's law. The relation of the vibration frequency "ν" between the two atoms is calculated:

$$v = \frac{1}{2\pi c}\sqrt{\frac{k}{\mu}} \tag{3.4}$$

Where μ is the reduced mass of the atoms and k is the force constant of the A-B bond representing the bond under vibration. ν is the frequency of the vibration of the bands observed in the spectra, increases with the stiffness of the bond, but decreases as the reduced mass increases. The vibrational energy is quantized because the energy assumes discrete (quantized) energy levels according to the relationship:

$$E_n = \left(n + \frac{1}{2}\right) hv \tag{3.5}$$

Where h is Planck's constant, v is the quantum vibrational number (it assumes positive integers: 0, 1, 2, 3...) and defines the discrete energies allowed to the system and ν is the vibration frequency. The energy potential is described through a parabolic harmonic oscillator model and presents the vibrational energy levels equally separated by the constant quantity hv and the vibrational levels are infinite. With v=0 E0= hv/2 (zero-point Energy) whose existence is required by Heisenberg's uncertainty principle The model of the harmonic oscillator is a simplification with respect to the real vibrational motion, because at r which tends to 0 the atoms cannot penetrate, while at r which tends to ∞ the molecular bond splits. The energy potential in a real model is described by the harmonic oscillator of Morse (Fig. 3.1), in which the distance between the levels is not constant is progressively reduced as v increases and the vibrational levels are finite.

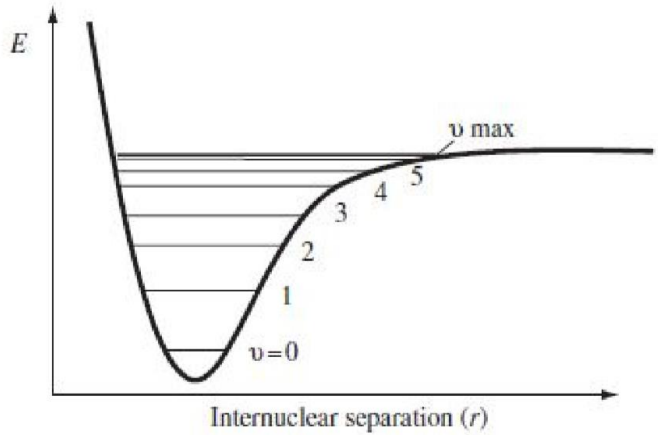

Figure 3.1: Energy potential described by the harmonic model of the Morse oscillator.

The possible vibrations of a polyatomic molecule made up of N atoms depend on the number of degrees of freedom (or vibrational modes) of the molecule itself: it has 3N degrees of freedom of which 3 are translational and 3 rotational (2 in linear molecules): the molecular vibrational modes are therefore 3N-5 if the molecule is linear and 3N-6 if it is non-linear. There

are two modes of molecular vibration: stretching (stretching) and bending (bending), of which there are twisting, rocking (oscillation in the plane) and wagging (oscillation outside the plane). Usually, the stretching frequencies are at higher values than the bending frequencies because more energy is needed to stretch the bonds rather than bend them.

The difference between the two spectroscopic techniques lies in the sensitivity to two different parameters: Raman spectroscopy is sensitive to the variation in the polarizability of the molecule during vibrational motions, while IR is sensitive to the variation in dipole momentum. Using the selection rules, it is possible to predict whether a molecular vibration will be Raman or IR active. In the presence of a centre of symmetry, molecular vibrations symmetrical to the reversal centre of the molecule are prohibited in IR and allowed in Raman, and opposite. This phenomenon is known as the principle of mutual IR/Raman exclusion. According to the mutual exclusion rule: no mode can be simultaneously active Raman and IR.

The selection rules of Raman spectroscopy are different from those of IR spectroscopy. For IR spectroscopy a transition between 2 vibrational levels is allowed when the transition moment associated with it is different from zero, according to the relationship:

$$\int \Psi j \, \Theta \, \Psi i \, d\tau \neq 0 \tag{3.6}$$

where Ψj and Ψi are the autofunctions of the final (j) and initial (i) vibrational states, while Θ is the transition moment operator. IR absorption occurs if there is a change in the dipole moment μ during a vibration along a generic Q coordinate:

$$\left(\frac{\partial \mu}{\partial Q}\right) \neq 0 \tag{3.7}$$

In the case of Raman spectroscopy the selection rules depend on the variation of the polarizability tensor α along the normal reference coordinate Q. Therefore, an active vibration results if during the vibration along a generic coordinate Q there is a variation of the polarizability (α) of the molecule; so that there is Raman scattering:

$$\left(\frac{\partial \alpha}{\partial Q}\right) \neq 0 \tag{3.8}$$

$$\mu = \alpha E \tag{3.9}$$

Where α is the polarizability of the molecule, μ is the induced dipole moment, E is the electric field. However, the probability of creating an induced dipole is not equal in all directions the polarizability α is a tensor of rank two obtainable from the relation between the components of the induced dipole and those of the electric field; explained in the matrix:

$$\begin{bmatrix} \mu_x \\ \mu_y \\ \mu_z \end{bmatrix} = \begin{bmatrix} a_{xx} & a_{xy} & a_{xz} \\ a_{yx} & a_{yy} & a_{yz} \\ a_{zx} & a_{zy} & a_{zz} \end{bmatrix} \cdot \begin{bmatrix} E_x \\ E_y \\ E_z \end{bmatrix} \quad (3.10)$$

where the matrix containing the terms α is called the polarizability tensor.

3.2 Raman Spectroscopy

Raman spectroscopy owes its name to the Indian physicist Chandrasekhara Venkata Raman, who first observed in 1923 how a small fraction of the radiation scattered by certain materials had different energy from that incident [194]. He realized that the difference in energy was due to the chemical characteristics of the material under analysis. In 1930, following this discovery, he was awarded the Nobel Prize for Physics.

Raman spectroscopy is a non-destructive, non-invasive technique that needs a small sample volume (about 1µm3). In addition, it offers the possibility to use a wide spectrum of laser sources, ranging from ultraviolet (UV) to near infrared (NIR). Raman spectroscopy covers a wide range of applications and the spectrum obtained, called the Raman spectrum, provides a "fingerprint" of the molecule under examination, allowing its identification [195] [196].

The main advantage of the Raman technique compared to IR is that the water is practically transparent Raman and therefore aqueous samples can be analysed as they are. The glass has a weak Raman absorption and it is possible to analyse aqueous samples in simple test tubes. In addition, the analysis of solid samples does not require special sample preparation in Raman spectrometry. For example, pharmaceutical products can be analysed as they are, in their final form for consumption. This makes Raman a potentially useful technique for process control. The Raman spectrum of active products is also generally much more intense than that of excipients. Therefore, Raman spectroscopy finds an increasing number of applications in the pharmaceutical field and in materials science. Most Raman peaks are in the range between 150÷3500 cm-1. It is thus possible to identify the chemical composition of an unknown sample, by comparison with standard spectra, but also to characterize the different state of aggregation of the molecules. Raman analysis allows a non-destructive analysis of the material which is a great advantage in research and development because the available sample quantities are often limited. However, the main applications of Raman remain in the biological and medical sector, where samples with a high water content must be analysed.

3.2.2 Raman theory

Raman spectroscopy allows to obtain information about the structure and composition of the sample, and this is due to the fact that the Raman spectrum contains peaks for frequencies corresponding to the vibrational modes of the molecules under examination [197]. In particular, Raman spectroscopy is used for the study of "intramolecular" modes (molecular properties) and intermolecular modes (crystalline lattice properties) [198]. Furthermore, through polarized light measurements it is possible to investigate molecular order, anisotropy, alignment and molecular self-organization and crystalline domains. It is used for mapping sample surfaces to monitor the spatial distribution of structural inhomogeneities (chemical, physical, mechanical, etc.) with a spatial resolution of the order of one μm [198].

The principle on which the Raman technique is based is the scattering of a monochromatic radiation incident on the sample. Considering the radiation-matter interaction in terms of particles, the scattering can be of two types: elastic or inelastic. In the first case it is called Rayleigh scattering, i.e. without net energy transfer, the scattered photons have the same energy as the incident photons and is the most frequent event. Instead, inelastic scattering is called Raman scattering, i.e. there is an energy transfer between the incident photon and the molecule. This interaction occurs on a limited number of events, about 1 in 10^6 [198]. Raman scattering can occur as Raman Stokes or Raman anti-Stokes scattering. In the first case the molecule decays to an excited $h\nu_0$-$h\nu_m$ vibrational state, emitting a photon with less energy than the incident one. Instead in the Raman anti-Stokes scattering the molecule already present in an excited vibrational state (E_0+$h\nu_m$) decays from the virtual state to the fundamental state emitting a photon with energy $h\nu_0$+ $h\nu_m$, higher than the incident one (Fig. 3.2).

It is important to underline that Raman dispersion is very different from fluorescence (Fig. 3.2). In Raman spectroscopy the photon is released instantly, while in fluorescence, the incoming photon is completely absorbed by the molecule and causes a change of state of the electronic energy. It is then released when the molecule relaxes again in a lower energy state.

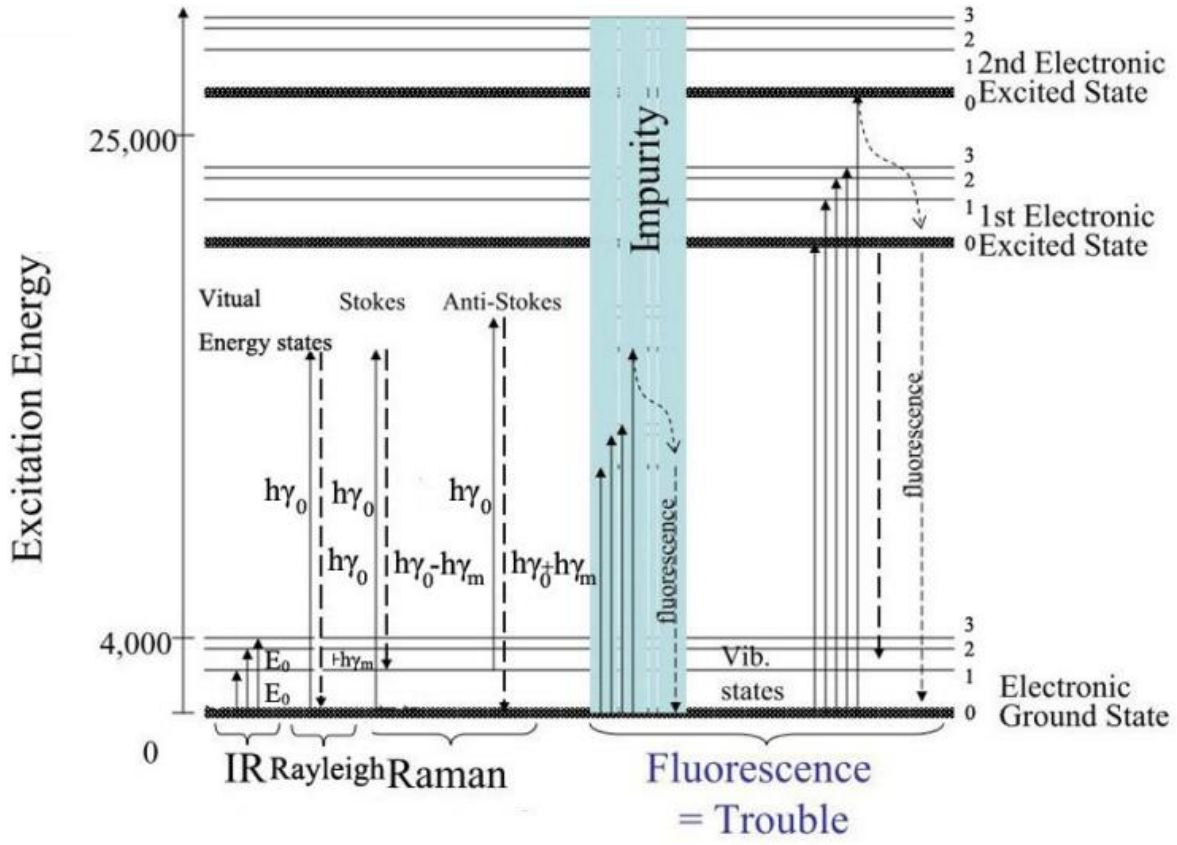

Figure 3.2: Scheme on the different energy states described by the Raman effect (Stokes, anti-Stokes, Rayleigh dispersion) IR effect and fluorescence.

The Rayleigh scattering, does not provide any information since it is at the same frequency as the incident radiation hv0 (elastic scattering). It is subject to coherence effects that make it much more intense than Raman scattering, which is fundamentally inconsistent. Moreover, the Stokes and anti-Stokes lines are symmetrical with respect to the Rayleigh line. In order to analyse the vibrational modes of a molecule, a Raman-shift analysis is performed; the difference between the frequency of the incident radiation and that emitted by the sample under analysis is studied. At room temperature, the fundamental vibrational level is more populated, therefore Stokes lines are more intense than anti-Stokes because Stokes lines start from the fundamental state, while anti-Stokes lines start from an excited state. This is demonstrated by Boltzmann's distribution, which links the probability distribution of the population in energy levels. Stokes lines are related to the functional groups of the molecule and those more analysed in common Raman spectra. According to the Boltzmann distribution:

$$\frac{Nn}{Nm} = \frac{gn}{gm} exp\left[\frac{-(En - Em)}{kT}\right] \quad (3.11)$$

Where Nn and Nm are the number of molecules in the vibrational energy level: excited (n) and ground (m). g is the degeneration of n and m levels; (En – Em) the difference in energy between the two energy levels and k is Boltzmann's constant (1.3807×10^{-23} JK-1). When Anti-Stokes scattering occurs, the molecule is in an excited state, but the Nn population is negligible compared to Nm, so the intensity of the Anti-Stokes signal is small compared to the Stokes signal Fig. 3.3 [199].

Although the rarity of anti-stokes photons generates much weaker anti-stokes lines, they are sometimes favoured in the analysis due to the absence of fluorescence interference, which could be a problem for stokes lines.

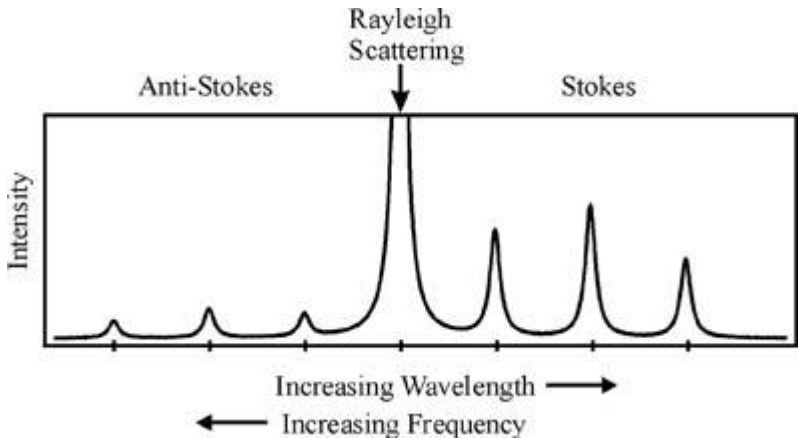

Figure 3.3: Example of a Raman spectrum containing the Stokes , anti-Stokes and Rayleigh scattering bands.

In summary, the electromagnetic radiation interacts with the electronic cloud surrounding the molecule. Only if there is a non-symmetrical variation in the distribution of the electronic cloud, due to the vibratory motion of the atoms with respect to the equilibrium position, is there an exchange of energy between the radiation and the molecule. The vibrational motion is present in both homonuclear and heteronuclear biatomic molecules and a non-symmetrical variation of the electronic distribution is generated (as previously described). Each molecule can therefore be classified in relation to its elements of symmetry. The point group to which the molecule belongs is thus assigned and can be used to predict which bands are active Raman and IR. Therefore the elements of symmetry are distinguished in: E; Cn; σv; σh; i; Sn. Molecules that have the same elements of symmetry belong to the same group of symmetry.

3.2.3 Instrumentation

The Raman instrumentation is able to record the collected Raman spectra and generally consists of five main components. The first two elements include a source of monochromatic light and a microscope device: the incident light is focused and the Raman light is collected; a spectrograph: once the light information is collected it is divided into a frequency spectrum; a detector: the light is transduced into an electrical signal; a software: displays the frequency spectrum that acts as a visual interface. Other two important components are the "notch filter" whose function is to eliminate the Rayleigh elastic dispersion from the final spectrum and "optical polarizer" which collects the information of the Raman scattering. A laser is the typical source of a Raman instrument whose frequency can vary from UV to NIR. The incoming laser is focused on the "notch filter" which at a correct angle reflects it on the sample. The incident radiation produced finds the filter that only allows the Raman radiation to pass through. The Raman radiation then passes through the monochromator and is then captured by the detector. Usually the detector is CCD (charged-coupled device) which function is to count the photons and convert the information into an electrical signal, which, subsequently the software processes. The experiments done in this thesis were carried out using a micro-Raman spectrometer (T-64000, Horiba/Jobin-Yvon., Kyoto, Japan) with an excitation source emitting at 532 nm operating at a power of 10 mW (Nd:YVO4 diode pumped solid state laser; SOC JUNO, ShowaOptronics Co. td., Tokyo, Japan), at room temperature and in backscatter conditions. An example of instrumentation is shown in Fig. 3.4.

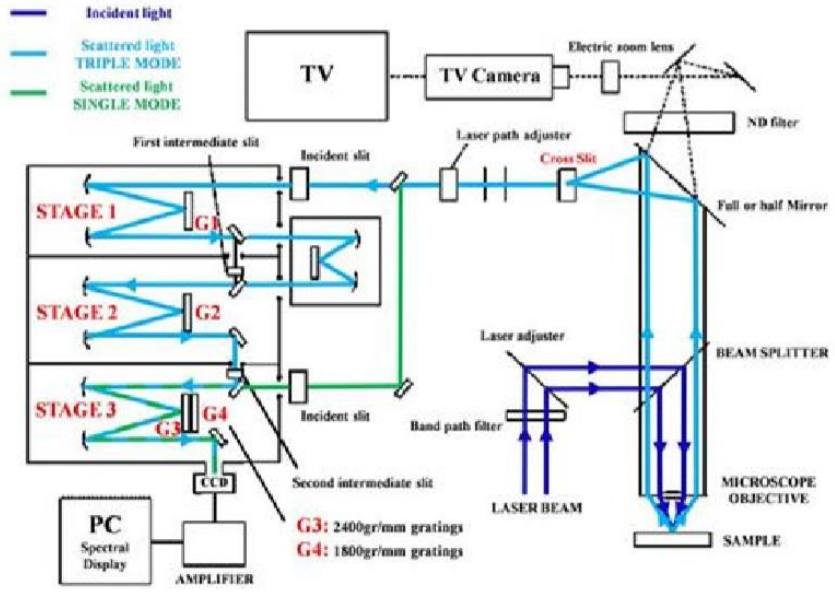

Figure 3.4: Scheme concerning the operation of T64000 spectrometer.

This instrument for increasing optical stability and spectral resolution has a triple monochromator. There is also a set of holographic diffraction gratings of 2400 gr/mm, 1800 gr/mm and 600 gr/mm. The diffraction lattice of 2400 gr/mm allows to obtain, during spectrography, the range and the wavelength resolution that the instrument can manage. In fact, the number of grooves improves the dispersion of polychromatic light; moreover, depending on the grating used, the spectral band width is modified. The T64000 spectrometer can be used with either a single or triple monochromator; for the triple configuration it consists of two double pre-chromators and a spectrographic stage; for the single monochromator configuration the elastic scattering (Rayleigh) is eliminated from the notch filter, then the first two steps are ignored. Through an electric motor it is possible to move along x and y and choose the point to analyse. Spectrum acquisition requires a 1024 x 256 pixel CCD detector cooled to 140 K with liquid nitrogen and mounted in the output image plane (CCD-3500V, Horiba Ltd., Kyoto, Japan). An optical microscope is used to focus the laser beam on the sample. It has three different long focus objectives: 100x with NA=0.9, 50x with NA=0.X 20x with NA=0.9. The diffused radiation is separated from incident beam and collected in backscattering configuration through the use of a beam splitter. T64000 can operate in confocal mode thanks to Raman modulation. The confocal microscopy patented by Minsky in 1957 [200], is used in Raman spectroscopy and other imaging microscopy [201] Fig. 3.5.

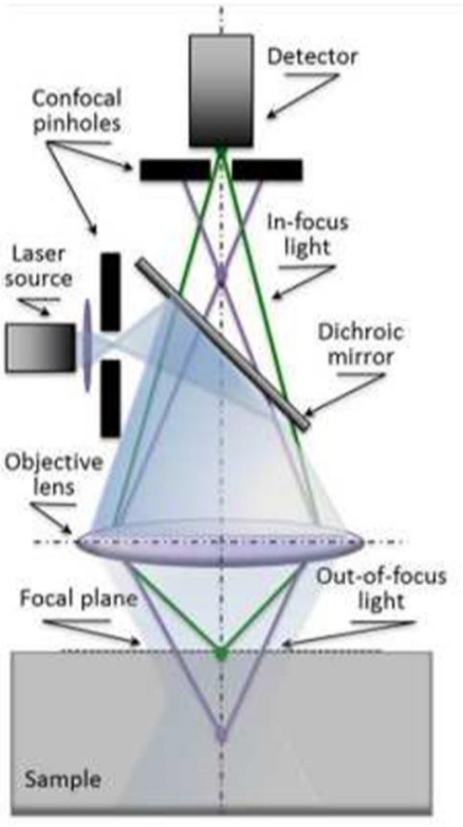

Figure 3.5: Schematic draft of the confocal configuration for Raman assessments.

It has two pinhole filter holes that allow to exclude light from out-of-focus planes. The first hole improves the Gaussian shape of the probe and is placed in the path of the laser beam, while the second improves the spatial resolution (lateral and axial) and is placed in the output focal plane of the microscope. The signal produced at the aperture passes without significant attenuation and is brought from the surface to a focus, consequently, the out-of-focus light is cut because it is brought into focus before the aperture. The advantages of this technique are an improvement in the noise/signal and an increase in resolution.

3.3 Fourier Transform Infrared Spectroscopy

The IR spectroscopy as already briefly discussed in the introduction, is an absorption spectroscopy. Since, only when the electromagnetic radiation has the exact energy to pass the molecule to the highest energy state does absorption take place. The energy of the vibrational levels is associated to the molecular structure, it follows that, by observing which energy is absorbed by the molecule, it is possible to deduce which are the main functional groups of a molecule and therefore to determine its chemical nature (Fig. 3.0). The vibration modes of the molecule are essentially two: stretching vibration; due to rhythmic stretching along the bonding axis and bending vibration; due to variation of the bonding angle.

Infrared radiation is divided into NIR (13000 - 4000cm^{-1}), MIR (4000 - 400cm^{-1}) and FIR (400 - 10cm^{-1}). The IR spectrum is present in the MIR region. The vestments that characterize the absorption bands are: the position that depends on the force constant (3.4), the intensity that describes the probability that the energy transition that causes the absorption takes place, it can be strong, medium or weak. Moreover, the shape of the band that can be sharp or broad, it depends on the vibrational structure. In a typical infrared spectrum in abscissa we find the wave number of the incident photon, and in ordinate the transmittance.

FT-IR spectroscopy can capture all frequencies of the IR spectrum in the detector at the same time, which makes scanning the wavelength unnecessary. It uses an interferometer, which transforms the polychromatic IR radiation emitted by the source (instant by instant with the same intensity) into an interferogram, where absorption is no longer a function of frequency, but of time (i.e. it changes from frequency domain to time domain). Contrary to traditional spectrophotometers, therefore, in this equipment there is no dispersion monochromator, but Michelson's interferometer is used, which produces the interferogram of the substance under

examination during the scan (Fig. 3.6). The first interferometer was created in 1891 and only a year later the correlation between the interferogram and the IR spectrum was defined, thanks to a mathematical operation: the Fourier transform. Only with the advent of computer calculation it was possible to develop FT-IR which allowed the development of the Fourier Transform. In the operating principle the energy coming from a conventional IR source is collimated and directed towards a beamsplitter, that is a semi-transparent mirror, which is usually a very thin germanium film supported by a potassium bromide substrate. An ideal beamsplitter reflects 50% of the incident light and transmits the remaining 50%, thus creating two distinct optical paths.

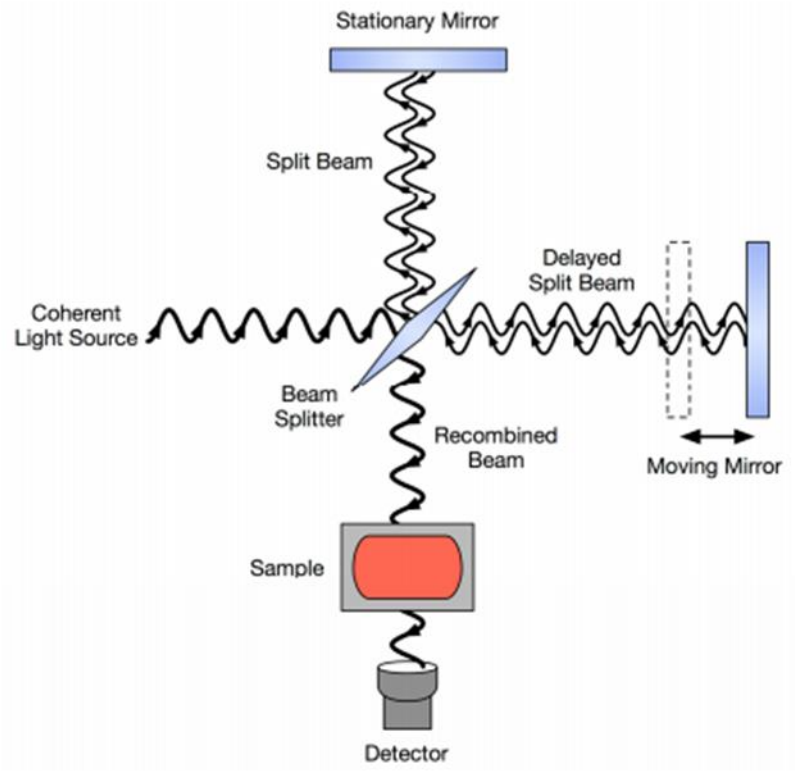

Figure 3.6: Michelson's interferometer for FT-IT spectroscopy features the components: a detector, a coherent light source, a fixed mirror, a moving mirror and a beam splitter.

Figure 3.6 shows how, experimentally, about 50% of the radiation affects a fixed mirror while the other half affects a moving mirror that flows along an "x" direction at a constant speed. The rays reflected by the two mirrors intercept the semi-transparent mirror again and recombine in one point, interfering with each other. The resulting beam is sent first to the sample and then to the detector.

When the moving mirror moves it can cause destructive or constructive interference with the two radiations. This is very important because in the absence of the sample, the detector records an absorption spectrum related to water vapour, CO2 and impurities of various nature present

in the air. This spectrum, called background, is stored and then subtracted from the spectrum performed on the sample.

The most significant advantage of FT-IR spectrophotometry is certainly the signal to noise ratio: while the background noise is random, the signal is constant and all frequencies are analyzed simultaneously. The speed has also made many applications possible, especially in those cases where the sample is available for analysis for short periods of time, such as kinetic studies with unstable intermediates, observations on gas chromatographic column eluates or the use of FT-IR variable temperature microscopy. Further advantages are that it is possible to accumulate spectra and thus decrease noise, that the laser is used for each single scan and that the resolution of the instrument is constant [202] [203].

3.4 Fluorescence Microscopy (FM)

3.4.1 Introduction of Fluorescence

Fluorescence is a radioactive decay by the release of a photon. According to the scientific treatment: when a molecule hit by an electromagnetic radiation absorbs a photon, the electron passes from a stationary energy state S_0 (singlet 1) to an excited one S_1 (singlet 1), then it transfers to excited energy levels. With S_0, S_1 we mean the states of singlet respectively the fundamental state and an excited state. This energy transition does not involve a change of wave function (ψ) within the molecule. This energetic transition must follow the rules of selection, if I start from a state of singlet I must arrive at a state of singlet (Keeping ψ constant) [204].

However, a given molecule can only absorb photons with a given wavelength because, as established by the energy conservation law, the energy difference between the two states must correspond exactly to the energy of the absorbed photon. The absorption happens however to major energy states, then it easily decays on minor energy levels until the resonant energy level [205] [204].

A molecule is in the state of singlet excited S_1, so excited it can dissipate its excitation energy in several ways: by vibration, phosphorescence then an internal conversion and by photooxidation. In the case of organic molecules that are in the excited state S_1, if the equilibrium geometry is different from the stationary state geometry, a decay through vibrations

is generated. For this reason, the organic luminescent molecules have to be rigid molecules able to contrast a vibrational decay. Phosphorescence, on the other hand, means an internal conversion through intersystem-crossing and a wave function (ψ). There is an internal passage from S_1 -T. Radioactive decay will occur at times slower than fluorescence [204].

Fluorescence is defined as a radioactive return (photon emission) from state S_1 to S_0. The photon emitted in the form of fluorescence generally has a longer wavelength (lower energy) than that initially absorbed. This is because the photon is positioned on the resonated energy level [204] [206]. The mechanism is schematized in Figure 3.7.

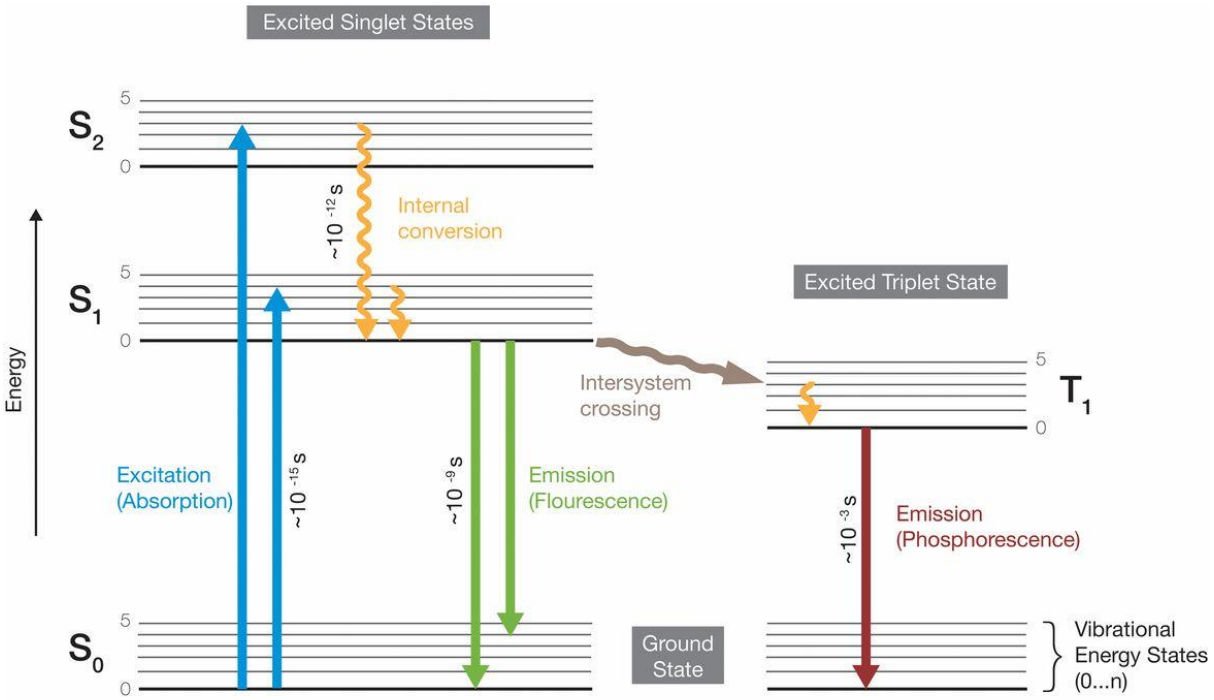

Figure 3.7: 2Jablonski's diagram; the graph shows the processes of: absorption through a photon S_0->S_1 (single in stationary state at excited); internal conversion, decay at resonant level; phosphorescence emission S_1->T through intersystem-crossing; fluorescence [204]

In various scientific fields, the phenomenon of fluorescence is now used as a non-destructive method to track or analyse biological molecules through an associated fluorescent emission. In our particular case, fluorescence is used as a population analysis of cells and bacteria present on the surface of the sample. Organic fluorescent molecules such as markers or stains are used [206].

3.4.2 Instrumentation

In fluorescence microscopy (Fig. 3.8), the main advantage is the possibility to have access to a "raw" data, represented by the image acquired through the use of a digital camera "CCD camera" (*f*). The cells are illuminated with a beam of light at a specific wavelength, such as the one absorbed by the sample (excitation wavelength), determining the emission of light at a different wavelength (emission wavelength). The wavelengths, excitation and emission, are characteristic for each fluorescent marker and can be selected and discriminated by using special filters or a monochromator. In a fluorescence microscope the light incident on the sample is typically emitted by a mercury vapour lamp "Light source" (*a*) that emits radiation in the low wavelength region of the visible and in the near ultraviolet. In the optical path, before reaching the sample, the radiation is conveyed and selected by a system of: "Excitation filter" (*b*), "Dichroic mirror" (*c*) and "Emission filter" (*d*). The "Excitation filter", allow to illuminate the sample with selected wavelengths coming from the light source, the "Emission filter" are instead chosen to block (absorb) the excitation wavelengths and allow to pass only the wavelengths emitted by the sample, finally the "Dichroic mirror" are specialized in efficiently reflecting excitation wavelengths and letting pass emission wavelengths [207] [208].

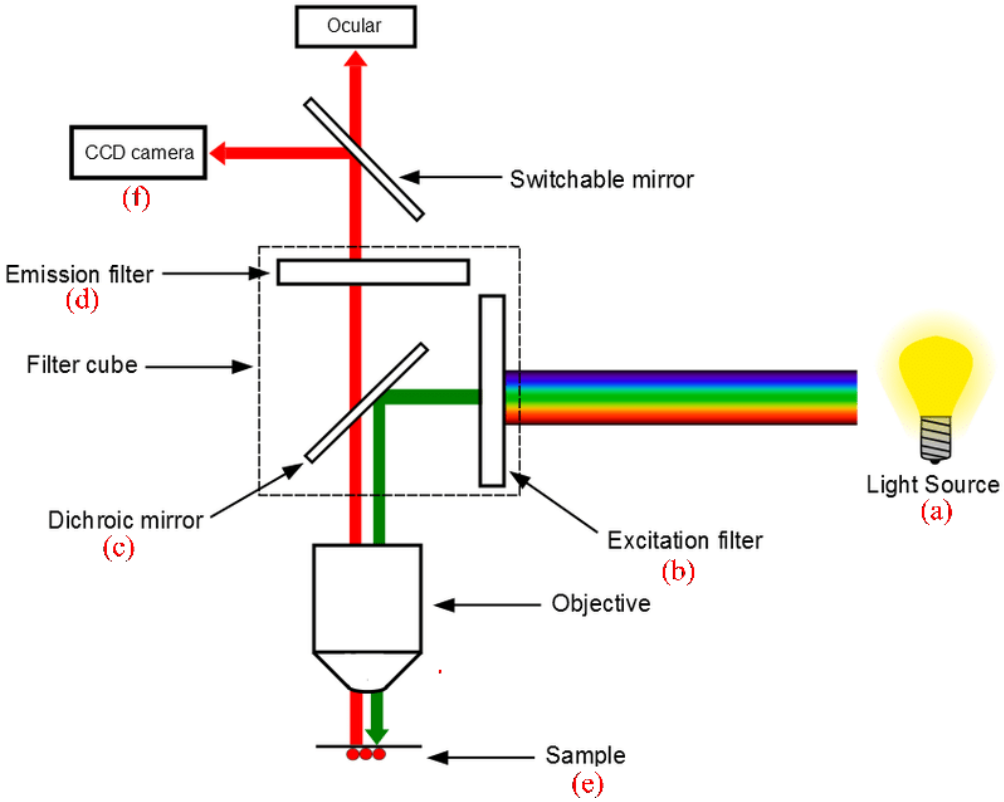

Figure 3.8: The microscope fluorescence instrumentation: (a) Light Source; (b) Excitation filter;(c) Dichroic mirror; (d) Emission filter; (e) Sample.

3.4.3 Markers and Staining techniques

For the development of this thesis work, The fluorescence microscope was used to characterize the surface, first colonized by bacteria, then colonized by cells. In the bacterial analysis, the bacteria were marked with DAPI, CFDA and PI respectively to analyse the population of total bacteria, alive and dead. A relevant study to be carried out in this context is related to the understanding of how antibacterial the surface is. In particular, the mechanism of application of the markers used were:

DAPI: colour blue; "4′,6-diamidino-2-phenylindole" binds to cell nuclei, then to the cellular DNA rich in A-T sequence. When bound to double-stranded DNA, DAPI has an absorption maximum at a wavelength of 358 nm (ultraviolet) and its emission maximum is at 461 nm (blue). As a result fluorescent microscope the cell nucleus is blue [209] [210].

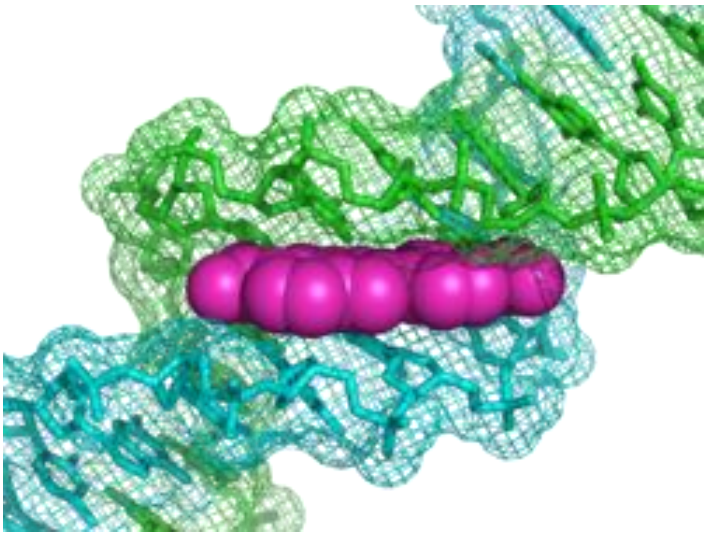

Figure 3.9: Mechanism of interaction of the DAPI marker with the DNA.

CFDA colour green; binds living cells, the mechanism of action is divided into two phases:

1- CFDA-SE enters cells by diffusion and is cleaved by intracellular esterase enzymes to form an amine-reactive product, CFSE.
2- CFSE enters the cytoplasm of cells, intracellular esterase remove the acetate groups and convert the molecule to the fluorescent ester. Enzyme esterase is a hydrolase enzyme that splits esters into an acid and an alcohol in a chemical reaction with water called hydrolysis. Only alive cells have an active esterase enzyme [211].

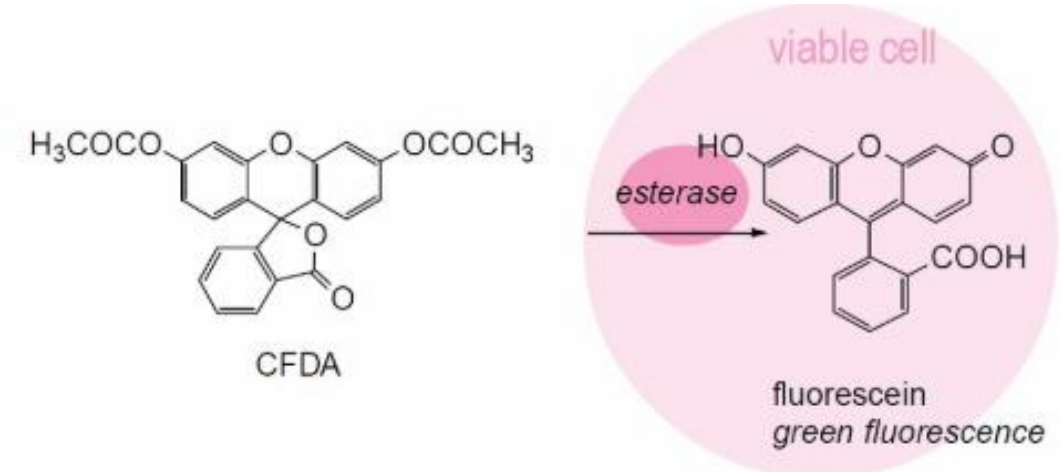

Figure 3.10: Reaction mechanism of the CFDA marker with the esterase enzyme.

PI colour red; "ropidium iodide " binds dead cells. PI binds to DNA by intercalating between the bases with little or no sequence preference. PI is not permeable to the membrane, which makes it useful to differentiate dead cells from alive cells based on the integrity of the membrane. PI binds to DNA by intercalating between the bases with little or no sequence preference. In aqueous solution, the dye has excitation/emission maxima of 493 / 636 nm. Once the dye is bound, its fluorescence is enhanced 20- to 30-fold, the fluorescence excitation maximum is shifted ~30–40 nm to the red [212] [213].

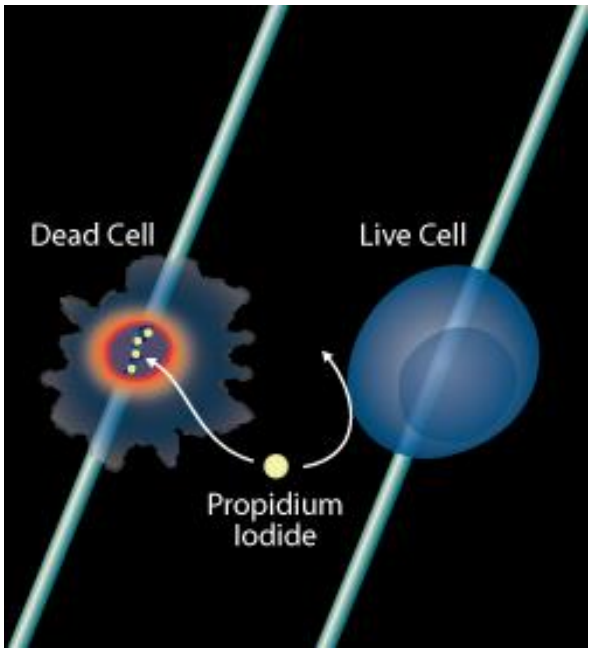

Figure 3.11: Mechanism of application of the PI marker; PI is not able to penetrate the cell membrane, but easily binds with DNA.

In order to analyse the cells, these were two stains of Osteopontine (OPN) and Osteocalcin (OC) and the DAPI marker to recognize the total number of cells. OPN and OC are two proteins released into the extracellular matrix of osteoblastic cells during the bone formation phase. They have the function of modulating this process of formation, mineralization and adhesion between the cells and the bone matrix [214]. In order to evaluate the condition of the bone tissue they are the specific proteins. For the thesis project these are important parameters for knowing the speed and quality of osseointegration for a dental implant; in particular:

*OPN (*Osteopontine)*:* green colour; it is a protein present in all mammals and binds to hydroxyapatite and provides the basic structure (matrix) for the bone. It binds the components of the extracellular matrix (hydroxyapatite), then it participates in the mineralization of the tissues and promotes the deposition of calcium phosphates in the bones [215].

*OC (*Osteocalcin): red colour; it is an extremely specific protein which, during the mineralization phase of the bone, binds calcium ions Ca^{2+}.

3.5 Scanning Electron Microscopy (SEM)

The Scanning Electron Microscopy (SEM) coupled with the Energy Dispersive X-ray spectroscopy (EDX spectroscopy) is an electro-optical instrument that allows, after the emission of an electron beam, to analyse the various signals produced by the interaction of the electrons in the beam with the sample under examination. The processing of these signals allows to obtain a wide range of information not only morphological, but also compositional and structural relating to the various parts of which the sample is made.

The scanning electron microscope does not use light as a source of radiation, but a beam of primary focused electrons that hit the sample. The primary beam is not fixed, but scans the surface of interest: it is driven in sequence, point after point, line after line, over a small rectangular area of the sample. In the interaction between the primary beam and the atoms constituting the sample, numerous particles are emitted, among which the secondary electrons [216]. These electrons are captured by a special detector [217] and converted into electrical pulses that are sent in real time to a screen (a monitor) where a similar scan is performed simultaneously. The result is a black and white image with high resolution and great depth of field, which has characteristics similar to those of a normal photographic image. For this reason, SEM images are immediately intelligible and intuitive to understand. The SEM microscope can

obtain images that appear almost three-dimensional even for relatively large objects (such as an insect). The resolution power of a normal SEM electron microscope with tungsten cathode is around 5 nm, but some models reach 1 nm. The sample is under high vacuum (10-5 Torr) because the air would prevent the production of the beam (given the energy labass of the secondary electrons), and must be conductive (or metallic), otherwise it would produce electrostatic charges that would disturb the detection of the secondary electrons.

The other signals emitted by the sample following the excitation of the primary electron beam are: backscattered electrons (backscattering phenomenon), X-rays, electron-channelling, cathodoluminescence, beam-induced currents and, for some types of samples, even transmitted electrons. With regard to microanalysis (EDX spectroscopy), the X-rays emitted by the sample are exploited because of the accelerated electron beam incident on the sample itself [218]. The instrumentation used for the characterization of the powders described in the previous chapter has two types of detectors, one sensitive to secondary electrons and one sensitive to X-rays emitted by the sample because of the primary electron beam. The latter is arranged in such a way as to receive the maximum level of absorbable radiation and can be of the wavelength dispersion (WDS) or energy dispersion (EDS) type. Each of them has its respective advantages and disadvantages:

WDS detector: it exploits the undulatory characteristics of the X photons. It consists of a curved crystal, the "Rowland circle, with a certain pitch of crystal lattice, on which are arranged the sample and the photon counter. following the law of Bragg, only a certain wavelength will then be reflected on the counter, wavelength that can be varied by rotating the detector:

EDS detector: exploits the energy interaction between X-rays and a suitable material. It is characterized by a monocrystal of silicon-doped lithium, coated at both ends with a conductive layer of gold, kept in high vacuum and at a temperature of -192 ° C with liquid nitrogen. High purity germanium crystal represents a more efficient modern evolution. The operating principle exploits the production of electric current, which is significantly amplified, generated by interaction between crystals and photons. These are the most widely used detectors today.

The resulting image consists of an X-ray spectrum, from which one can trace the chemical composition of the analysed material since each peak of the spectrum can be traced back to a very precise atomic species [218]. X-ray radiation results from the ionisation of the atom in the innermost orbits by the incident beam. A primary electron (incident) can expel an electron from the orbital K, L or M of the atom, losing at the same time, by inelastic diffusion, the energy EK, EL, EM, corresponding to the orbit of the electron with which it interacted. The ionized atom will be able to regain its stability by going down to lower energy levels, either through the

occupation of the gap by more external electrons, with concomitant emission of the corresponding photon X, or through the emission of another electron that has absorbed the energy just released (electron Auger).

The emitted X radiations are characteristics of the atom that produced them and allow their recognition. Since the electronic bombardment generates not only the characteristic spectrum, but also a continuous spectrum (background radiation) due to the interaction between the primary electrons and the nuclei of the atoms, it is necessary to make use of appropriate detection systems (spectrometer EDX-Energy Dispersive X-ray spectroscopy) that allow to analyse and separate the different energies of the radiations, to be able to make a measurement, from which it will be possible to obtain the composition of the sample. The schematic representation of the instrumentation of a SEM-EDXS is reported (Fig. 3.12):

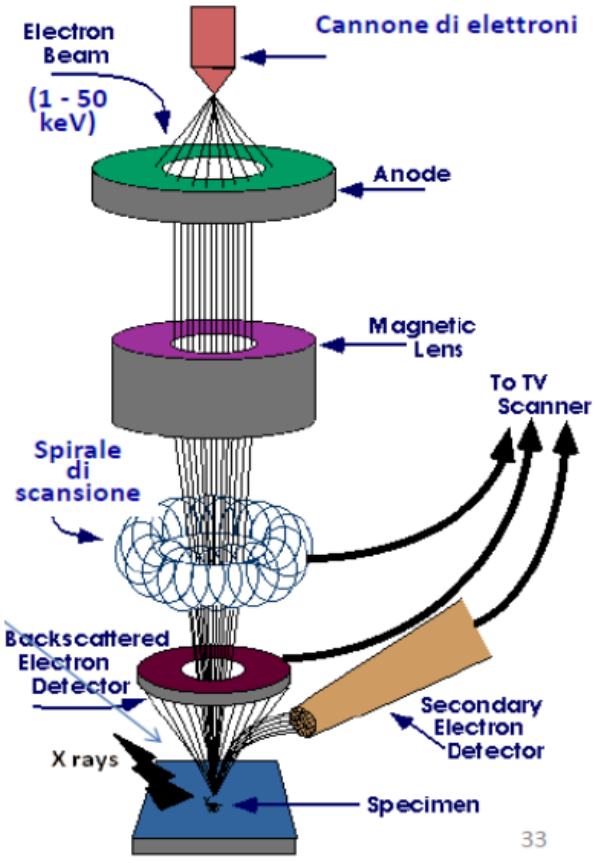

Figure 3.12: Schematic representation of a SEM-EDXS

3.6 XPS (x-ray photoelectron spectroscopy)

XPS (photoelectric X-ray spectroscopy) is a non-destructive technique used to determine the surfaces of materials. In this technique the sample is irradiated with an X-ray source and the photoemitted electrons are analysed. If ultraviolet radiation is used, this technique is called UPS (ultraviolet photo-emission spectroscopy). The UPS technique allows to excite electrons of the most external valence band, while in XPS electrons of the internal levels are also excited. X-ray photoelectron spectroscopy is based on the photoelectric effect: a radiation in the X field ($10\text{-}12 < \lambda < 10^{-8}$ m) hits a solid surface [219] causing the emission of electrons to the outside (photoelectrons).

In its simplest configuration an XPS spectrometer consists of a primary radiation source "X-ray source", a sample holder "UHV chamber" and an "electron energy analyser" (Fig. 3.13). The primary radiation is usually produced by interaction between electrons that are emitted by a cathode and are accelerated towards an anode in Mg or Al. In order to avoid any possible interference to the analysis, these instruments operate in the field of ultra-high vacuum (UHV) [220].

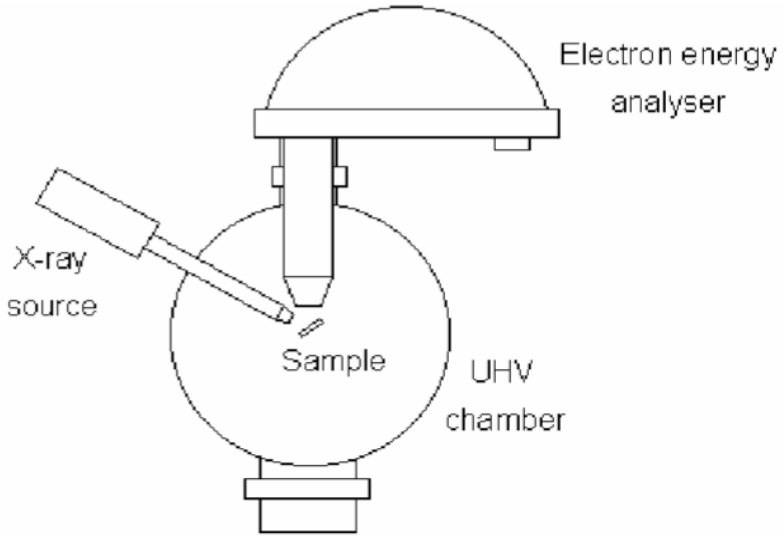

Figure 3.13: Schematic representation of an XPS spectrometer

The X-rays produced by the source affect the sample generating photoelectrons, i.e. electrons coming from the inner shells of the atoms, but also from those of valence (Fig. 3.14).

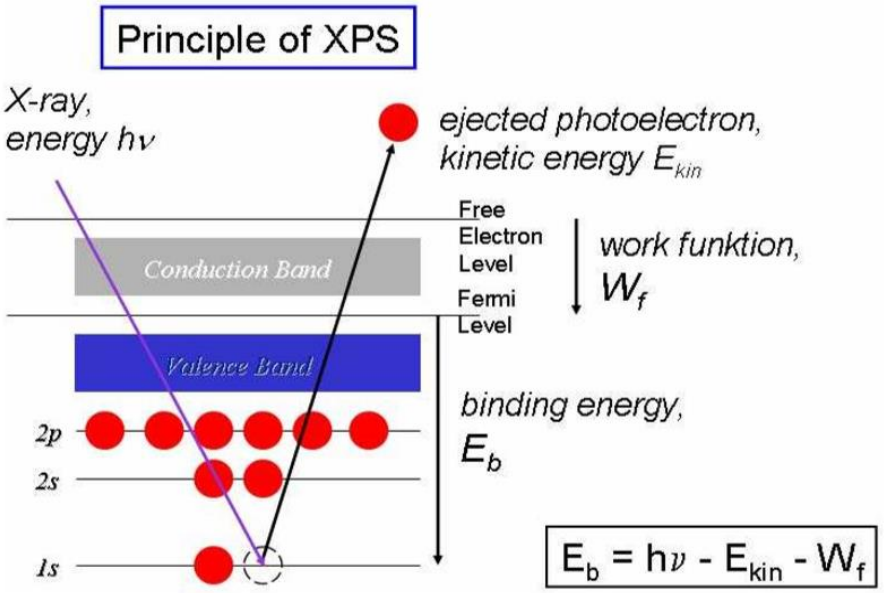

Figure 3.14 The photoemission process: the incident photon expels an electron from the shell 1s

The analyser allows to differentiate the kinetic energy associated to these electrons, providing as output a spectrum that reports the signal intensity (number of electrons counted per second) vs the kinetic energy possessed by the electrons themselves. This energy depends on the energy of the incident photons (primary radiation, E=hν) and on the binding energy of the electrons to the atom (Binding Energy, BE). It is possible to relate these quantities through the formula (3.12):

$$BE = h\nu - Ek - \Phi \qquad (3.12)$$

Where BE is binding energy of the electron and Φ is the function of the sample work ("Wf" in Fig. 3.14). Φ is defined as the minimum energy required to extract an electron from the material in a vacuum state. The most important information for photoelectron spectroscopy is relative BE, which depends on the chemical element from which the photoelectron is extracted, and also contains information on the chemical configuration in which the atom from which the photoelectron originates is located. Since during an XPS experiment all the quantities of the right member are known, it is possible to trace the binding energy of the electron "BE". Using an XPS spectrum (Fig. 3.15) it is therefore possible to obtain the electronic structure of a solid, from the valence band to the innermost electrons [220].

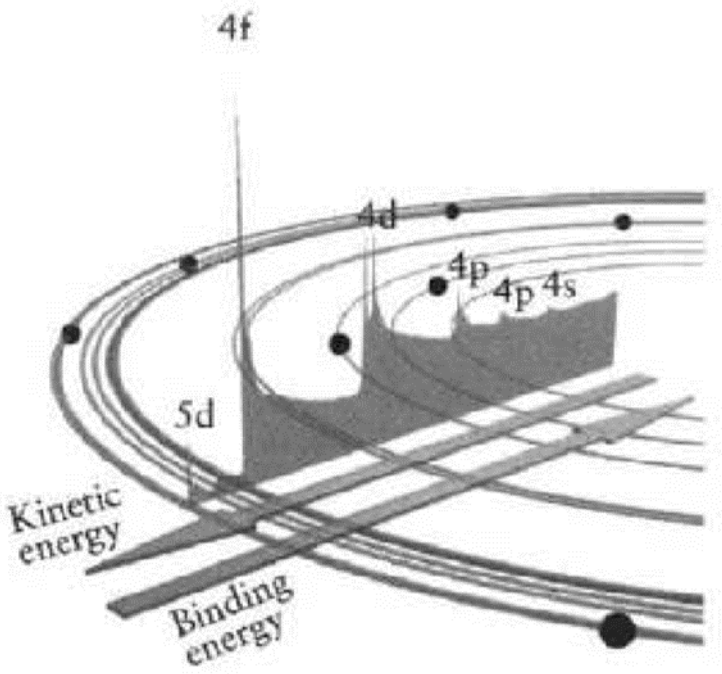

Figure 3.15: Example of XPS spectrum.

The electrons, following the interaction of the solid with the photons X, can follow three different ways: 1-Electric absorbs the photon and passes to an excited state. 2-The electron, once ejected moves towards the surface of the sample, 3- The electron is ejected into the vacuum, elastic collision. During the path of the electron towards the surface most of the generated electrons undergo inelastic collisions, which determine a reduction of the kinetic energy. Therefore, the photoemission spectra are made up of two main components:

The primary electrons that do not undergo inelastic collisions, determine distinct peaks that, in the first approximation, reflect the density of states of the sample.

Secondary electrons that, because of the interactions with matter, have lost kinetic energy. They determine a more or less continuous spectrum in energy up to zero kinetic energy.

These two types of electrons give us information of different types: the primary peaks allow us to determine binding energy (BE) of the electronic states of the sample, while the secondary electrons are mainly used to determine the function of the sample work. BE is sensitively influenced by the oxidation state of the element: at high oxidation states it will be more difficult to extract an electron and this results in an increase in BE [221].

3.7 Laser Microscopy

The laser microscope allows to obtain high-resolution optical images with depth selectivity. This technique has been used for the morphological characterization of samples. One other ability of the laser microscope is to allows to acquire focused images from selected points and depths. For operating principle see 3.2.3; 3D laser microscope and profile measurements, Keyence, VK-x200 series, Osaka, Japan. This instrument has a very high resolution and high magnification (24000X according to the manufacturer). The confocal configuration has two pinholes and only a small fraction of the sample volume around the focus point will be probed (described above). Laser microscopy enables scanning in the xy plane and along the z axis, allowing a 3D profile of the surface. Using 3D imaging it is possible to get information about the surface roughness, avoiding damage to the sample.

3.8 Experimental procedure

3.8.1 Cellular Treatment: Osteosarcoma SAOS-2

The samples of silicon nitride (positive control), Coating SN and ZR were analysed after incubation for 10 days at 37°C. The cells were initially incubated and cultured in an osteoblast-inducer medium consisting of 4.5g/L of glucose DMEM (D-glucose, L-glutamine, phenol red, and sodium pyruvate supplemented with 10% fetal bovine serum). They were allowed to proliferate within Petri dishes for 24h at 37◦C. The final SaOS-2 concentration was equal to 5×10^5 cell/ml. The cultured cells were placed in 24-well plate above the samples after UV light sterilization. The medium was changed every two days.

3.8.2 Bacteria protocol: Staphylococcus epidermidis

The samples of silicon nitride (positive control), Coating SN and ZR were analysed after incubation under aerobic conditions of 12; 24; 48h at 37°C. Bacteria protocol Gram-positive Staphylococcus epidermidis were cultured at the "Kyoto Prefectural University of Medicine"

in a brain heart infusion (BHI) agar culture medium. The initial concentration was subsequently diluted to 1×10^8 CFU mL^{-1} using a phosphate buffered saline solution (PBS) to mimic ion blood concentrations. Subsequently, 100 µL aliquots of the bacteria solution were transferred to Petri dishes containing the BHI agar and samples.

3.8.3 WST essay

After exposures of 12 and 48 hours of bacteria on surfaces samples (silicon nitride, Coating SN and ZR), the bacterial metabolism was examined with a colorimetric test (Microbial Viability Assay Kit-WST, Dojindo, Kumamoto, Japan). This test used WST-8 which is an indicator. WST-8 produces a water-soluble formazan dye after reduction in the presence of an electronic mediator. The amount of dye (formazan) generated is directly proportional to the number of living microorganisms. Using micro-plate readers (EMax, Molecular Devices, Sunnyvale, California) through an optical density (OD) method for living cells, bacterial solutions were analysed.

3.8.4 Raman Spectroscopy

The elemental chemistry of the surfaces of the samples of silicon nitride (positive control), Coating SN and ZR; and the increase of hydorssiapatite (HA) on the surface of the samples were studied by Raman. Raman spectra were collected by T-64000 equipped with a CCD detector (see 3.2.3) at room temperature. The obtained spectra were analysed with software (LabSpec, Horiba/Jobin-Yvon, Kyoto, Japan). A diode-pumped 532 nm Nd:YVO4 solid state laser excitation source (SOC JUNO, Showa Optronics Co. Ltd., Tokyo, Japan) operating with a nominal power of 200 mW and a confocal pinhole with an aperture diameter of 100 µm was used. The lateral resolution of the Raman micro probe was in the order of 1 µm. Spectral maps at certain depths, above or below the sample surface and spectral maps with high lateral resolution were recorded on the sample surface. An automated two-axis sampling stage was used for the recording. For each sample, 25 randomised positions were studied and the resulting spectra were averaged.

3.8.5 Fourier Transform Infrared Spectroscopy

The elemental chemistry of the surfaces of the samples of silicon nitride (positive control), Coating SN were studied by Fourier Transform Infrared Spectroscopy (FT-IR). FT-IR uses the Spotlight 200 imaging system (Perkin Elmer, Waltham, Massachusetts, USA) equipped with a total attenuated reflectance (ATR) imaging attachment. The FT-IR spectra obtained were acquired with an aperture of 200 × 200 μm2.

3.8.6 Fluorescence Microscope

Silicon nitride (positive control), Coating SN and ZR samples were studied under a fluorescence microscope (BZ-X700; Keyence, Osaka, Japan).

Bacterial samples were first observed. To facilitate their examination, the bacteria were stained with different solutions: 4',6-diamidine-2-phenylindol (DAPI; Dojindo, Kumamoto, Japan), 5(6)-carboxyfluorescein diacetate (CFDA; Dojindo, Kumamoto, Japan) and propidium iodide (PI; Dojindo, Kumamoto, Japan); these markers have already been described in chapter 3.4.3. DAPI, which binds to DNA, verified the positions and quantities of cell nuclei; the green colour of CFDA revealed live bacteria; the red colour of PI revealed dead or injured bacteria. The staining protocol consisted of adding 1 μL of DAPI, the PI solution, and 15 μL of CFDA solution to the samples. Then incubate for 5 minutes at 37°C. The buffer is then removed and the stained cells are analysed under a fluorescence microscope for 5s under a metal halide lamp (80 W). Later, exposure to osteoblasts was studied. The surfaces of the samples were treated with various immunostaining reagents prior to testing, including IgG isotype, polyclonal rabbit antibody (IBL, Gunma, Japan), human anti-osteocalcin clone 2H9F11F8 and Hoechst 33342 (Dojindo, Kumamoto, Japan). Hoechst 33342 is a staining of the cell nucleus; and has been used to visualize cell proliferation. The other two antibodies were used to stain proteins of the osteocalcin and osteopontin matrix, respectively, whose concentration quantifies the process of mineralization and bone matrix formation. Subsequently, a secondary antibody, Goat anti-Mouse IgG1 Conjugate FITC Antibody (Bethly Laboratories), was added to improve signal detection and visualization.

3.8.7 SEM

The elemental chemistry of the surfaces of the sample of Coating SN was studied by Scanning Electron Microscope (SEM). A field-emission-gun scanning electron microscope (JSM 7001F Scanning Electron Microscope, JEOL, Tokyo, Japan) was used. The surface of the samples was observed and characterized, before and after cell culture, and all images were collected at an acceleration voltage of 10 kV and magnifications between 100x and 50,000x. To improve their electrical conductivity, all samples were coated with sputter (Cressington, Watford, UK) with a thin layer of platinum (20 to 30 Å).

3.8.8 X-Ray Photoelectron Spectroscopy

The elemental chemistry of the surfaces of the sample Coating SN was studied by X-ray photoelectron spectroscopy (XPS). The measurements to obtain the XPS spectra used a device (JPS-9010MC/SP; JEOL, Tokyo, Japan). The device is equipped with a 10 kV (10 mA) Mg-Kα radiation source at the anode and both wide scan and narrow scan modes were applied with voltage steps of 1.0 and 0.1 eV, respectively. The measuring angle was 34° and the dwell time was always 100 ms. Emissions were recorded from zirconium atoms (Zr3d) to 184.5 and 187 eV, from oxygen atoms (O1s) to 533.5 eV, from silicon atoms (Si2p region) to 100, 102.5 and 104 eV and from nitrogen atoms (N1s) to 398 and 400 eV e. XPS measurements were repeated n=9 and scanned 40 times for each sample tested.

3.8.9 Laser Microscopy

The micrographs of the samples of silicon nitride (positive control), Coating SN and ZR were studied by Laser Microscopy. It was used with a 3D laser scanning microscope (VKX200K series, Keyence, Osaka, Japan) with magnifications ranging from 10x to 150x and a numerical aperture between 0.30 and 0.95. Through an automated x-y stage and an autofocus function for the z range, the acquisition of composite images has been allowed.

Chapter 4

Result

4. Substrates characterization

The substrates of the samples were characterized with the techniques of:

4.1.1 Laser microscopy

4.1.2 Fourier Transform Infrared Spectroscopy

4.1.3 Raman spectroscopy

4.1.4 X-Ray Photoelectron Spectroscopy

4.1.5 Scanning electron microscopy

4.1.6 Cross-sectional analysis

4.1.1 Laser microscopy

The surface morphology of silicon nitride and zirconia coating samples were characterized by Microscopy laser. Figure 4.0 shows the morphology of the polished zirconia samples (ZR) in Figure 4.0a compared to rough zirconia (ZR rough) in Figure 4.0b. Figure 4.0c and 4.0d. show the Si_3N_4 coating on polished zirconia and rough zirconia. It can be seen that the laser coating process produced a rough surface. In fact, the Si_3N_4 powder particles have different roughness orders. In Fig. 4.0d, scratches resulting from the roughening process are still visible after the coating, apprehensively 50 µm.

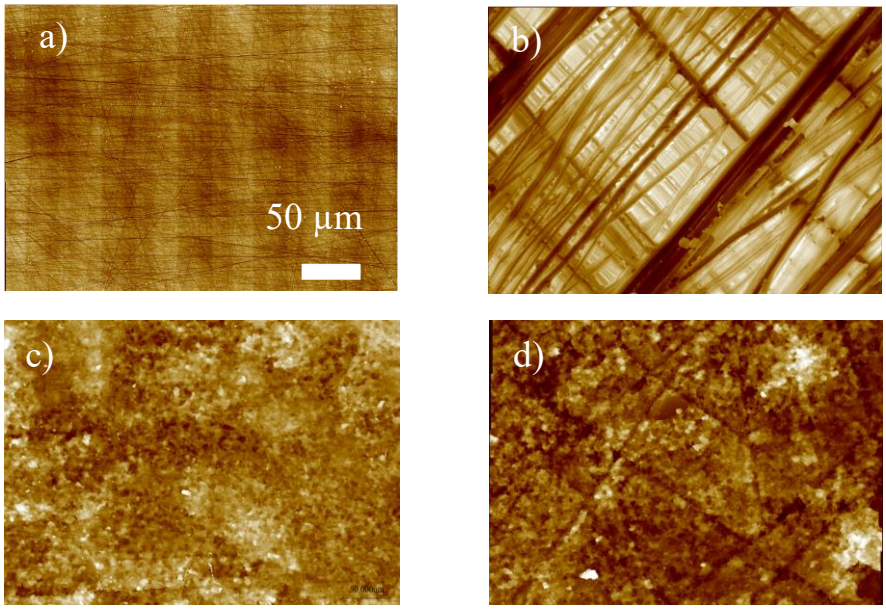

Figure 4.0: Laser Microscopy images a) polished zirconia; b) rough zirconia; c) polished zirconia coated with silicon nitride; d) rough zirconia coated with silicon nitride.

Analysing optical laser microscope images at higher magnifications, it was observed that white spots are present on the surface of the zirconia (rough and polished) coated with silicon nitride. These are due to a coating that is not perfectly homogeneous on the zirconia (Fig. 4.1a).
At lower magnifications, however, a network of cracks was clearly observed on the coated and polished zirconia samples (Fig. 4.1b). The cracks may be due to instability, causing compressive stress on the coating. It can be observed that the cracks did not result in high delamination of the coating, as only small portions of material were missing at the intersections of three or more ridge cracks (black arrow). Delamination is a process of breakage which consists of the separation of the foils in the vicinity of the free edges of the pieces, where high stress peaks are present. Residual compressive stresses occur during solidification. These are probably caused by the gap in the coefficient of thermal expansion for the various phases: amorphous (1.0 10-6 K-1 [222]) and nanocrystalline silicon (3.5 10-6 K-1 [222]), silicon nitride (1.0 10-6 K-1 [223]) and zirconia (11.0 10-6 K-1 [224]). It is noted that the main coating phase (amorphous silicon) and the substrate (zirconia) have a different coefficient of thermal expansion. And this causes a contraction of the coating on the zirconia that approaches its mechanical limits, thus forming folds and cracks. The presence of scratches on the zirconia has made it possible to reduce the stress concentration and improve the adhesion of the coating, prevents the formation of cracks.

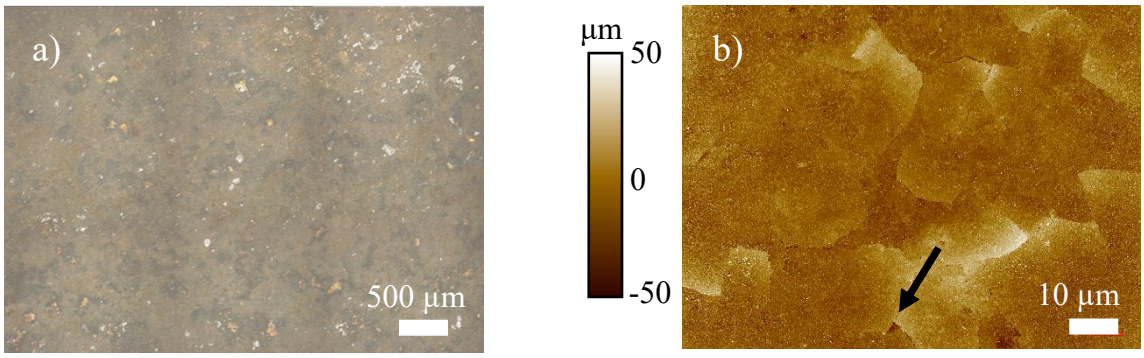

Figure 4.1: Laser Microscopy images a) The Optical image zirconia coated with silicon nitride; b) polished zirconia coated with silicon nitride.

The roughness of the samples has been studied through the use of laser microscopes that have allowed their analysis. Figure 4.2 shows the morphology of the samples. Specifically, an increase in roughness can be seen from polished zirconia to rough zirconia and coated zirconia with silicon nitride. The analysis between polished zirconia coated with silicon nitride and rough zirconia coated with silicon nitride has not been inserted because the roughness is the same.

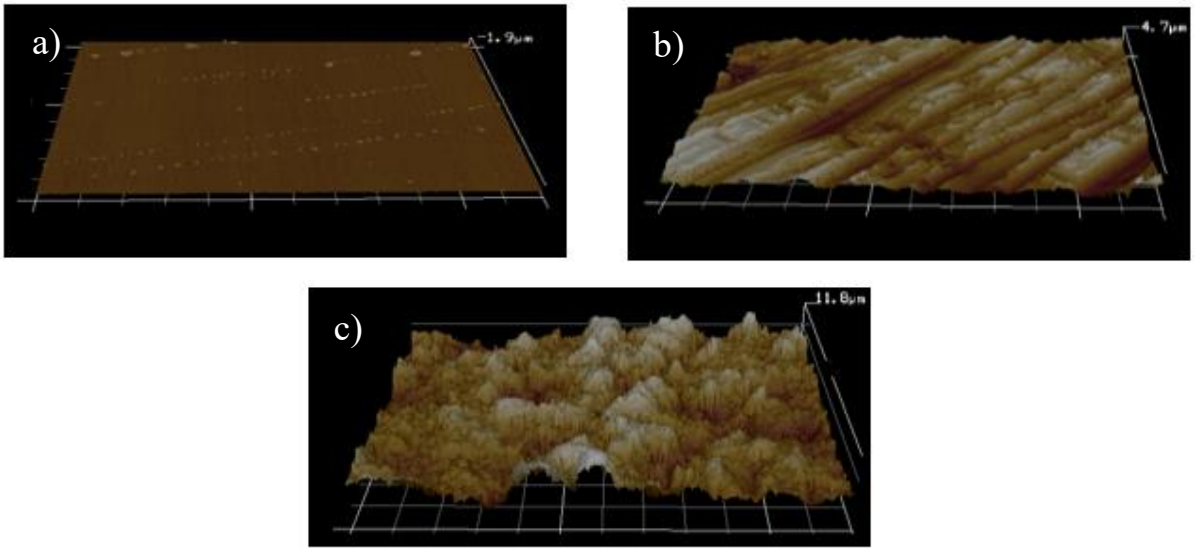

Figure 4.2: Laser Microscopy morphologic images; a) polished zirconia; b) rough zirconia; c) zirconia coated with silicon nitride.

Figure 4.3 shows the surface roughness values Ra (average rough) and Rz (maximum and minimum height difference) measured on the different samples at 50x magnification. Stoichiometric silicon nitride (SN) was used as positive control for the analysis. It is observed that the roughness, Ra and Rz, increases from ZR, SN, ZR rough to silicon nitride coated. There is no roughness comparison between polished and rough zirconia coating because it is the same.

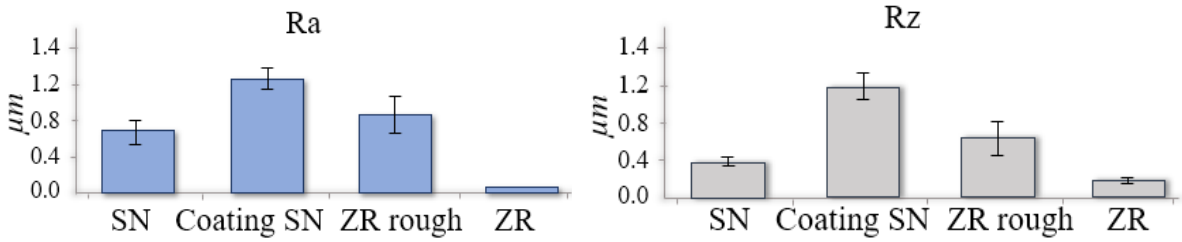

Figure 4.3 The surface roughness values measured on the different samples are represented, with a magnification of 50x. Ra corresponds to average rough; Rz corresponds to the difference between maximum and minimum height (Qmax - Qmin).

4.1.2 Fourier Transform Infrared Spectroscopy

Zirconia coated with silicon nitride (CoatingSN) and stoichiometric silicon nitride (SN) were characterized by FT-IR spectroscopy. The FT-IT characterization identifies a first analysis for the identification of the surface chemistry of Coating SN against SN (positive sample).

The spectrum of silicon nitride is divided into regions for better understanding [225] [226] [227] [228]:

- 400-600cm^{-1} has the bending of Si-N; Si-O
- 600-800cm^{-1} both has bending O-Si-O; N-Si-O.
- 800-1000cm^{-1} has Si-N silicon nitride stretching
- 1000-1200cm^{-1} are present the stretching O-Si-O; N-Si-O.

It is observed that before 800 cm^{-1} the energy is low for stretching vibration. From 800cm^{-1} the energy is increased and It can be obtained the stretching vibration of Si_3N_4.

In Figure 4.4 it can be examined the comparison between the spectrum of SN and Coating SN and it is noted that Coating SN shows a different behaviour from SN. In particular, in the region between 400-600cm^{-1} a broadband is observed probably due to an increase of oxygen and a decrease of nitrogen in the crystalline lattice (peaks 1;2). In the region between 600-800cm^{-1} a shoulder formation is observed, possibly due to an increase in oxygen (peaks 3;4). In the region between 800-1000cm^{-1} a shift in the band at lower energies and broadband is emerged, probably due to a loss of crystallinity of silicon nitride (peaks 5;6;7;8). Most of Si_3N_4 is in an amorphous state. In the region between 1000-1080cm^{-1} a shift of the lower-energy and broadband band is emerged, probably still due to an amorphous silicon nitride structure (peaks 9;10). This

characterization shows that silicon nitride shifts from a crystalline Si_3N_4 structure to an amorphous Si(3+x)N(4-y) with an increase in oxygen and loss of nitrogen.

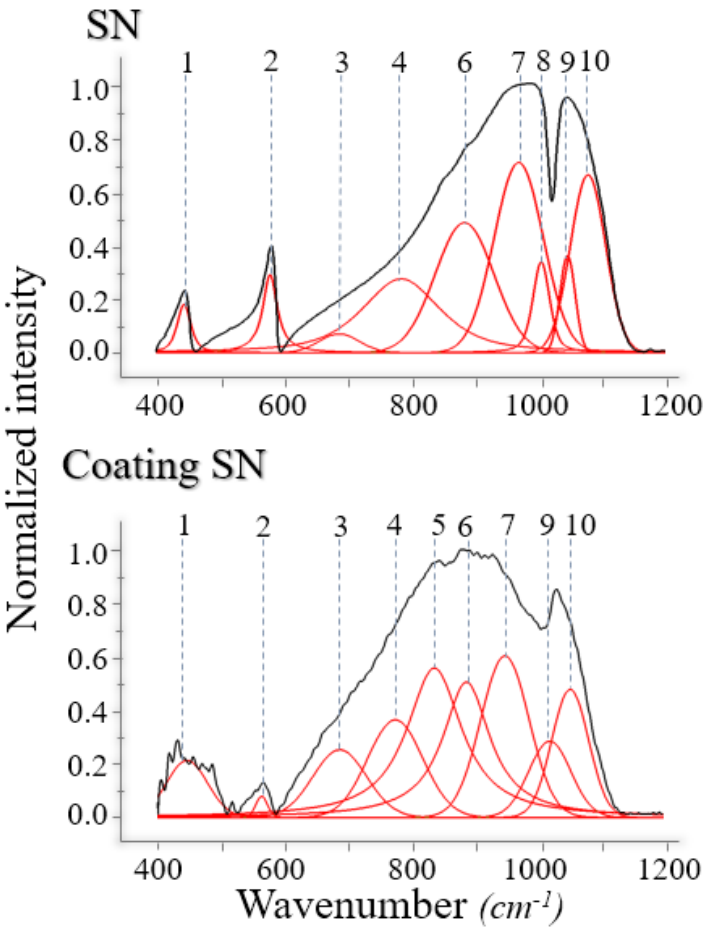

Figure 4.4: FT-IT spectra of zirconia coated with silicon nitride (coatingSN) and silicon nitride powder (SN).

4.1.3 Raman Spectroscopy

Zirconia coated with silicon nitride(CoatingSN) and stoichiometric silicon nitride (SN), rough zirconia (ZR rough) and polished zirconia (ZR) samples, were characterized by Raman. Raman analysis was done to further investigate the morphology of the various samples. It also defines a finger print [195] [196]. Fig.4.5 and Fig. 4.6 shows the spectra ZR and ZR rough, while Fig.4 shows the SN compared to the Coating SN. The zirconia substrates (Fig. 4.5) are in tetragonal crystalline shape (t-ZR), and the Raman peaks of polished zirconia have its characteristic peaks. In particular, the t-ZR peaks have a Raman shift of: 147, 260, 324, 368, 607 and 643cm^{-1} [229] [230] [231] [232] [233]. Polished substrates are made of 100% tetragonal zirconia. Rough

zirconia has two small peaks relative to monoclinic zirconia (m-ZR) at approximately 180 and 192cm^{-1} [233] [231] [229]. The tetragonal-monocline crystalline transformation arises from the roughening process, which has generated internal stresses in the crystalline lattice. The crystalline lattice has undergone a stress-induced transformation because the monocline form is the most stable at room temperature. During the preparation of the sample, scratching the surface of the t-ZR resulted in the tenaciousness mechanism [134] [136] [135]. The mean value of m-ZR over the entire surface of the zirconia rough was 0.55 ±0.22 %.

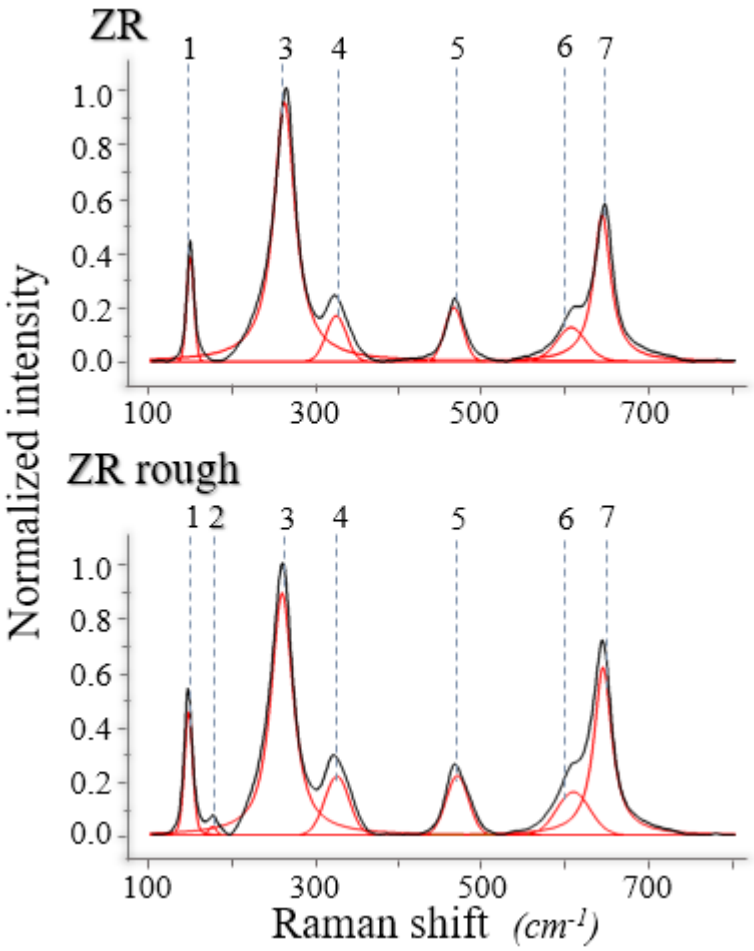

Figure 4.5: Raman spectra of polished zirconia (ZR) and rough zirconia (ZR rough).

Figure 4.6 compares the spectra of silicon nitride (SN) and silicon nitride coating (CoatingSN). The silicon nitride stoichiometric is β-Si_3N_4 stoichiometric, in fact in the SN spectrum the characteristic peaks of the Si-N bonds are visible; 181, 202, 225cm^{-1} [234] [235] [236] [237] [238]. The silicon nitride stoichiometric is 100% β-Si_3N_4. The silicon nitride coating has only a peak at 517cm^{-1} which is associated with Si-Si vibrations [236].

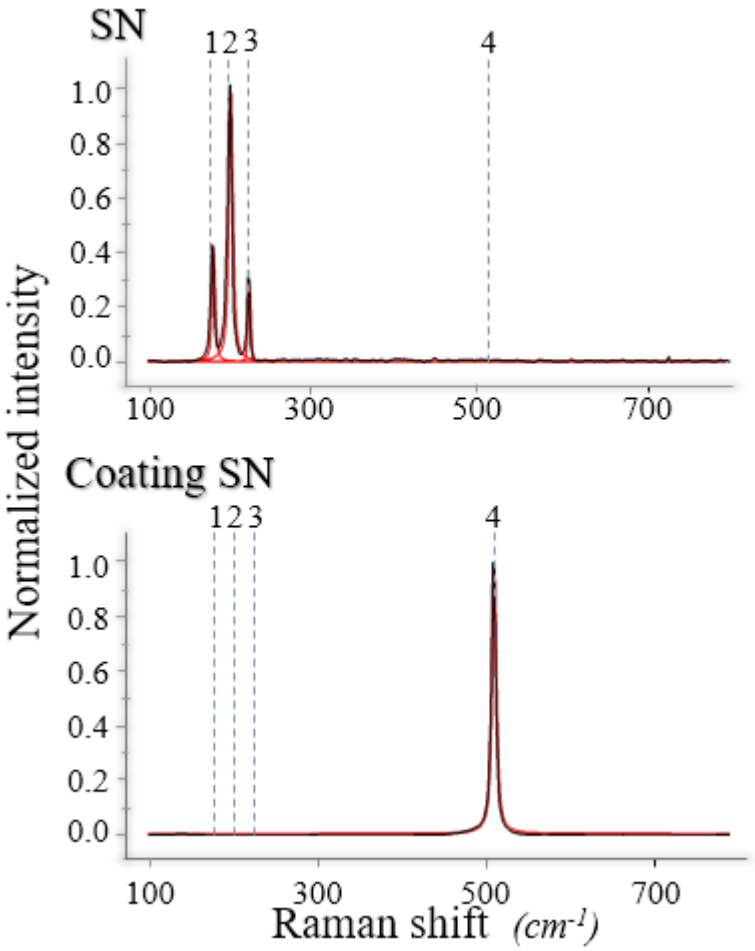

Figure 4.6: Raman spectra of zirconia coated with silicon nitride (CoatingSN) and silicon nitride powder (SN).

4.1.4 X-Ray Photoelectron Spectroscopy

The X-Ray Photoelectron Spectroscopy (XPS) characterization has been performed only on the zirconia coated with silicon nitride sample (CoatingSN) , in order to get a more detailed analysis of the surface chemistry. Figure 4.7 shows the XPS spectra of silicon, oxygen, nitrogen and zirconium. The silicon signal was deconvolved in three main bands: silicon metal (100 eV), silicon nitride (102.5 eV) and silicon oxide (104 eV) [239] [240]. It can be observed that the silicon element represents 34% of the total elements and only 9.5% corresponds to silicon nitride. The rest 24% is Si or SiO_2, this is confirmed because the silicon oxide is the strongest signal, and also because the spectrum at about 533.5 eV and related to oxygen bonds (1s) [241] [242]. The presence of silicon-nitrogen-oxygen bonds was also confirmed by the nitrogen

spectra (1s) at about 400 eV. Two main peaks can be observed: stoichiometric silicon nitride (400 eV) and Si_x-N-O_x phases, resulting from partial oxidation (398 eV) [243]. Finally, all zirconium ions detected by XPS (185-187 eV) [244] seemed to be oxygen bound, which means that the only possible source for such a signal was the exposed residual substrate.

The presence of SiO_2 in high concentration is presumably due to the reaction between water (moisture atmosphere) and silicon (Si-Si), which produces a thin, uniform layer of passivation on the silicon particles. The passivated layer corresponds to the oxidation of silicon SiO_2. The reaction rate increases as the average diameter of the particles becomes smaller [245]. On the zirconia sample coated with silicon nitride there was a passivated layer during deposition, caused by possible initial oxygen sources. The oxygen present was limited to the gas trapped in the dust or chemically bound to silicon nitride in the form of silicon oxide or silicon oxinitride. It is supposed that the zirconia sample coated with silicon nitride has trans-micrometric and sub-micrometric particles and the passivation reaction can be considered instantaneous.

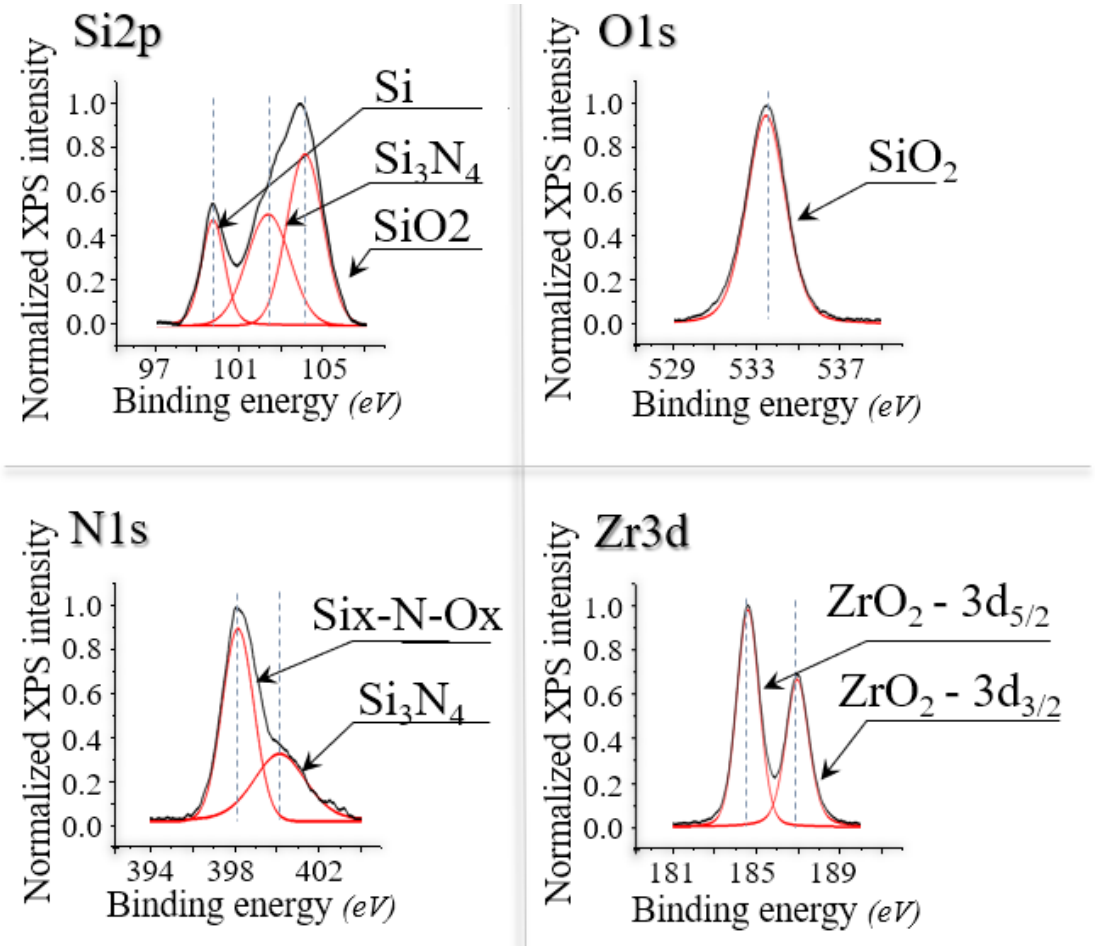

Figure 4.7: Surface composition of the zirconia coated with silicon nitride sample obtained in the Si2p, O1s, N1s and Zr3d regions.

4.1.5 Scanning Electron Spectroscopy

Zirconia coated with silicon nitride (CoatingSN) and rough zirconia (ZR rough) samples were characterized through the SEM technique, at different magnifications (Fig.4.8). In Figure 3.8a the scratches have two main orientations and are almost perpendicular to each other (≅90°). This was chosen as the best condition to obtain a uniform adhesion of the laser-coated coating and avoid preferential orientations. At higher magnifications (Fig. 4.8b), it can be observed that the roughening process has led to the formation of small debris, the amount of which can be roughly related to the depth of the relative abrasion.

The low magnification analysis of Coating SN (Fig. 4.8c) showed generally good coverage of the substrate, with only localized defects that appear to be small cracks or intergranular voids. In addition, there are spots due to non-coating of the surface. At higher magnifications (Fig. 4.8d), the coating revealed its composite structure with a dispersion of sub-micrometric globular particles protruding from the continuous matrix in which they are embedded. EDX analysis was carried out on the sample of zirconia coated with silicon nitride and it was found that out of a total of 56% Silicon, only 28% was silicon nitride. The rest 28% is Si or SiO_2. This demonstrates the considerable amount of passivated layer on the surface of the particles. This layer was generated during sample production due to the reaction between humid air and silicon.

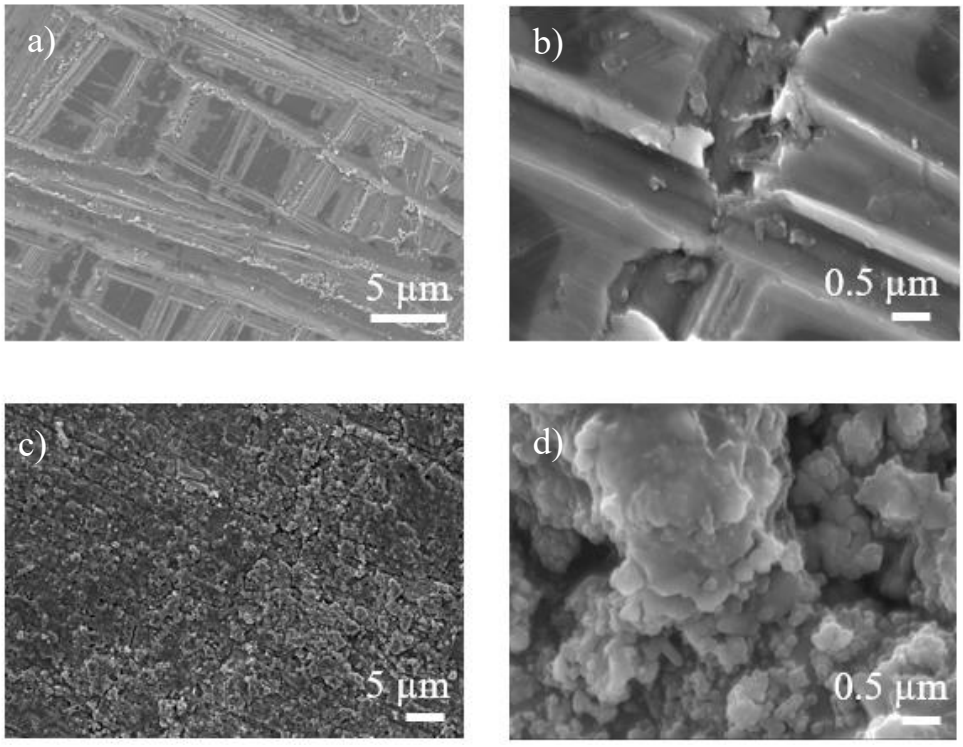

Figure 4.8: SEM of the roughened zirconia samples before(a,b) and after (c,d) coating, at low (a,c) and high (b,d) magnifications.

4.1.6 Cross-sectional analysis

Zirconia coated with silicon nitride sample (CoatingSN) was characterized through cross-sectional analysis. This study defines an accurate analysis of the coating thickness. Specifically, the was first cut through a diamond tip and then analysed at SEM. The reason why the sample it has been cut is due to the view of the coating that, in this way, become more accurate (Fig. 4.9).

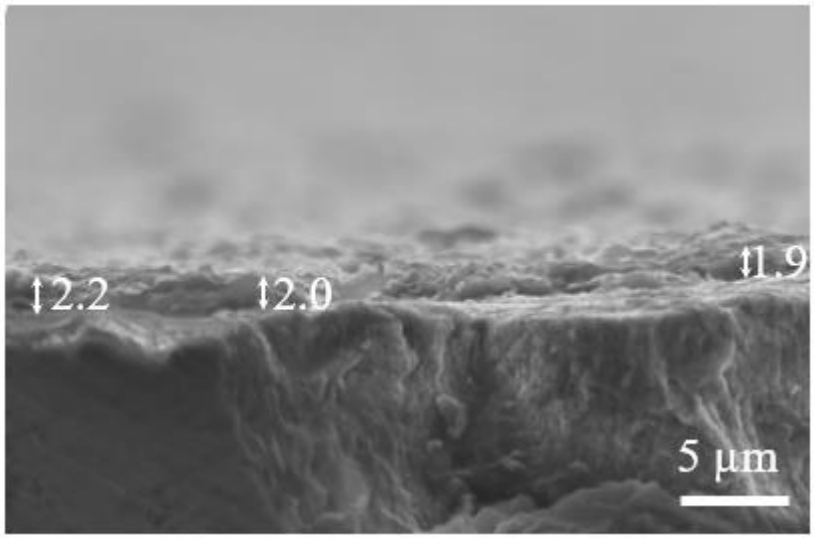

Figure 4.9: SEM image of a portion of the section of the zirconia sample coated with silicon nitride. Some examples of coating thickness measurements are shown.

Through SEM images (Fig. 4.9) shows a portion of the overall section the coating thickness was measured 98 times obtaining the average thickness µm= 2.18µm with a standard deviation of σ = 0.34µm. The thickness range, in first approximation is between µm-σ = 2.52µm and µm+σ = 1.84µm. A Gaussian distribution of thickness was then calculated (fig. 4.10) through the function (4.1).

The normal Gauss distribution is a continuous probability distribution function (4.1), which was used to calculate the thickness distribution function. The function describes the random measured coating thickness values that tend to concentrate around the mean value. The distribution in fact depends on the parameters µ and σ, respectively the mean value and standard deviation (4.1). Plotting then the function obtains the following trend (Fig.4.10)

$$f(x;\mu;\sigma) = \frac{1}{\sqrt{2}\pi\sigma} e^{-\left(\frac{(x-\mu)^2}{2\sigma^2}\right)} \quad (4.1)$$

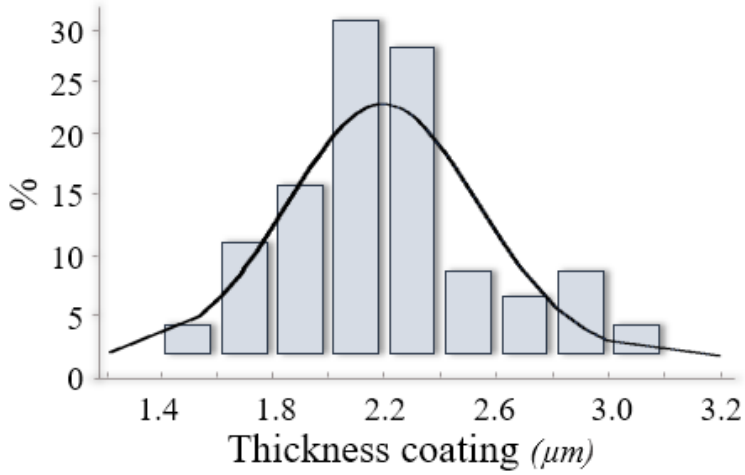

Figure 4.10: Gaussian distribution of thickness. The bar graph and the normal Gaussian function describing the coating thickness trend is shown.

The Gaussian distribution of thickness shows an almost uniform distribution of values. It is noted that the values between 2.0 - 2.4 μm are the most frequent, in fact the average is 2.18 μm.

4.2 Bacteria characterization: *Staphylococcus epidermidis*

After substrate characterization, the samples were treated with Staphylococcus epidermidis bacteria under aerobic conditions for 12; 24; 48 hours (see paragraph 3.8.2), then characterized with the techniques of:

4.2.1 Raman

4.2.2 Fluorescence microscope

4.2.3 WST

4.2.1 Raman Spectroscopy

Coated zirconia with silicon nitride (CoatingSN), rough zirconia (ZR rough) and polished zirconia (ZR) samples were characterized by Raman. Figure 4.11 shows the samples treated for 12, 24 and 48 hours with Staphylococcus epidermidis bacteria. The spectra have a region

between 2800 and 3100 cm-1 that corresponds to the vibration of the bacteria cell membrane. Due to the spectra that had too much background noise it was not possible to repeat the experiment analysing other Raman shift regions. The Table 4.0 shows the Raman vibrations.

	RAMAN SHIFT (cm^{-1})	ASSIGNEMENT	REFERENCE
1	2855	CH_2 stretch. Sy: (lipids; fatty acids)	[246]
1	2880	CH_3 stretch. Sy (lipids; fatty acids)	[247] [248]
3	2935	CH_2 CH_3 stretch. Sy, Asy: C-H (lipids; proteins; carbohydrates)	[249] [250] [248]
4	2970	CH_3 stretch. Sy: C-H (lipids; fatty acids)	[246] [248]
5	3060	C=C CH stretch. (olefinic)	[250]

Table 4.2: Peaks assignments Raman after 12, 24 and 48 hours with Staphylococcus epidermidis bacteria.

Figure 4.11 shows the Raman spectra. The normalized intensity is present in the ordinate, because what is analysed is whether the sample surfaces are colonized by bacteria. All surfaces have been colonized by the bacteria, as all spectra have the relative bands of the cell membrane. There are small differences between the different spectra. The spectra Coating SN at 12 hours

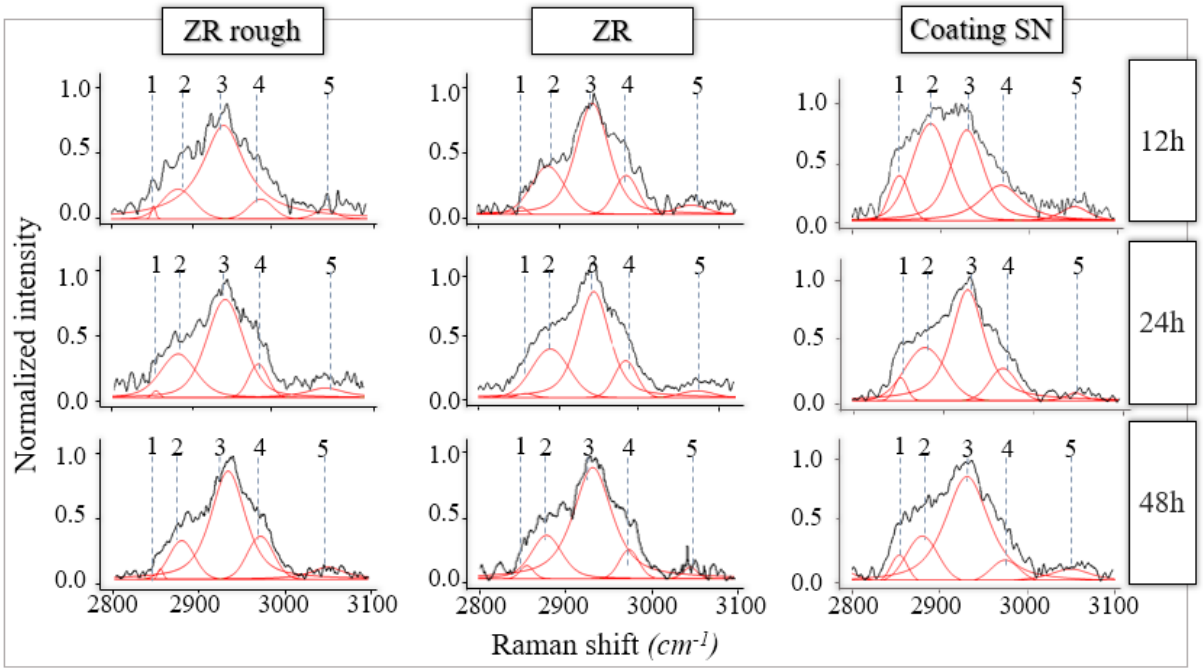

Figure 4.11: Raman spectra for the various samples after 12, 24 and 48 hours exposure to Staphylococcus epidermidis bacteria.

shows the most intense symmetrical CH_3 vibrational band, probably due to a higher amount of lipids and fatty acids.

4.2.2 Fluorescence microscope

Zirconia coated with silicon nitride (CoatingSN), stoichiometric silicon nitride (SN) rough zirconia (ZR rough) and polished zirconia (ZR) samples, were characterized by fluorescence microscopy. Figures 4.12, 4.13 and 4.14 show the samples treated for 12, 24, 48 hours with *Staphylococcus epidermidis* bacteria. Stoichiometric silicon nitride was used for comparison as a positive control. The FM images show three different colours which were the 3 markers used: DAPI (blue colour) represents the total cell nuclei; CFDA (green colour) the still living bacteria and PI (red colour) the dead bacteria.

Stoichiometric silicon nitride substrates have detected the highest amount of bacterial colonization and it has been observed that the trend in the number of living cells increases during the first 24 hours and then decreases after 48 hours of incubation. However, live cells are above the expected value and bacterial death is therefore low [251]. In Coating SN bacterial death is apparently high, but the number of live cells over the entire sample surface is high, indicating a significant bacterial proliferation for all times (12, 24, 48h). For zirconia samples at 12 and 24h a large biofilm concertation is observed, which prevents an accurate analysis. While at 48h it is noted that the sample of ZR rough, presents the main concentration of bacteria in the scratches with an apparently low bacterial death. ZR rough was theoretically the sample that worked worse, not being bioactive. In fact, it presents a surface morphology suitable for bacterial proliferation. The ZR sample also presents a large amount of biofilm at 48h that prevents the analysis.

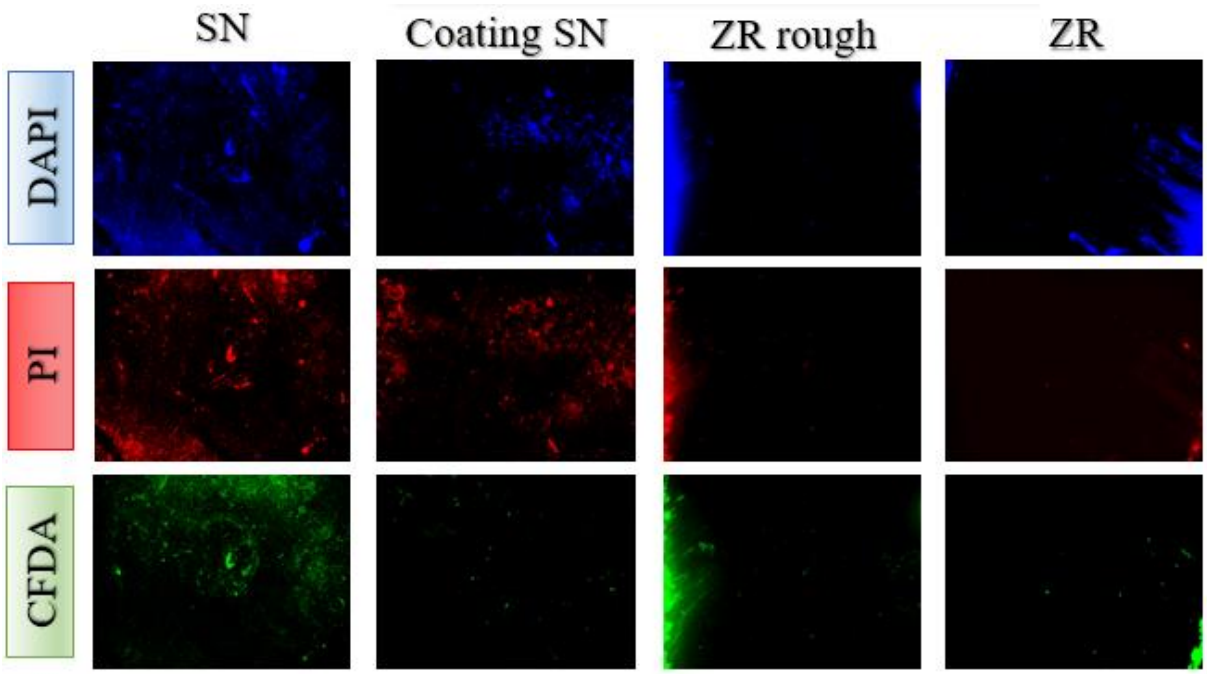

*Figure:4.12: Fluorescence micrograph after PI, CFDA, and DAPI staining of S. epidermidis exposed for **12h** to for the various samples. Live and dead cells were labeled with green and red stains, respectively, whereas nuclei displayed in blue colour.*

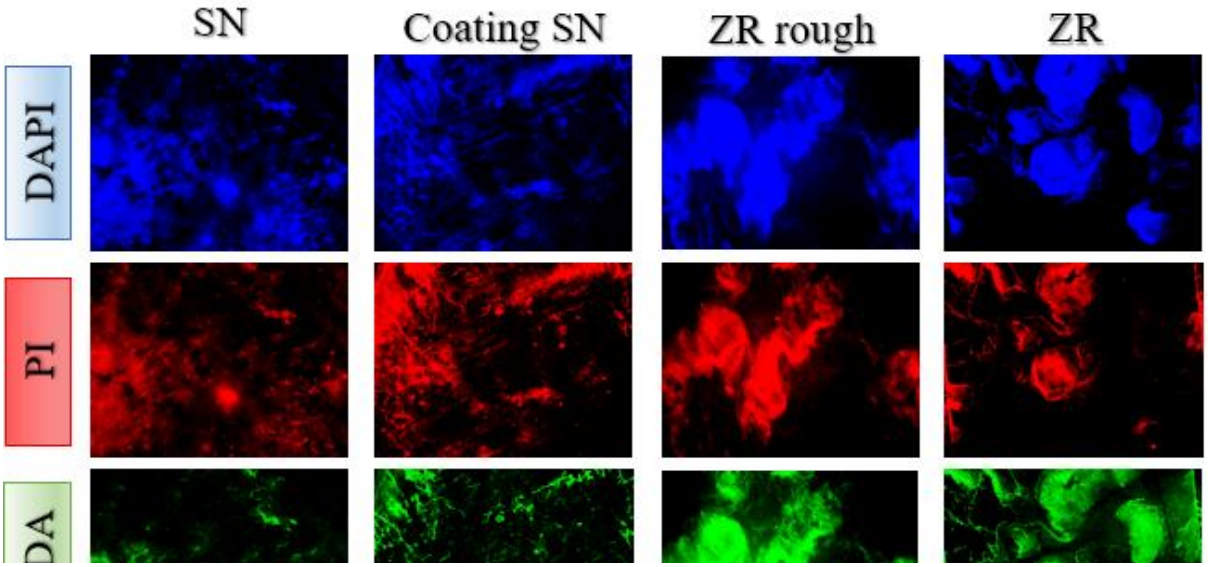

*Figure 4.13: Fluorescence micrograph after PI, CFDA, and DAPI staining of S. epidermidis exposed for **24h** for the various samples. Live and dead cells were labeled with green and red stains, respectively, whereas nuclei displayed in blue colour.*

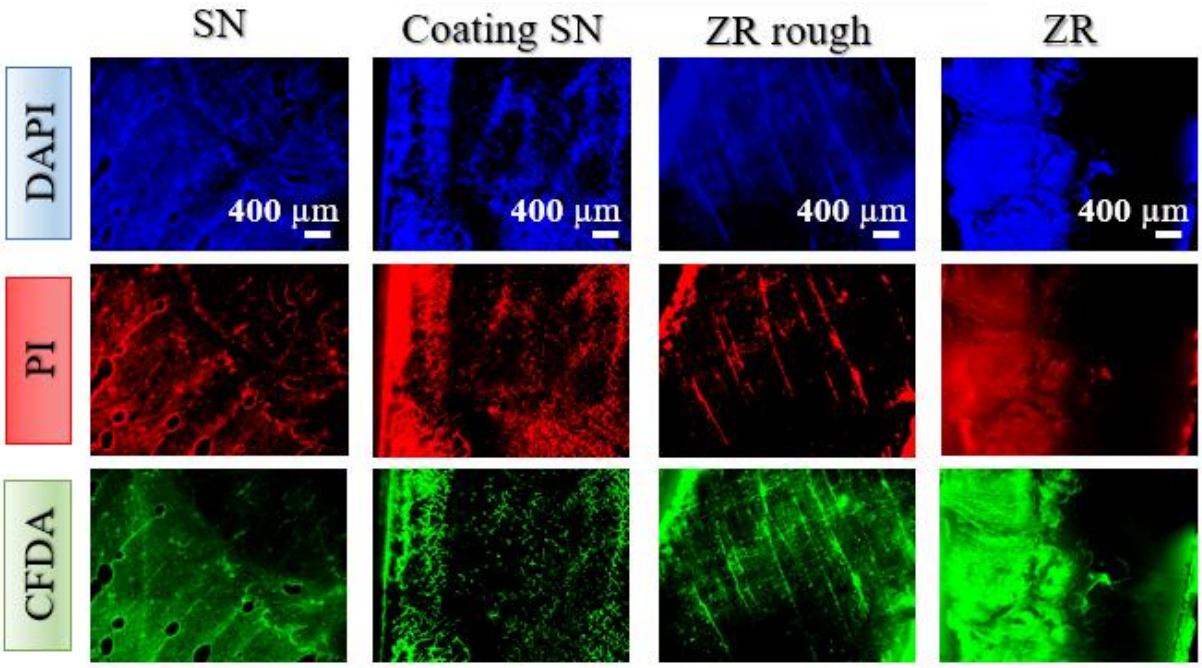

*Figure 4.14: Fluorescence micrograph after PI, CFDA, and DAPI staining of S. epidermidis exposed for **48h** for the various samples. Live and dead cells were labeled with green and red stains, respectively, whereas nuclei displayed in blue colour.*

4.2.3 WST

Zirconia coated with silicon nitride (CoatingSN), stoichiometric silicon nitride (SN) rough zirconia (ZR rough) and polished zirconia (ZR) samples were characterized through viability testing with a WST-8 test, after 12, 24 and 48 hours with Staphylococcus epidermidis bacteria. (see 3.8.3). The "OD currency" data obtained from the WST-8 test, were divided by the sample area to obtain a standard value. The reason of this division is given by the bacterial concentration on the sample surface that is different for each sample area. Bacterial culture does not allow the number of bacteria present on the surface to be quantified. And consequently the count of the pixel of bacterial FM images does not work. It can be seen in Figure 3.1 that for all samples, the amount of living bacteria decreases from 12 to 48 hours.

Moreover, in the figure are represented, in red, the lines showing the slope (m1 and m2) between 12-24, 24-48 hours. These slopes calculate the rate of bacterial death and are a parameter to analyse the antibacterial behaviour of the surface. The slope has been calculated (4.0):

$$m = \frac{\Delta\,(OD\ valute)}{\Delta t} \qquad (4.0)$$

Table 4.1 shows the slopes.

	$m1$ Δt1 (24h-12h)	$m2$ Δt2 (48h-24h)
SN	-4.39	-1.86
Coating SN	-0.84	-3.48
ZR rough	-6.55	-6.00
ZR	-3.33	-1.25

Table 4.1: Slope values representing the rate of bacterial death for the various samples.

It can be observed that SN shows an anomalous trend because the slope after 24 hours decreases (m2). This value obtained is below expectations and the theoretical value [38] [39]. For Coating SN there is an increase in the slope after 24 hours (m2), but the m1 value is the lowest of all the samples and the slope m2 is very low. The ZR rough sample has the highest slope, both at m1 and m2, i.e. the best bacterial death rate. This result is anomalous because a better bacterial death rate was expected for SN and Coating SN. The ZR rough sample in theory is the sample with the worst antibacterial properties [130].

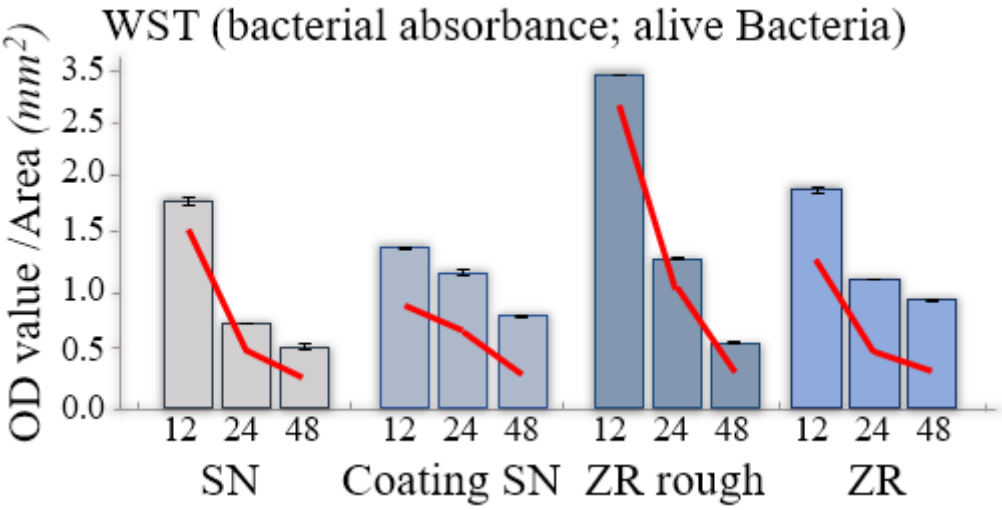

Figure 4.15: WST optical density results measured on different samples of S. epidermidis exposed for 12, 24 and 48hours. The "OD value" data has been divided with the sample area to obtain a standard value. The red lines showing rate of death bacterial (m1 and m2) between 12-24, 24-48 hours.

4.3 Cell characterization: SaOS-2

After substrate characterization, the samples were treated with SaOS-2 osteosarcoma for 10 days (see paragraph 2.8.1) and then characterized with the techniques of:

4.3.1 Fluorescence microscope

4.3.2 WST

4.3.3 Raman

4.3.4 Quality index

4.3.5 Scanning electron microscopy

4.3.1 Fluorescence microscopy

Zirconia coated with silicon nitride (CoatingSN), stoichiometric silicon nitride (SN) rough zirconia (ZR rough) and polished zirconia (ZR) samples were characterized by fluorescence microscopy (Fig.4.16). The samples were treated for 10 days with SaOS-2 osteosarcoma. Stoichiometric silicon nitride was used for comparison as a positive control. The results show that the cell proliferation on silicon nitride was much higher than on polished and rough zirconia, as expected. The roughened samples showed generally higher cell adhesion than smooth surfaces, but Coating SN was the only sample capable of showing a homogeneous distribution of cell nuclei over the entire surface. In addition, both osteocalcin and osteopontin levels were higher on Coating SN samples compared to both smooth and rough zirconia. Compared to stoichiometric silicon nitride, Coating SN samples showed less cell proliferation on the surface, but there appears to be more extracellular matrix released (osteocalcin and osteopontine).

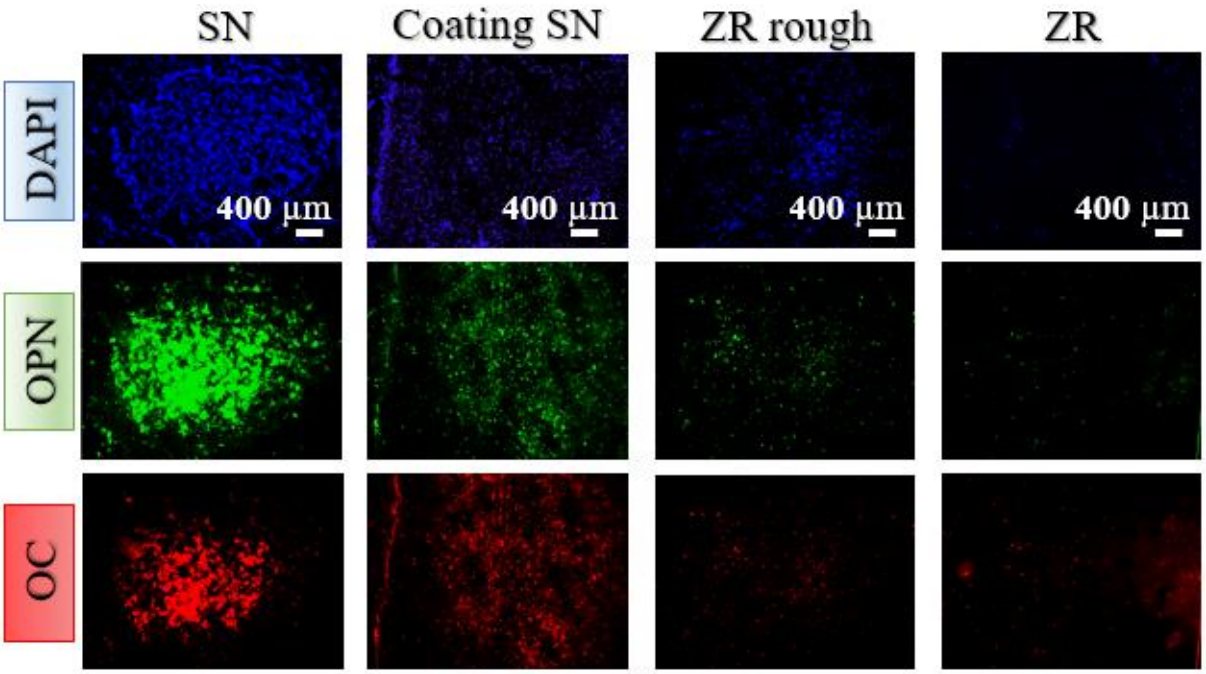

Figure 4.16: Fluorescence microscopy results as obtained on the various samples, showing the presence and distribution of cell nuclei (blue), osteocalcin (green) and osteopontin (red) on the surfaces.

In order to get a more accurate analysis, pixel counting was done on the fluorescence microscopy images. Pixels were counted for each image and the result data were averaged and reported in a graph (Fig. 4.17). It is noted that the SN sample has a higher cellular adhesion than all other samples (DAPI markers). Then, examining the sample of Coating SN, ZR rough and ZR, it is noted that the Coating SN sample shows an increase of osteopontine and osteocalcin compared to DAPI (see arrow). There was, therefore, a faster release of extracellular matrix than the SN sample suggesting a faster osseointegration. The quality of Hydroxyapatite and collagen released should be studied to assess bone quality.

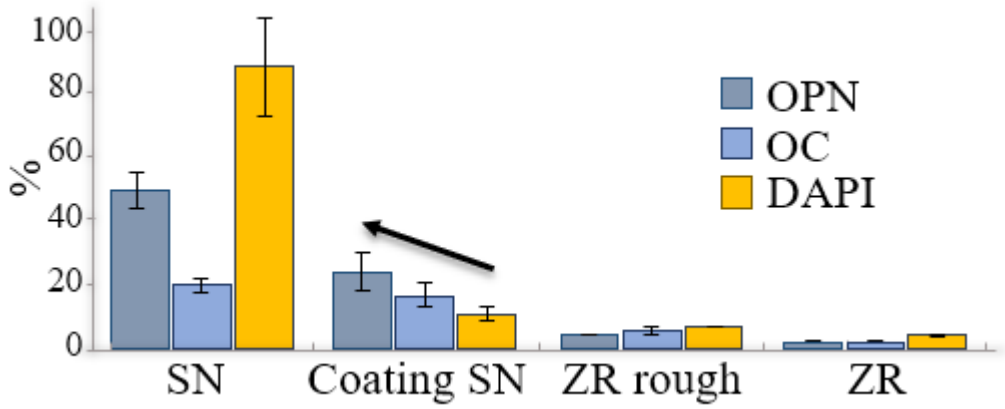

Figure 4.17: Number of pixels of fluorescence microscopy images, for the DAPI marker and osteopontine (OPN) and osteocalcin (OC) stains, on the four different samples.

4.3.2 WST

Zirconia coated with silicon nitride (CoatingSN), stoichiometric silicon nitride (SN) rough zirconia (ZR rough) and polished zirconia (ZR) samples were characterized through viability testing using a WST-8 test, after 10 days of exposure with SaOS-2 osteosarcoma (see 3.8.3). It is observed in Figure 4.18 that the amount of cells observed on zirconia samples are similar, with differences in statistical dispersion of optical density measurements. On the other hand, the optical density measured on the silicon nitride reference sample was significantly higher, this fact means that more cells are colonizing the surface. The result got is in line with fluorescence microscopy data and the bioactive properties of silicon nitride, and were previously correlated with the presence (and release) of nitrogen [252] [253] [254] [34]. The different cellular response of Coating SN compared to stoichiometric Si_3N_4 is caused by the passivation layer which decreases the amount of nitrogen available on the surface. This confirms that nitrogen is the key element responsible for improving observed cell proliferation [252] [35].

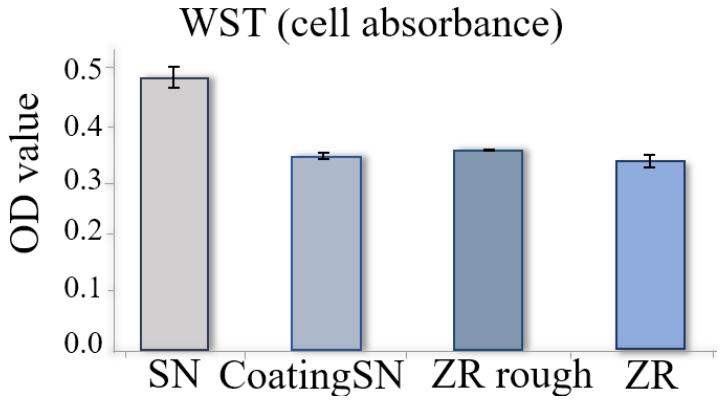

Figure 4.18: WST optical density results measured after 10 days on different samples.

4.3.3 Raman Spectroscopy

Zirconia coated with silicon nitride (CoatingSN), stoichiometric silicon nitride (SN) rough zirconia (ZR rough) and polished zirconia (ZR) samples were characterized by Raman after the SaOS-2 osteosarcoma test are shown in Figure 4.19 and Figure 4.21 with the related Raman shifts in Table 4.1. The spectrum has a region between 600 and 1800 cm^{-1}, which can be divided approximately into four areas, depending on the nature of the vibration. The first region, between 600 and 100cm^{-1}, is mainly dominated by the strong peak related to phosphate vibrations, at about 960cm^{-1}. The second region, between 1200 and 1400cm^{-1} is associated with

the vibrations of Amide III [255]. The low intensity bands in the region between 1400 and 1650 cm^{-1} are conventionally marked by fatty acids [256], while the strongest band at 1590cm^{-1} is associated with Amide II. Finally, the two relatively weak peaks at 1660 and 1690cm^{-1} are the result of the vibrations of Amide I.

When comparing the Raman spectrum of Coating SN to the SN spectrum, it is evident that there is an increase in the Amide I, II and III bands which is probably due to an increase in collagen in the bone structure (II,III,IV spectrum region). Collagen is released from osteoblasts through the extracellular matrix. This is consistent with the data found in microscope fluorescence where there is an increase in osteopontine and ostocalcine compared to nuclei. On the other hand, the SN spectrum presents the more pronounced vibrations of the phosphate group, which results in a more resistant and compact crystalline structure of bone [257]. Zirconia spectra, as in Coating SN, have more intense amine bands. In addition, for a more detailed analysis, the "quality indices" characteristic of some Raman bands of hydroxyapatite have been studied.

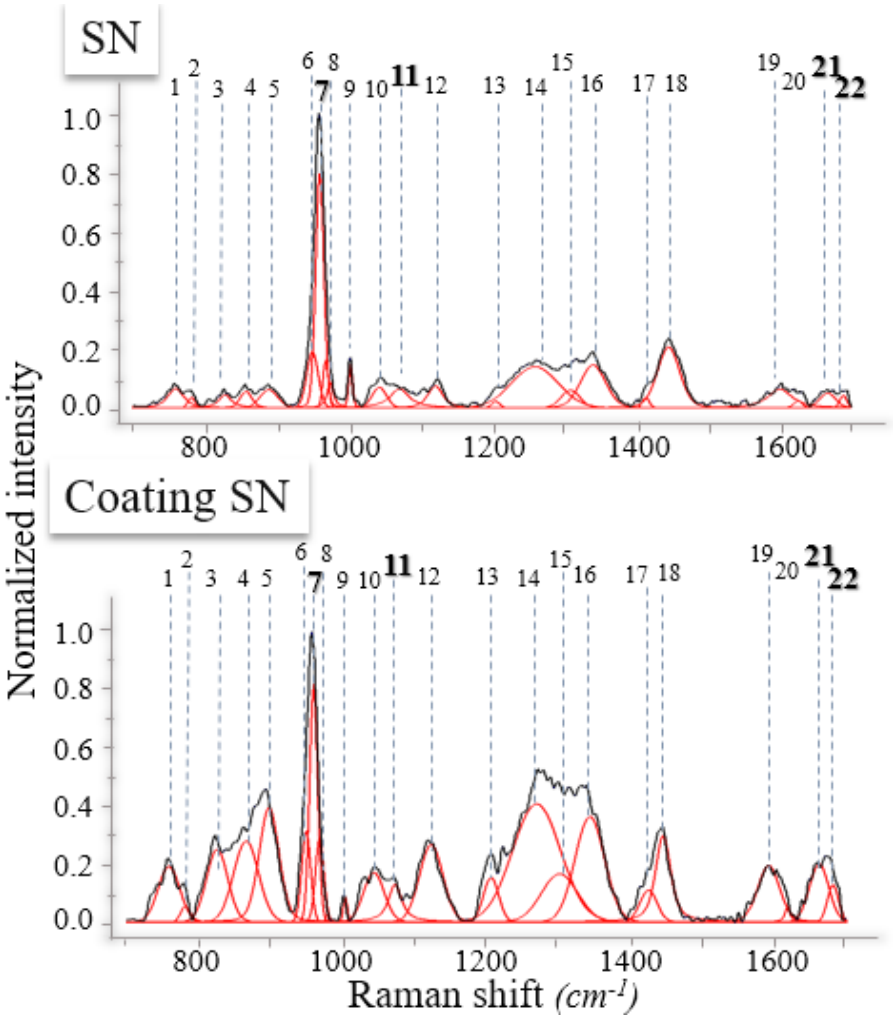

Figure 4.19: Raman spectra zirconia coated with silicon nitride (CoatingSN) and stoichiometric silicon nitride (SN) samples after the SaOS-2 osteosarcoma test.

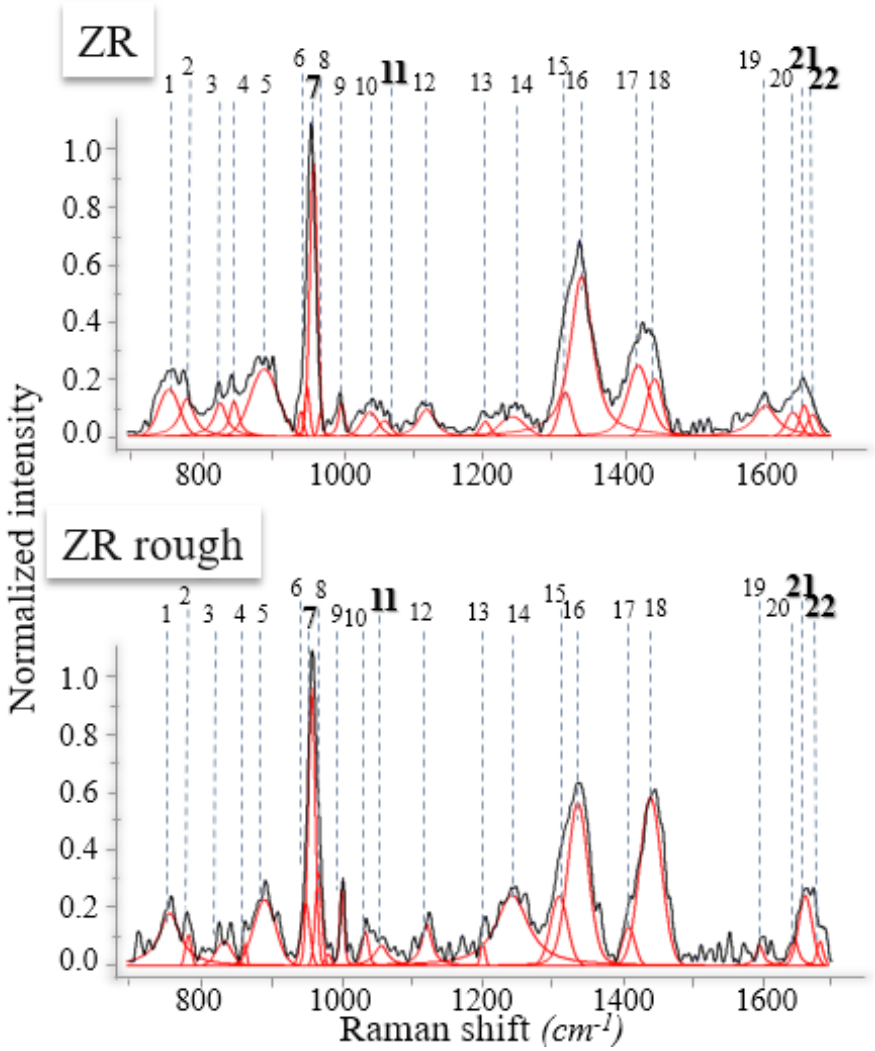

Figure 4.20: Raman spectra of zirconia polished (ZR) and zirconia rough (ZR rough) samples after the SaOS-2 osteosarcoma test.

	RAMAN SHIFT (cm^{-1})	ASSIGNEMENT	REFERENCE
1	750	phosphatidylserine	[258] [259] [262]
1	784	tryptophan symmetric breathing	[271]
3	827	O−P−O asymmetric stretching in DNA	[262] [258] [259]
4	856	C−C stretching of proline ring and ring breathing in tyrosine	[271] [264]
5	896	C−C skeletal stretching of proline in α-helix	[262] [259]

6	947	hydroxyapatite PO_4 symmetric stretching	[265]
7	961	hydroxyapatite PO_4 symmetric stretching	[265]
8	975	hydroxyapatite PO_4 symmetric stretching	[265]
9	1002	symmetric ring breathing in phenylalanine	[262] [258]
10	1037	C−H in-plane bending in phenylalanine	[262] [258]
11	1070	CO_3 symmetric stretching	[265] [266]
12	1125	C−C stretching acyl backbone in lipids	[262]
13	1207	C−C stretching lipids	[262]
14	1254	amide III in β-sheet, α-helix, and proteins	[259] [267]
15	1310	CH_2 twisting in lipid	[268]
16	1339	CH_2/CH_3 wagging and twisting in tryptophan/DNA	[262]
17	1402	bending of methyl bond in the membrane	[269]
18	1447	CH_2 bending of proteins and lipids	[270]
19	1598	N−H bending and C−N stretching amide II	[270]
20	1613	C=C stretching in tyrosine and tryptophan	[264]
21	1658	C=C stretching in lipids and amide I in α-helix (non-reducible collagen)	[271]
22	1691	C=O stretching and amide I (reducible collagen)	[272] [270] [273] [267] [269] [274]

Table 4.2: Peaks assignments Raman after the SaOS-2 osteosarcoma test.

4.3.4 Bone Quality indices

Raman quality indices were used to investigate the efficacy of SaOS-2 osteosarcoma on samples of zirconia coated with silicon nitride (CoatingSN) and stoichiometric silicon nitride (SN), rough zirconia (ZR rough) and polished zirconia (ZR).

Table 4.3 shows all the Raman shifts with the relative vibration characteristic of each band. The bands used to evaluate the quality indexes are shown below:

	RAMAN SHIFT (cm^{-1})	ASSIGNEMENT
7	961	hydroxyapatite PO_4 symmetric stretching
11	1070	CO_3 symmetric stretching
21	1658	C=C stretching in lipids and amide I in α-helix (non-reducible collagen)
22	1691	C=O stretching and amide I (reducible collagen)

Table 4.3: Peaks assignments Raman after the SaOS-2 osteosarcoma test.

The quality indexes analysed were:

Collagen maturity ratio: the ratio I_{1658}/I_{1691} gives the relative amount of cross-linking collagen and defines bone maturation.

CPR -Carbonate-to-Phosphate Ratio: the ratio I_{1070}/I_{961} gives the relative bone mineral composition. In the HA there is a exchange between PO_4^{3-} (trivalent) and $CO3^{2-}$ (divalent), this involves the loss of crystallinity and the increase in solubility.

MMR -mineral-to-matrix-ratio: the ratio I_{961}/I_{1658} and I_{1070}/I_{1658} gives the relative measure of the amount of mineralization in bone, provides information on bone tissue compositions.

Collagen maturity ratio: was evaluated by the ratio of 1658 cm^{-1} area to 1691 cm^{-1} secondary structures in the spectral region of amide I, and in particular the alpha-helix secondary structure of the collagen protein. This ratio represents the cross-linking of non-reducible (trivalent) and reducible (divalent) collagen [275] [276]. In the case of an increase in ratio, the variation represents an increase in the amount of non-reducible trivalent cross-linking due to the transformation of the divalent reducible collagen type and/or after the reduction of the reducible collagen type or its reduced formation. The enzyme lysil oxidase is able to oxidize the nitrogen binding and change the order of cross-linking. The amine changes from a secondary to a tertiary structure, thus increasing the number of cross-linking between the collagen fibres. Lysyl oxidase-generated intermolecular cross-links are essential for the tensile strength of collagen fibrils [277]. In addition, cross-links give a measure of bone condition because they increase over time, making the bone stronger and more resistant [278].

In Figure 4.21 it can be observed that the maturity ratio of the collagen of bone tissue developed by osteosarcoma cells on the ZR rough and ZR was relatively small, representing a low level of cross-linking and a high amount of reducible collagen. Tissue grown on SN and Coating SN

had a higher degree of cross-linking, which is associated with a faster development of non-reducible, cross-linked tissue.

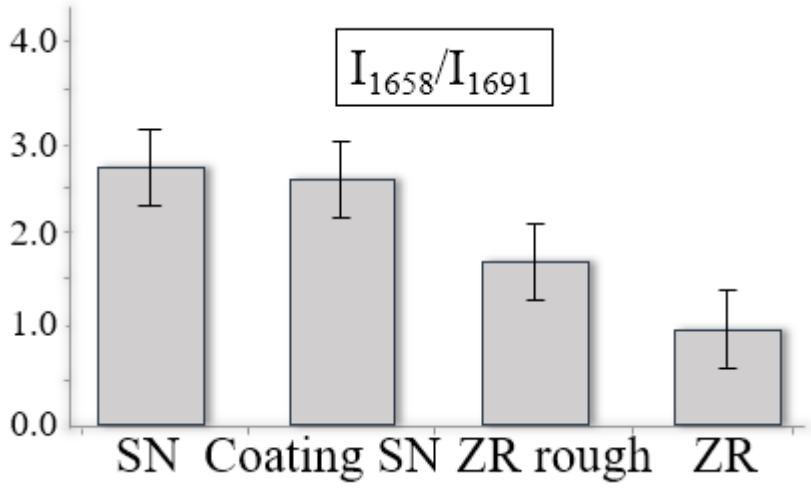

Figure 4.21: Collagen maturity ratio for the various samples as obtained from the intensity of the Raman bands at 1658 and 1691 cm^{-1}.

CPR - Carbonate-to-Phosphate Ratio: was evaluated by the ratio between the carbonate band at 1070 cm^{-1} and the phosphate band 1691 cm^{-1} and gives the relative bone mineral composition. In $Ca_{10}(PO_4)_6(OH)_2$ ion replacements CO_3^{2-} with PO_4^{3-} occur regularly, causing a decrease in the level of crystallinity, weakening the bonds and increasing mineral solubility [279] [280] [281]. Phosphates are trivalent (they bind through three bonds), while carbonates are divalent (they bind through two bonds) and this substitution causes holes in the crystalline lattice that generates the formation of defects. The substitution of carbonate (CO_3^{2-}-) in normal bone contains 2-8 wt% [276] [282] [283], a value that, if compared to Raman, corresponds to the range 0.125 - 0.5 [284]. In Figure 4.22 it can be observed that the amount of carbonate hydroxyapatite formed on zirconium substrates was significantly lower than the stoichiometric reference of silicon nitride and Coating SN which have values in the range. The results for ZR, in particular while ZR rough barely reached the minimum acceptable value.

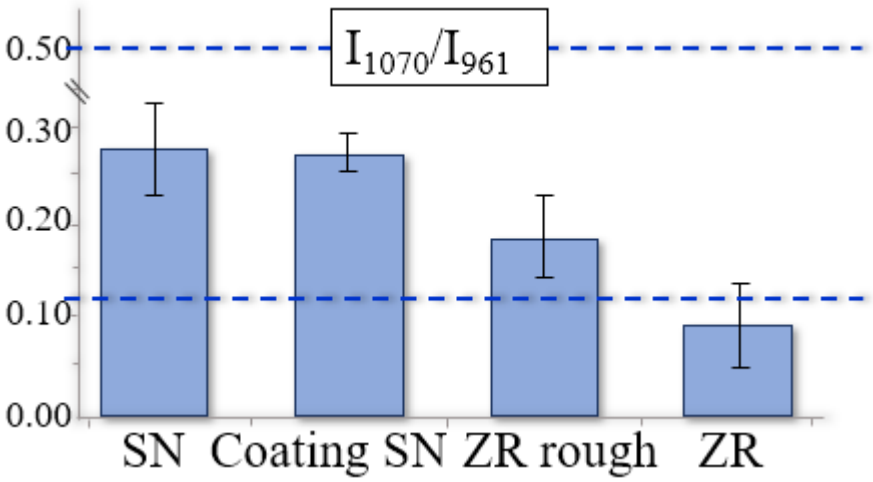

Figure 4.22:3 Carbonate-to-phosphate ratio for the various samples as obtained by the intensity of the Raman bands at 1070 and 961 cm^{-1}.

MMR - mineral to matrix ratio: is calculated as the ratio between the intensities of the Raman bands specific to the mineral (phosphate and carbonate bands at 961 and 1070 cm^{-1}, respectively) and the intensity of the amide I band (irreducible collagen) at 1658 cm^{-1}. It provides a measure of the amount of mineralization in bone and bone tissue composition [285]. In particular, an increase of MMR above the limit value causes an increase in the bone mineral matrix of CO_3^{2-} and PO_4^{3-}, which increases bone hardness [286]. On the other hand, a decrease causes bone tissue without crystallinity, but with a large quantity of collagen. The minimum Raman limit values are: 0.9 for CO_3^{2-} / irreducible collagen and 4.9 for PO_4^{3-}/ irreducible collagen [287]. In the Figure 4.23 it can be seen that three of the four samples tested meet both requirements, the only exception is the area of ZR, for which the ratio of carbonate to irreducible collagen was below the minimum value. The best scores were obtained for stoichiometric silicon nitride, which showed ratios well above the threshold values. Coating SN showed intermediate values and barely met both requirements, while, ZR rough with more intense phosphate bands and Coating SN with more carbonate.

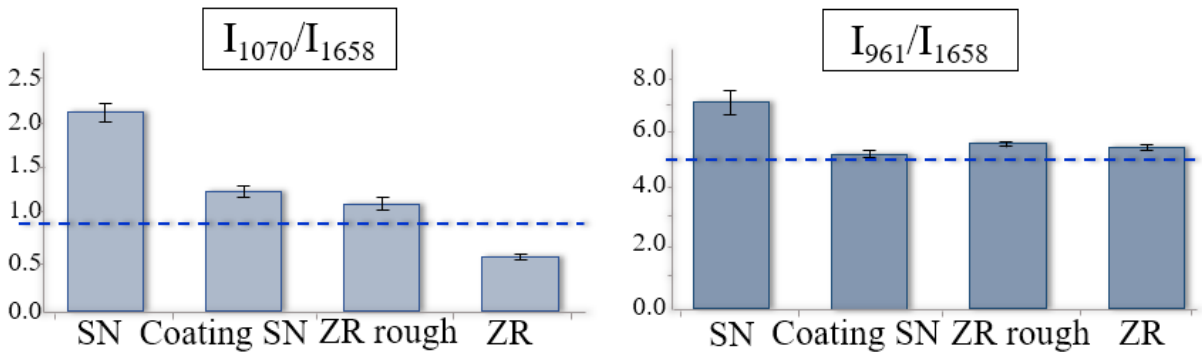

Figure 4.23:4 Mineral-to-matrix ratio for the various samples as obtained by the intensity of the Raman bands at 961 and 1658 cm^{-1} and at 1070 and 1658 cm-^{1}.

4.3.5 Scanning Electron Microscopy

Zirconia coated with silicon nitride (CoatingSN), stoichiometric silicon nitride (SN) rough zirconia (ZR rough) and polished zirconia (ZR) samples were characterized at Scanning Electron Microscopy after 10 days of exposure with SaOS-2 osteosarcoma (Fig.4.24). SEM images were stained to highlight the main elements of bone, particularly hydroxyapatite. The results got show that all samples have hydroxyapatite on the surface. Moreover, the Coating SN and ZR samples present a non-granular surface because they were crushed during the experiment. SN has the highest amount of HA and appears to show the highest amount of phosphorus (P) together with Coating SN, whereas ZR and ZR rough appear to have a higher amount of calcium (Ca). For a further analysis the stoichiometric calcium/phosphorus ratio (Ca/P) was calculated. The ratio Ca/P gives the relative measure of the amount of mineralization in bone and provides information on bone tissue compositions.

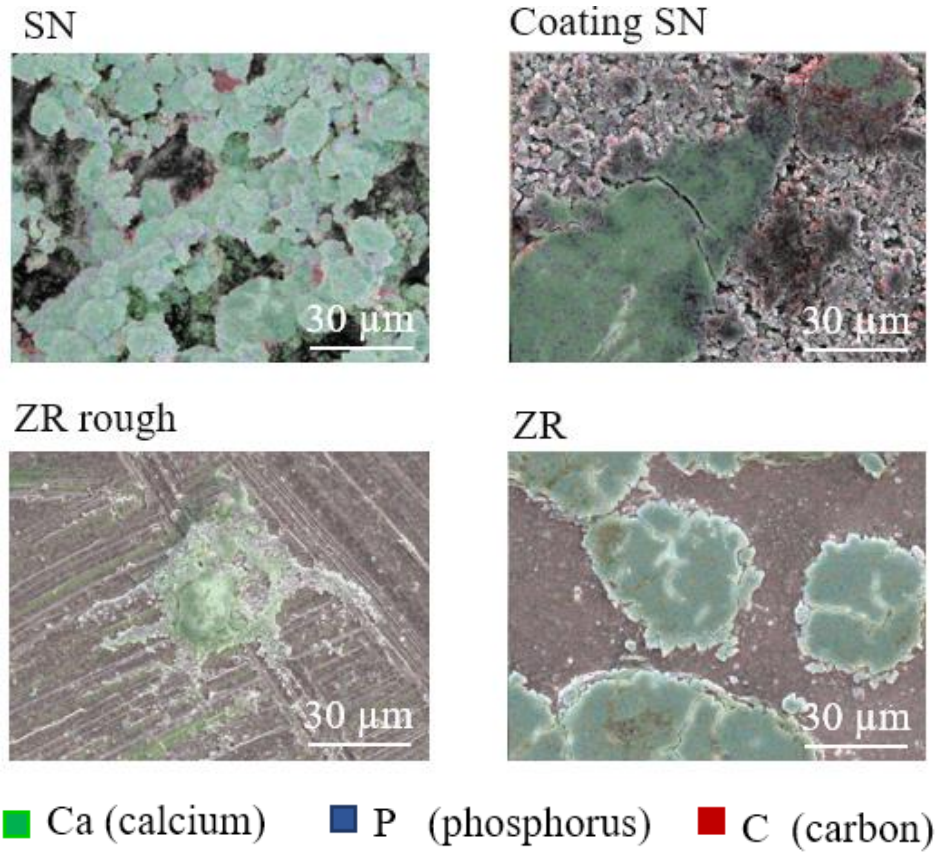

Figure 4.24: Scanning electron microscopy for the various samples after the SaOS-2 osteosarcoma test.

HA has a stoichiometric Ca/P ratio of 1.67, however the natural mineral component of bone is mainly non-stoichiometric HA (with a Ca/P ratio other than 1.67). In fact, HA can be found in

different chemical structures, which alter its crystallinity and surface area modifying its behaviour in a biological environment. It has been shown that calcium-deficient is more biodegradable than stoichiometric HA due to its low crystallinity [288], as it is able to increase the solubility and in vivo resorption capacity of composite materials [289]. The Ca/P ratios as a function of stoichiometry:

Ratio *Ca/P*	Name	Formula
	Calcium hydroxide	$Ca(OH)_2$
1 .67	**HA stoichiometric**	**$Ca_{10}(PO_4)_6(OH)_2$**
1.5	Tricalcium phosphate (β-TCP)	$Ca_3(PO_4)_2$
1.0	Dicalcium phosphate	$CaHPO_4$

Table 4.4: Ratio Ca/P of the SEM analysis.

A higher ratio leads to the formation of calcium hydroxide ($CaOH_2$) in addition to HA which generates an increase in pH of the solution. The solution becomes more basic. The presence of $CaOH_2$ in the structure is ideal for dental composite applications. In fact, this leads to an increase in the amount of free $CaOH_2$ and its dissolution in the environment which increases the pH and reduces the growth of bacteria. $CaOH_2$ has antibacterial characteristics, improves the release of enzymes and growth factors and increases the rate of drug release [290] [291]. The Figure shows the Ca/P ratio for all samples and it is evident that the SN and Coating SN samples show a value below the stoichiometric value, 1.49 and 1.25 respectively. It can be assumed that both forms are β-TCP with a minimal presence of HA. This difference between Coating SN and SN may be due to the large amount of collagen in the coating, as demonstrated by the Raman spectrum of HA. Collagen causes a decrease in the crystallinity of HA. On the other hand, zirconia samples have a much higher value than stoichiometric (ZR 2.65 and ZR rough 3.55) which shows the presence of $Ca(OH)_2$. In this case the presence of calcium hydroxide is a side effect derived from the precipitation of $Ca(OH)_2$ in solution. Calcium ion in solution precipitates easily.

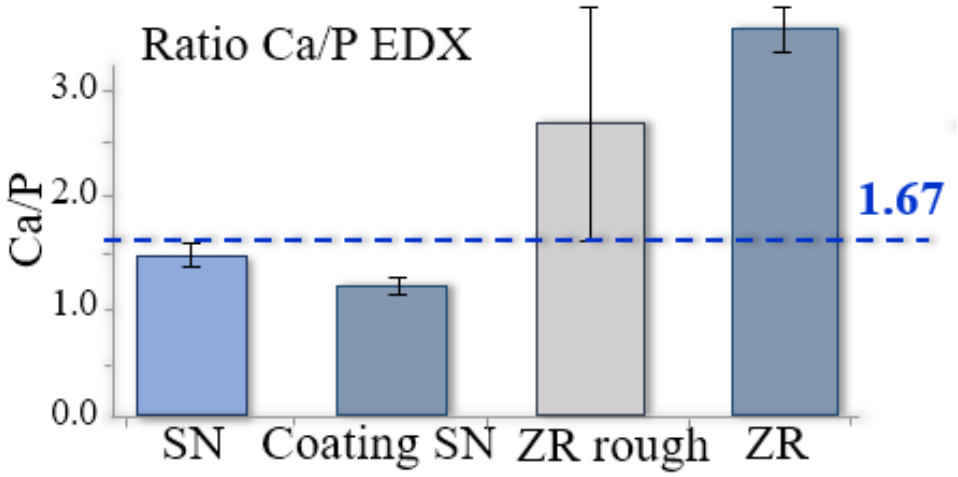

Figure 4.25: Ca/P ratio for the various samples as obtained by scanning electron microscopy after the SaOS-2 osteosarcoma test.

Chapter 5

Discussion

This study was performed to investigate the ability of a silicon nitride coating on zirconia substrates for dental prosthesis applications. The coated silicon nitride sample (Coating SN) was compared to stoichiometric silicon nitride (SN) used as positive samples and samples of polished (ZR) and rough (ZR rough) zirconia. The coating of silicon nitride on dental zirconium substrates, led to the formation of a coarse layer of ceramic particles embedded in a silicon metal matrix, presumably composed of both amorphous and nanocrystalline domains.

The laser microscope analysis showed a homogeneously distributed coating, but with the presence of holes (white spots). Moreover the different thermal coefficient [222] [223] [224], between zirconia and silicon nitride caused the deamination process, that is a contraction between the grains forming folds and cracks. The presence of scratches on the zirconia allowed to reduce the stresses (Fig. 4.0 and 4.1).

The FT-IR analysis (Fig.4.4) shows a different behaviour from that of stoichiometric silicon nitride. Coating SN does not present a crystalline Si_3N_4 structure, but an amorphous Si(3+x)N(4-y) structure with an increase in oxygen and nitrogen loss. The analysis by Raman spectroscopy (Fig. 4.6) showed the presence only of the band related to Si-Si bonds at 520 cm-1 [236]. There is no presence of Si_3N_4, but as reported in the literature, the Raman dispersion alone cannot provide unambiguous information on the size, fraction and distribution of crystallites [292]. The XPS analysis gave further insights into the composition and chemical structure of the layer (Fig. 4.7). It was observed that out of a total of 34% Silicon only 9% is Si_3N_4, the rest is silicon or silicon oxide (SiO2), so only 38% of the total is Si_3N_4. The presence of SiO2 in high concentration is presumably due to the reaction between water (atmospheric humidity) and silicon (Si-Si), which produces a thin and uniform layer of passivation on the silicon particles. The passivated layer corresponds to the oxidation of silicon SiO2.

The reaction rate increases as the average diameter of the particles becomes smaller [245]. On the zirconium sample coated with silicon nitride there was a passivated layer during deposition, caused by possible initial oxygen sources. The oxygen present was limited to the gas trapped in the powder or chemically bound to silicon nitride in the form of silicon oxide or silicon oxide.

It is assumed that the zirconium oxide sample coated with silicon nitride has trans-micrometric and sub-micrometric particles and the passivation reaction can be considered instantaneous. This thesis is supported because it was possible to observe an intermediate phase of silicon nitride oxy-nitride at about 398 eV (N1s). SEM analysis It was observed that out of a total of 56% Silicon only 28% is Si_3N_4, the rest is silicon or silicon oxide (SiO_2), only 50% of the total is Si_3N_4, which shows a large amount of the passivated layer.

Coating SN treated with Staphylococcus epidermidis bacteria under aerobic conditions for 12; 24; 48 hours, showed poor antibacterial behaviour. This result can be explained by the low amount of nitrogen on the surface and a large amount of a passivated layer (SiO_2), since nitrogen is the vector of antibacterial behaviour in silicon nitrides [39] [38]. Analysis by Raman spectroscopy (Fig. 4.11 and Tab. 4.2) showed that all surfaces were colonized by bacteria. Fluorescence microscopic images (Fig. 4.12; 4.13; 4.14) showed that Coating SN and SN exhibit the highest number of dead cells on the surface, but a large number of living cells are still present. This particular fact suggests poor antibacterial behaviour and it can also be applied to zirconia samples. The WST analysis (Fig.4.15 and Tab .4.1) allowed the calculation of the bacterial death rate. Coating SN showed very low antibacterial properties. Stoichiometric silicon nitride also showed a low bacterial death rate trend. The ZR rough instead, The raw ZR on the other hand, contrary to what was expected, which has an antibacterial behaviour absent [130], it appears to have the best bacterial death rate. This result is anomalous because, as reported in the literature, silicon nitride has good antibacterial properties [39] [38].

The particular surface structure of Coating SN differs from that of stoichiometric silicon nitride (SN), which has a different cellular response of SaOS-2 osteosarcoma. In that, fluorescence microscopic analysis (Fig. 4.16) showed a homogeneous cell adhesion of Coating SN, but a lower proliferation compared to SN, which effectively stimulates cell proliferation. This result was also confirmed by the pixel count in FM images (Fig. 4.17). The presence of a low proliferation can be seen in the literature from the osteoinductive properties of silicon nitride. The nitrogen provided by Si_3N_4 can be partially released from the surface and used as a nutrient to stimulate cell differentiation and proliferation [293] [294] [295]. In addition, the pixel count showed that Coating SN has an increase in extra cellular matrix, osteopontine and osteocalcin (OC, OPN) compared to the number of nuclei (DAPI). The presence of these two proteins in bone tissue has the following effects considered synergistic, osteocalcin [296] is mainly observed in mineralized tissue while osteopontine [297] is often associated with bone remodeling. This result does not have an active effect on Coating SN, but a better proliferation of osteoblasts, which stimulates the production of bone tissue. This result may suggest a higher

rate of osseointegration. Furthermore, these results are confirmed by the literature on the positive effects of silicon on bone tissue [298] [299] [300] and can be explained by the high bioavailability of silicon from amorphous and nanocrystalline sources compared to macroscopic crystals [301]. WST analysis (Fig.4.18) showed a cellular adhesion of Coating SN similar to zirconia samples and lower than SN, due to a low nitrogen concentration of Coating SN [293] [294] [295]. The Raman analysis (Fig.4.20) showed a higher presence of Amide I II and III bands which is probably due to an increase of collagen (OPN, OC) in the bone structure and this is consistent with FM results. Through the Raman spectra the "quality index" parameters Collagen maturity ratio, CPR and MMR were studied (Fig. 4.21; 4.22; 4.23). and it is observed that the Coating SN shows values similar to SN, with parameters within the range. The Raman analysis (Fig.4.24 and Tab. 4.4) studied the calcium/phosphate (Ca/P) ratio of hydroxyapatite. It was observed that zirconia has a value above the stoichiometric ratio, due to a side effect derived from the precipitation of Ca(OH)2 in solution. Coating SN has the lowest ratio, while stoichiometric nitride has a value more similar to stoichiometric and the reason is because of an higher P contraction in Coating SN which is consistent with all results, as the amount of extracellular matrix is higher.

Chapter 6

Conclusion

This study characterized the properties of silicon nitride coating on dental zirconia for dental implant applications. This coating proved to be completely homogeneous with the presence of small holes and high roughness (laser microscope), moreover it is presented in the form of silicon nitride particles in a matrix of nanocrystalline and amorphous metallic silicon (FT-IR, Raman, SEM, XPS).

The coating of silicon nitride has an antibacterial effect (with staphylococcus epidermidis bacteria), but less than expected (FM,WST). It also does not contribute to the proliferation of SaOS-2 cells (FM, WST), but promotes the stimulation of bone tissue formation (FM), as a large amount of extracellular matrix is present in the formed bone (Raman, SEM) and bone quality indexes are all within the acceptable range. In conclusion, this study has proven that silicon nitride coating on zirconia could be a good solution to improve dental implant technology.

Chapter 7

Bibliography

[1] Beumer J., Lewis S.G., Il sistema implantologico Brånemark: procedure cliniche e laboratorio Edinava; 1990.

[2] Rickard Brånemark, MD, PhD; P-I Brånemark, MD, PhD; Björn Rydevik, MD, PhD; Robert R. Myers, PhD , Osseointegration in skeletal reconstruction and rehabilitation. A review; 2001, 175–181.

[3] Lindquist LW, Carlsson GE, Jemt T. A prospective 15-year follow-up study of man- dibular fixed prostheses supported by osseointegrated implants. Clinical results and marginal bone loss. Clin Oral Implants Res; 1996;7 (4):329–36.

[4] Evrard L, Waroquier D, Parent D. Allergies to dental metals. Titanium: a new allergen. Rev Med Brux; 2010, 31(1):44–9.

[5] Pigatto PDPD, Guzzi G, Brambilla L, Sforza C. Titanium allergy associated with dental implant failure. Clin Oral Implants Res; 2009, 20(8):857.

[6] Sicilia A, Cuesta S, Coma G, Arregui I, Guisasola C, Ruiz E, . Titanium allergy in dental implant patients: a clinical study on 1500 consecutive patients. Clin Oral Implants Res; 2008, 19(8):823–35.

[7] Koutayas SO, Vagkopoulou T, Pelekanos S, Koidis P, Strub JR. Zirconia in dentistry: part 2. Evidence-based clinical breakthrough. Eur J Esthet Dent; 2009, 4(4):348–80.

[8] Onodera K, Ooya K, Kawamura H. Titanium lymph node pigmentation in the recon- struction plate system of a mandibular bone defect. Oral Surg Oral Med Oral Pathol; 1993, 75(4):495–7.

[9] Jacobs JJ, Skipor AK, Patterson LM, Hallab NJ, Paprosky WG, Black J, . Metal release in patients who have had a primary total hip arthroplasty: a prospective, controlled, longitudinal study. J Bone Joint Surg Am; 1998, 80(10):1447–58.

[10] Evrard L, Waroquier D, Parent D. Allergies to dental metals. Titanium: a new allergen. Revue Medicale de Bruxelles; 2010, 31(1):44-49.

[11] Bågedahl-Strindlund M, Tomson Y, Larsson KS, SandborghEnglund G. A multidisciplinary clinical study of patients suffering from illness associated with mercury release from dental restorations: psychiatric aspects. Acta Psychiatr Scand; 1997, 96(6):475–82.

[12] Denry, I., & Kelly, J. R. State of the art of zirconia for dental applications. Dental ma-terials; 2008 24(3), 299-307.

[13] Vagkopoulou, T., Koutayas, S. O., Koidis, P., & Strub, J. R. Zirconia in dentistry: Part 1. Discovering the nature of an upcoming bioceramic. European Journal of Es-thetic Dentistry. 2009, 4(2).

[14] Chevalier, J., Gremillard, L., & Deville, S. Low-temperature degradation of zirconia and implications for biomedical implants. Annu. Rev. Mater. Res; 2007, 37, 1-32.

[15]] Zhu, W.,Marin, E., ... & Pezzotti, G. Mechanisms induced by transition metal con-taminants and their effect on the hydrothermal stability of zirconia-containing bioc-eramics: an XPS study. Physical Chemistry Chemical Physics; 2018, 20(45), 28929-28940.

[16] W.E. Lee e W.M. Rainforth, Ceramic Microstructure - property control by processing. Chapman & Hall, London; 1994.

[17] C. Piconi, W. Burger, H. G. Richter, a. Cittadini, G. Maccauro, V. Covacci, N. Bruzzese, G. a. Ricci, and E. Marmo. Y-TZP ceramics for artificial joint replacements. Biomaterials; 1998, 19(16):1489–1494.

[18] J J Swab. Low temperature degradation of Y-TZP materials. Journal of Materials;1991, 6706-6714.

[19] Covacci V, Bruzzese N, Maccauro G, Andreassi C, Ricci G, Piconi C, Marmo E, Burger W, Cittadini A. In vitro evaluation of the mutagenic and carcinogenic power of high purity zirconia ceramic. Biomaterials; 1999, 20: 371– 376.

[20] Afzal, A. Implantable zirconia bioceramics for bone repair and replacement: A chrono-logical review. Materials Express; 2014, 4(1), 1-12.

[21] Scarano, A., Di Carlo, F., Quaranta, M., & Piattelli, A. Bone response to zirconia ce-ramic implants: an experimental study in rabbits. Journal of Oral Implantology 2003, 29(1), 8-12.

[22] Rapacz-Kmita, A., Ślósarczyk, A., Paszkiewicz, Z., & Paluszkiewicz, C. Phase stabil-ity of hydroxyapatite–zirconia (HAp– ZrO_2) composites for bone replacement. Journal of molecular structure; 2004, 704(1-3), 333-340.

[23] Aldini, N. N., Fini, M., Giavaresi, G., Martini, L., Dubini, B., Bossi, M. P., ... & Giardino, R. Osteointegration of bioactive glass-coated and uncoated zirconia in oste-openic bone: an in vivo experimental study. Journal of Biomedical Materials Research; 1995, 29, 349–57.

[24] Hao, L., Lawrence, J., & Chian, K. S. Osteoblast cell adhesion on a laser modified zirconia based bioceramic. Journal of Materials Science: Materials in Medicine. 2005, 16(8), 719-726..

[25] Gahlert, M., Gudehus, & Erhardt, W. Biomechanical and histomorphometric compari-son between zirconia implants with varying surface textures and a titanium implant in the maxilla of miniature pigs. Clinical oral implants research; 2007, 18(5), 662-668.

[26] Thian, E., Huang, J., Best, S., Barber, Z. & Bonfield, W. Silicon-substituted hydroxyapatite: The next generation of bioactive coatings. Materials Science and Engineering; 2007, C 27, 251–256.

[27] Whitehead, M. A. et al. High-porosity poly (ε-caprolactone)/mesoporous silicon scaffolds: calcium phosphate deposition and biological response to bone precursor cells. Tissue Engineering Part A; 2008, 14, 195–206.

[28] Calvo-Guirado, J. L. et al. Biphasic β-TCP mixed with silicon increases bone formation in critical site defects in rabbit calvaria. Clinical oral implants research; 2015, 26, 891–897.

[29] Neumann A, Unkel C, Werry C, et al. Osteosynthesis in facial bones. Silicon nitride ceramic as material. HNO; 2006, 54:937–42.

[30] Neumann A, Unkel C, Werry C, et al. Prototype of a silicon nitride ceramicbased miniplate osteofixation system for the midface. Otolaryngol Head Neck; 2006,134:923–30.

[31] Khandkar A, Lakshminarayanan R, Clarke I, Hoffman AA, Rahaman MN. Testing of silicon nitride ceramic bearings for total hip arthroplasty. J Biomed Mater Res B; 2008, 87:447–54.

[32] Shepherd, J. H., Shepherd, D. V. & Best, S. M. Substituted hydroxyapatites for bone repair. Journal of Materials Science: Materials in Medicine; 2012, 23, 2335–2347.

[33] Escott-Stump, S. Nutrition and diagnosis-related care. (Lippincott Williams & Wilkins, 2008).

[34] Rizzo, D. C. Fundamentals of anatomy and physiology. (Cengage Learning, 2015). 20 Pezzotti, G. et al. Silicon Nitride Bioceramics Induce Chemically Driven Lysis in Porphyromonas gingivalis. Langmuir; 2016, 32, 3024–3035.

[35] Pezzotti, G. et al. Silicon Nitride Bioceramics Induce Chemically Driven Lysis in Porphyromonas gingivalis. Langmuir; 2016, 32, 3024–3035

[36] Bock, R. M. et al. Surface modulation of silicon nitride ceramics for orthopaedic applications. Acta biomaterialia; 2015, 26, 318–330.

[37] Pezzotti, G. et al. Silicon Nitride: A Synthetic Mineral for Vertebrate Biology. Sci. Rep., 2016; 1121–1134.

[38] G. Pezzotti et al., “Silicon nitride bioceramics induce chemically driven lysis in Porphyromonas Gingivalis,” Langmuir; 2016; 32 3024 –3035.

[39] Francesco Boschetto; Tetsuya Adachi; Satoshi Horiguchi; Danny Fainozzi; Fulvio Parmigiani; Elia Marin; Wenliang Zhu; Bryan J. McEntire; Toshiro Yamamoto; Narisato Kanamura; Osam Mazda; Eriko Ohgitani; Giuseppe Pezzotti "Monitoring metabolic reactions in Staphylococcus epidermidis exposed to silicon nitride using in situ time-lapse Raman spectroscopy. J. Biomed. Opt.; 2018, 23(5)

[40] Fergal J.O'Brien. Biomaterials & scaffolds for tissue engineering. Materials Today; 2011, vol.14, 88-95.

[41] Giuseppe Pezzotti, Elia Marin, Tetsuya Adachi, Alfredo Rondinella, Francesco Boschetto, Wenliang Zhu, Nobuhiko Sugano, Ryan M. Bock, Bryan McEntire & Sonny B. Bal. Bioactive silicon nitride: A new therapeutic material for osteoarthropathy. Sci. Rep; 2017.

[42] L. Hench, L. Larry e J. Wilson. An Introduction to Bioceramics, II. Imperial College Press; 2013.

[43] W.F. Smith, "Principles of Materials Science and Engineering", seconda edizione, McGraw-Hill Publishing Company, New York 1999.

[44] R.W. Davidge, Mechanical behaviour of ceramics, Cambridge University Press, Cambridge; 1979..

[45] Riley FL. Silicon nitride and related materials. J Am Ceram Soc; 2000, 83:245–65.

[46] Frank L. Riley "Silicon Nitride and Related Materials" J. Am. Ceram. Soc.; 2000, 83 [2] 245–65.

[47] Brook RJ, editor. Concise encyclopedia of advanced ceramic materials. Oxford: Pergamon Press; 1991.

[48] Supancic P, Danze R, Harrer W, Wang Z, Witschnig S, Schöppl O. Strength tests on silicon nitride balls. Key Eng Mat; 2009, 409:193–200.

[49] Wang W, Hadfield M, Wereszczak AA. Surface strength of silicon nitride in relation to rolling contact performance. Ceram Int; 2009, 35:3339–46.

[50] Wang L, Snidle RW, Gu L. Rolling contact silicon nitride bearing technology: a review of recent research. Wear; 2000, 246:159–73.

[51] Howlett CR, McCartney E, Ching W. The effect of silicon nitride ceramic on rabbit skeletal cells and tissue. An in vitro and in vivo investigation. Clin Orthop Relat Res; 1989, 244:293–304.

[52] Neumann A, Jahnke K, Maier HR, Ragoß C. Biocompatibility of silicon nitride ceramic in vitro. A comparative fluorescence-microscopic and scanning electron-microscopic study. Laryngorhinootologie; 2004,83:845–51.

[53] Kitayama M., K. Hirao, M. Toriyama, and S. Kanzaki. "Modeling and simulation of grain growth in Si_3N_4-Anisotropic Ostwald ripening." Acta materialia; 1998, 46, no. 18: 6541-6550.

[54]] Jiang J. Z., Flemming Kragh, D. J. Frost, and H. Lindelov. "Hardness and thermal stability of cubic silicon nitride." Journal of Physics: Condensed Matter; 2001, 13, 22: L515.

[55] Riley Frank L. Silicon Nitride and Related Materials. Journal of the American Ceramic Society. 2004, 83 (2): 245-265.

[56] M. Rahaman, Y. Boiteux, L. DeJonghe Surface characterization of silicon nitride and silicon carbide powders Bull. Am. Ceram. Soc.; 1986, 65, 1171-1176.

[57] Fischer TE, Tomizawa H. Interaction of tribochemistry and microfracture in the friction and wear of silicon nitride. Wear 1985;105:29–45.

[58] Ishigaki H, Nagata R, Iwasa M. Effect of adsorbed water on friction of hotpressed silicon nitride and silicon carbide at slow speed sliding. Wear, 1988,121:107–16.

[59] Takadoum J, Houmid-Bennani H, Mairey D. The wear characteristics of silicon nitride. J Eur Ceram Soc; 1998,18:553–6.

[60] Lee KH, Kim KW. Effects of humidity and sliding speed on the wear properties of Si_3N_4 ceramics. Mater Sci Eng A; 1989,186:185–91.

[61] Saito T, Imada Y, Honda F. An analytical observation of the tribochemical reaction of silicon nitride sliding with low friction in aqueous solutions. Wear; 1997, 205:153–9..

[62] Maw W, Stevens F, Langford SC, Dickinson JT. Single asperity tribochemical wear of silicon nitride studied by atomic force microscopy. J Appl Phys; 2002, 92:5103–9.

[63] Amutha Rani D, Yoshizawa Y, Jones MI, Hyuga H, Hirao K, Yamauchi Y. Comparison of tribological behavior between a-Sialon/ Si_3N_4 and Si_3N_4/ Si_3N_4 sliding pairs in water lubrication. J Am Ceram Soc; 2005, 88:1655–8.

[64] Sasaki S. The effects of the surrounding atmosphere on the friction and wear of alumina,zirconia,siliconcarbide andsiliconnitride.Wear; 1989, 134:185–200.

[65] Zhou YS, Ikeuchi K, Ohashi M. Comparison of the friction properties of four ceramic materials for joint replacements. Wear; 1997, 210:171–7.

[66] Kusaka J, Takashima K, Yamane D, Ikeuchi K. Fundamental study for allceramic artificial hip joint. Wear; 1999, 225–229:734–74.

[67] NIST-JANAF Thermochemical Tables, 2015.

[68] S.I. Raider, R. Flitsch, J.A. Aboaf, W.A. Pliskin Surface oxidation of silicon nitride films J. Electrochem. Soc.; 1976, 123. 560-565.

[69] L. Bergström, R.J. Pugh Interfacial characterization of silicon nitride powders J. Am. Ceram. Soc.; 1989, 72, pp. 103-109.

[70] V.A. Hackley, P. Sen Wang, S.G. Malghan Effects of soxhlet extraction nitride powders on the surface oxide layer of silicon nitride powders Mater. Chem. Phys., 36 (1993), pp. 112-118.

[71] D.P. Butt, D. Albert, T.N. Taylor Kinetics of thermal oxidation of silicon nitride powders J. Am. Ceram. Soc.; 1996, 79, pp. 2809-2814.

[72] J. Szépvölgyi, I. Mohai, J. Gubicza Studies on atmospheric ageing of nanosized silicon nitride powders Key Eng. Mater.; 2004, 264–268, pp. 2311-2314.

[73] G. Busca, V. Lorenzelli, G. Porcile, M.I. Baraton, P. Quintard, R. Marchand FT-IR study of the surface properties of silicon nitride Mater. Chem. Phys.;1986, 14, pp. 123-140.

[74] S. Mezzasalma Characterization of silicon nitride surface in water and acid environment: a general approach to the colloidal suspensions J. Colloid Interface Sci.; 1996, 180, pp. 413-420.

[75] R.K. Iler The Chemistry of Silica Wiley, New York; 1979, NY.

[76] P. Greil, R. Nitzsche, H. Friedrich, W. Hermel Evaluation of oxygen content on silicon nitride powder surface from the measurement of the isoelectric point J. Eur. Ceram. Soc.; 1991, 7, pp. 353-359.

[77] J. Sonnefeld Determination of surface charge density parameters of silicon nitride Colloids Surf. A; 1996, 108, pp. 27-31.

[78] J.S. Reed Principles of Ceramics Processing (second ed.), Wiley, New York; 1995.

[79] J.N. Israelachvili Intermolecular and Surface Forces (third ed.), Academic Press, London; 2011.

[80] P. Greil Processing of silicon nitride ceramics Mater. Sci. Eng. A; 1989, 109, pp. 27-35.

[81] J.A. Lewis Colloidal processing of ceramics J. Am. Ceram. Soc., 2000, 83, pp. 2341-2359.

[82] Amutha Rani D, Yoshizawa Y, Jones MI, Hyuga H, Hirao K, Yamauchi Y. Comparison of tribological behavior between a-Sialon/ Si_3N_4 and Si_3N_4/ Si_3N_4 sliding pairs in water lubrication. J Am Ceram Soc; 2005, 88:1655–8.

[83] Xu J, Kato K. Formation of tribochemical layer of ceramics sliding in water and its role for low friction. Wear; 2000, 245:61–75..

[84] P. F. Becher. Microstructural Design of Toughened Ceramics. J. Am. Ceramic Socc; 1991, 74 (2) 255-69.

[85] F.F. Lange Relation between strength, fracture energy, and microstructure of hot-pressed Si_3N_4 J. Am. Ceram. Soc.; 1973, 56, pp. 518-522.

[86] F.L. Riley Silicon nitride and related materials J. Am. Ceram. Soc., 83 (2000), pp. 245-265.

[87] F.F. Lange The sophistication of ceramic science through silicon nitride studies J. Ceram. Soc. Jpn.; 2006, 114, pp. 873-879.

[88] P.F. Becher, E.Y. Sun, K.P. Plucknett, K.B. Alexander, C. Hsueh, H. Lin, et al. Microstructural design of silicon nitride with improved fracture toughness : I. Effects of grain shape and size J. Am. Ceram. Soc. 1998, 81, pp. 2821-2830.

[89] K. Bodišová, M. Kašiarová, M. Domanická, M. Hnatko, Z. Lenčéš, Z.V. Nováková, et al. Porous silicon nitride ceramics designed for bone substitute applications Ceram. Int; 2013, 39, pp. 8355-8362.

[90] M.P. Arts, J.F.C. Wolfs, T.P. Corbin The CASCADE trial: effectiveness of ceramic versus PEEK cages for anterior cervical discectomy with interbody fusion; protocol of a blinded randomized controlled trial BMC Musculoskelet. Disord.; 2013, 14, p. 244.

[92] R.F. Kersten, S.M. van Gaalen, M.P. Arts, K.C.B. Roes, A. de Gast, T.P. Corbin, et al. The SNAP trial: he SNAP trial: a double blind multi-center randomized controlled trial of a silicon nitride versus a PEEK cage in transforaminal lumbar interbody fusion in patients with symptomatic degenerative lumbar disc disorders: study protocol; 2014, 15:57

[93] D. W. Richerson, Modern Ceramic Engineering: Properties, Processing and Use in Design. Revised and Expanded Second ed, 1992, New York: Marcel Dekker, Inc. 5. G..

[94] Schwier, G. Nietfeld, and G. Franz, "Production and Characterization of Silicon Nitride Powders," Materials Science Forum; 1989, 47, pp. 1-20.

[95] Frieser, R. G. "Direct nitridation of silicon substrates." J. Electrochem. Soc; 1968, 115: 1092-1094..

[96] Mitomo M. "Effect of Fe and Al additions on nitridation of silicon." Journal of Materials Science; 1968, 12.2: 273-276..

[97] Pavarajarn Varong and Shoichi Kimura. "Catalytic effects of metals on direct nitridation of silicon." Journal of the American Ceramic Society; 2001, 84.8: 1669-1674..

[98] Boyer S. M. and A. J. Moulson. "A mechanism for the nitridation of Fe-contaminated silicon." Journal of Materials Science; 1978, 13, no. 8: 1637-1646. 47.

[99] Wang F, Jin G Q, Guo X Y. Formation mechanism of Si_3N_4 nanowires via carbothermal reduction of carbonaceous silica xerogels[J]. The Journal of Physical Chemistry B; 2006, 110(30): 14546-14549..

[100] Bal BS, Garino J, Ries M, Rahaman MN. Ceramic materials in total joint arthroplasty. Semin Arthroplasty; 2006, 17:94–101..

[101] Rahaman MN, Yao A, Bal BS, Garino JP, Ries MD. Ceramics for prosthetic hip and knee joint replacement. J Am Ceram Soc; 2007, 90:1965–88..

[102] R.M. Taylor, J.P. Bernero, A.A. Patel, D.S. Brodke, A.C. KhandkarSilicon nitride – a new material for spinal implants J. Bone Joint Surg. Br.; 2010, 92, p. 133.

[103] Kue R, Sohrabi A, Nagle D, Frondoza C, Hungerford D. Enhanced proliferation and osteocalcin production by human osteoblast-like MG63 cells on silicon nitride ceramic discs. Biomaterials 1999;20:1195–201.

[104] Cappi B, Neuss S, Salber J, Telle R, Knüchel R, Fischer H. Cytocompatibility of high strength non-oxide ceramics. J Biomed Mater Res A; 2010, 93:67–76..

[105] Guedes e Silva CC, Higa OZ, Bressiani JC. Cytotoxic evaluation of silicon nitride-based ceramics. Mater Sci Eng C; 2004, 24:643–6..

[106] Guedes e Silva CC, König Jr B, Carbonari MJ, Yoshimoto M, Allegrini Jr S, Bressiani JC. Tissue response around silicon nitride implants in rabbits. J Biomed Mater Res A; 2008 ,84:337–43.

[107] Becher PF, Sun EY, Plunkett KP, et al. Microstructural design of silicon nitride with improved toughness: I, effects of grain shape and size. J Am Ceram Soc; 1998, 81:2821-2830..

[108] R. Kue, A. Sohrabi, D. Nagle, C. Frondoza, D. Hungerford Enhanced proliferation and osteocalcin production by human osteoblast-like MG63 cells on silicon nitride ceramic discs Biomaterials; 1999, 20, pp. 1195-1201.

[109] C.R. Howlett, E. McCartney, W. Ching The effect of silicon nitride ceramic on rabbit skeletal cells and tissue Clin. Orthop. Relat. Res.;1989, 244, pp. 293-304.

[110] A. Neumann, T. Reske, M. Held, K. Jahnke, C. Ragoss, H.R. Maier Comparative investigation of the biocompatibility of various silicon nitride ceramic qualities in vitro J. Mater. Sci. – Mater. Med.;2005, 15, pp. 1135-1140.

[111] C. Santos, S. Ribeiro, J.K.M.F. Daguano, S.O. Rogero, K. Strecker, C.R.M. Silva Development and cytotoxicity evaluation of SiAlONs ceramics Mater. Sci. Eng.;2007, C27, pp. 148-153.

[112] C.C. Sorrell, P.H. Hardcastle, R.K. Druitt, C.R. Howlett, E.R. McCartney, Results of 15-year clinical study of reaction bonded silicon nitride intervertebral spacers, in: Proc. 7th World Biomater. Conf; 2004, 1872..

[113] A. Neumann, M. Kramps, C. Ragoß, H.R. Maier, K. Jahnke Histological and microradiographic appearances of silicon nitride and aluminum oxide in a rabbit femur implantation model Materwiss Werksttech; 2004, 35, pp. 569-573.

[114] C.C. Guedes-e-Silva, B. Konig, M.J. Carbonari, M. Yoshimoto, S. Allegrini, J.C. Bressiani Tissue response around silicon nitride implants in rabbits J. Biomed. Mater. Res., 84; 2008, pp. 337-343.

[115] M.N. Rahaman, A. Yao, B.S. Bal, J.P. Garino, M.D. RiesCeramics for prosthetic hip and knee joint replacement J. Am. Ceram. Soc., 90; 2007, pp. 1965-1988.

[116] M. Mazzocchi, A. BellosiOn the possibility of silicon nitride as a ceramic for structural orthopaedic implants. Part I: processing, microstructure, mechanical properties, cytotoxicity J. Mater. Sci. – Mater. Med., ;2008, pp. 2881-2887.

[117] M. Mazzocchi, D. Gardini, P.L. Traverso, M.G. Faga, A. BellosiOn the possibility of silicon nitride as a ceramic for structural orthopaedic implants. Part II: chemical stability and wear resistance in body environment J. Mater. Sci. – Mater. Med.; 2007, 19.

[118] B.S. Bal, M.N. RahamanOrthopedic applications of silicon nitride ceramics Acta Biomater., 8 ;2012, pp. 2889-2898.

[119] Williams D. Essential Biomaterials Science. Chap. 3. Cambridge, UK: Cambridge University Press; 2014..

[120] Raider SI, Flitsch R, Aboaf JA, et al. Surface oxidation of silicon nitride films. J Electrochem Soc; 1976, 123:560-565..

[121] . Rahaman MN, Boiteux Y, De Jonghe LC. Surface characterization of silicon nitride and silicon carbide powders. Bull Am Ceram Soc; 1986, 65:1171-1176..

[122] Bock RM, McEntire BJ, Bal BS, et al. Surface modulation of silicon nitride ceramics for orthopedic applications. Acta Biomater; 2015, 26:318-330..

[123] Gorth DJ, Puckett S, Ercan B, Webster TJ, Rahaman M, Bal BS. Decreased bacteria activity on Si(3)N(4) surfaces compared with PEEK or titanium. Int J Nanomedicine; 2012, 7: 4829–4840.

[124] Hisbergues M, Vendeville S, Vendeville P. Zirconia: Established Facts and Perspectives for a Biomaterial in Dental Implantology. J Biomed Mater Res B Appl Biomater; 2009, 88(2):519-29.

[125] A. G. EVANS E. A. CHARLES. Fracture Toughness Determinations by Indentation" Journal of the American Ceramic Society; 1976.

[126] Christel P, Meunier A, Dorlot J-M, Crolet J-M, Witvoet J, Sedel L, Boutin P. Biochemical compatibility and design of ceramic implants for orthopaedic surgery. Bioceramics: material characteristics versus in vivo behaviour. Ann NY Acad Sci; 1988, 523:234-2.

[127] Luthy H, Sharer P, Gaukler L. New materials in dentistry: Zirconia posts. Proc. 1993 Monte Verita BMS Conf., Ascona, CH; 1993, VI-2.

[128] P. Cardelli, E. Bigelli* , F. Balestra , M. Montani, M. Gallio, C. Arcuri. Types of cement for zirconia-ceramic crowns fixing: a review of the literature. UOC Odontostomatologia; 2012.

[129] Cranin AN, Schnitman PA, Rabkin SM, Onesto EJ. Alumina and zirconia coated vitallium oral endosteal implants in beagles. J Biomed Mater Res; 1975, 9:257-262.

[130] W.E. Lee e W.M. Rainforth, “Ceramic Microstructure - property control by processing”, Prima edizione, Chapman & Hall, London; 1994.

[131] J. R. Kelly e I. Denry Stabilized zirconia as a structural ceramic: An overview. Dental Materials; 2008, 24, 289-298.

[132] E.C. Subbarao, "Zirconia-an overview" In: "Science and technology of zirconia" A.H. Heuer and L.W. Hobbs, Editors, The American Ceramic Society, Columbus (OH); 1981.

[133] J.P. Goff, W. Hayes, S. Hull, M.T. Hutchings e K.N. Clausen. Defect structure of yttria-stabilized zirconia and its influence on the ionic conductivity at elevated temperatures. Phys Rev B; 1999, 59, 14202-19.

[134] A.G. Evans e A.H. Heuer. Review transformation toughening in ceramics: martensitic transformations in crack-tip stress fields. J Am Ceram Soc; 1980, 63, 241-8.

[135] BruxZir® Full-Strength vs. BruxZir® Anterior – Choosing Between Transformation Toughening and Light Transmission; Chairside Magazine; 2009, Vol 11, Issue 3.

[136] D.L. Porter e A.H. Heuer. Mechanisms of toughening partially stabilized zirconia (PSZ). J Am Ceram Soc; 1977, 60, 183-4.

[137] J. R. Kelly e I. Denry "Stabilized zirconia as a structural ceramic: An overview", Dental Materials; 2008, 24, 289-298.

[138] R.G. Garvie e P.S. Nicholson. Structure and thermomechanical properties of partially stabilized zirconia in the CaO– ZrO_2 system. J Am Ceram Soc; 1972, 55, 152- 7.

[139] J.P. Goff, W. Hayes, S. Hull, M.T. Hutchings e K.N. Clausen, Defect structure of yttria-stabilized zirconia and its influence on the ionic conductivity at elevated temperatures. Phys Rev B; 1999, 59, 14202-19.

[140] S. Fabris, A. Paxton e M.W. Finnis, "A stabilization mechanism of zirconia based. Acta Materialia; 2002, 50 (20), 5171-5178.

[141] Natalie R. Langley, Maria Teresa A. Tersigni-Tarrant Forensic Anthropology: A Comprehensive Introduction, Second Edition; CRC Press; 2017, 114-18.

[142] RESNICK D., KRANSDORF M. J., Imaging dell'apparato osteoarticolare, Bologna, Excerpta Medica Italia; 2005, pp. 50-51.

[143] Lynda F Bonewald. The Amazing Osteocyte. Journal of bone and mineral research: the official journal of the American Society for Bone and Mineral Research; 2011, 26(2):229-238.

[144] Danilo Alessio Di Stefano, Aurelio Cazzaniga, Chirurgia ossea ricostruttiva pre-e perimplantare, Elsevier Masson; 2008, 3-9.

[145] K. Sudarsanan, P. E. Machkie, R. A. Young; Comparison of synthetic and mineral fluorapatite, Ca5(PO4)3F, in crystallographic detail. Mater Res Bull; 1972, 7, 1331-8.

[147] L. Calderin, M. J. Stott; Electronic and crystallographic structure of apatites. Physical Review; 2003, B 67, 134106.

[148] M. Vallet-Regi, J. M. Gonzalez-Calbet; Calcium Phosphates as Substitution of Bone Tissues. Progress in Solid State Chemistry; 2004, 32, 1-31.

[149] R. Zapanta-LeGeros; Calcium phosphates in oral biology and medicine, Karger, New York, NY, USA; 1999, 15:1-201.

[150] J. C. Elliot; Structure and chemistry of the apatites and other calcium orthophosphates, Elsevier. Amsterdam, Netherlands; 1994, 43:652-656.

[151] N. Roveri, E. Foresti, M. Lelli, I. G. Lesci, M. Marchetti; Microscopic investigations of synthetic biomimetic hydroxyapatite. Microscopy: Science, Technology, Applications and Education; 2010, 3,1868-79.

[152] B. Palazzo, M. Iafisco, M. Laforgia, L. Bianchi, S. Mann, N. Roveri; Biomimetic hydroxyapatite-drug nanocrystals as potential bone substitutes with antitumor drug delivery properties. Advanced Functional Materials; 2007, 17 (13) 2180-2188.

[153] A. Tampieri, G. Celotti, E. Landi; From biomimetic apatites to biologically inspired composites. Analitical Bioanalitical Chemistry; 2005, 381, 568-576.

[154] M. Iafisco, B. Palazzo, M. Marchetti, G. Natile, M. Morpurgo, V. Gandin, C. Marzano, N. Roveri; Smart delivery of antitumoral platinum complexes from biomimetic hydroxyapatite nanocrystals, Journal of Material Chemistry; 2009, 19, 8385-8392.

[155] R. Zapanta-LeGeros; Calcium phosphates in oral biology and medicine, Karger, New York, NY, Monogr Oral Sc; USA; 1991,15:1-201.

[156] S. V. Dorozhkin and E. Matthias; Biological and medical significance of calcium phosphates, Angewandte Chemie International Edition; 2002, 41, 3130-3146, 2002.

[157] G. Daculsi, J. M. Bouler, R. Z. LeGeros, W. J. Kwang; Adaptive crystal formation in normal and pathological calcifications in synthetic calcium phosphate and related biomaterials. International Review of Cytolog; 1997, 172, 129-191.

[158] Th. Leventouri, A. Antonakos, A. Kyriacou, R. Venturelli, E. Liarokapis, V. Perdikatsis; Crystal structure studies of human dental Apatite as a function of age. Internatinal Journal of Biomaterials. (2009): 2009, P. 1155- 60 (Article ID 698547).

[159] A. Bigi, E. Boanini, C. Capuccini, and M. Gazzano; Strontium-substituted hydroxyapatite nanocrystals. Inorganica Chimica Acta; 2007, 360,1009-1016.

[160] N. K. Tripathy, P. N. Patel, and A. Panda, "Preparation, IR, and lattice constant measurements of mixed (Ca + Cu + Zn) hydroxylapatites. Journal of Solid State Chemistry; 1989, 80, 1-5.

[161] A. Bigi, E. Foresti, M. Gandolfi, M. Gazzano, and N. Roveri; Inhibiting effect of zinc on hydroxylapatite crystallization. Journal of Inorganic Biochemistry; 1995, 58, 49-58.

[162] S. V. Chiranjeevirao, J. Hemmerle, J. C. Voegel, and R. M. Frank; A method of preparation and characterization of magnesium-apatites. Inorganica Chimica Acta; 1982 67, 183-187.

[163] M. D. O'Donnell, Y. Fredholm, A. de Rouffignac, and R. G. Hill; Structural analysis of a series of strontium-substituted apatites. Acta Biomaterialia; 2008 4, 1455-1464.

[164] I. R. Gibson, S. M. Best, and W. Bonfield; Chemical characterization of siliconsubstituted hydroxyapatite. Journal of Biomedical Materials Research; 1999 44, 422-428.

[165] E. Fujii, K. Kawabata, K. Ando, K. Tsuru, S. Hayakawa, and A. Osaka; Synthesis and structural characterization of silica-hybridized hydroxyapatite with gas adsorption capability. Journal of the Ceramic Society of Japan; 2006, 114, 769-773.

[166] D. G. Nelson and J. D. Featherstone; Preparation, analysis, and characterization of carbonated apatites. Calcified Tissue International; 1982, 34 (2) S69-81.

[167] M. Vignoles, G. Bonel, and R. Young; Occurrence of nitrogenous species in precipitated B-type carbonated hydroxyapatites. Calcified Tissue International; 1987, 40, 64-70.

[168] J. Barralet, S. Best, and W. Bonfield; Carbonate substitution in precipitated hydroxyapatite: an investigation into the effects of reaction temperature and bicarbonate ion concentration. Journal of Biomedical Materials Research; 1998 41, 79-86.

[169] . T. Attin, B. Dumont, W. Buchalla; Fluoride uptake in caries, eroded and sound enamel after application of a 2000 ppm fluoride solution. Dtsch Zahnärztl Z; 2000: 55, P.455- 460..

[170] H. C. W. Skinner; Biominerals. Mineralogical Magazine; 2005, 69, 621-641.

[171] J. Elliott, D. Holcomb, R. Young; Infrared determination of the degree of substitution of hydroxyl by carbonate ions in human dental enamel. Calcified Tissue International; 1985, 3,7, 372-375.

[172] Sundgren JE, Bodö P, Lundström I. Auger electronspectroscopic studies of the interface between human tissue and implants of titanium and stainless steel. J Coll Int Sci; 1986, 110:9–20.

[173] Manicone PF1, Rossi Iommetti P, Raffaelli L. An overview of zirconia ceramics: basic properties and clinical applications. J Dent; 2007, 819-26.

[174] Pejeva E1, Papakoca K2, Ambarkova V3* and Todorovska G4 Marginal bone resorption at dental implant – RTG analysis; 2017, 94-118.

[175] M. Davarpanh, H.Martinez manulae di implantologia clinica. Elsevier; 1999, 31-35.

[176] Heitz-Mayfield LJ, Mombelli A. The therapy of peri-implantitis: a systematic review; 2014, 29 –45.

[177] Serino G, Turri A. Outcome of surgical treatment of peri-implantitis: results from a 2-year prospective clinical study in humans; Clin Oral Implants Res; 2011, 1214–20.

[178] Massimo Simon. Dental prosthesis conference; Milan; 2017.

[179] Luigi Canullo, David Peñarrocha Oltra, Marco Tallarico, Amparo Aloy Prosper. Surgical treatment of circumferential and semicircumferential defects due to periimplantitis: A prospective case series cohort study; 2007, 54-61.

[180] Fogh J., Fogh J.M., Orfeo T. One hundred and twenty-seven cultured human tumor cell lines producing tumors in nude mice. J Natl Cancer Inst; 1977, 59 (1): 221–226.

[181] Rodan S.B., Imai Y., Thiede M.A., Wesolowski G., Thompson D., Bar-Shavit Z., Shull S., Mann K., Rodan G.A. Characterization of a human osteosarcoma cell line (Saos-2) with osteoblastic properties. Cancer Res; 1987, 47 (18): 4961–6.

[182] Hausser H.J., Brenner R.E. Phenotypic instability of Saos-2 cells in long-term culture. Biochem. Biophys. Res. Commun; 2005, 333 (1): 216–22.

[183] McQuillan D.J., Richardson M.D., Bateman J.F. Matrix deposition by a calcifying human osteogenic sarcoma cell line (SAOS- 2). Bone; 1995, 16 (4): 415–26.

[184] Russell J. Fernandes, Michael A. Harkey, Maryann Weis, Jennifer W. Askew, and David R. Eyre The Post-Translational Phenotype of Collagen Synthesized by Saos-2 Osteosarcoma Cells. Bone; 2007, 40(5): 1343–1351.

[185] Czekanska E.M., Stoddart M.J., Richards R.G., J.S. Hayes, in search of an osteoblast cell model for in vitro research, EuropeanCells and Materials; 2012, 24: 1-1.

[186] Fernandes R.J., Harkey M.A., Weis M., Askew J.W., Eyre D.R. The post-translational phenotype of collagen synthesized by SAOS-2 osteosarcoma cells. Bone; 2007, 40: 1343-1351.

[187] Korting HC, Lukacs A, Vogt N, Urban J, Ehret W, Ruckdeschel G. Influence of the pH-value on the growth of Staphylococcus epidermidis, Staphylococcus aureus and Propionibacterium acnes in continuous culture; 1992, 78-90.

[188] D. Mack et al. Biofilm formation in medical device-related infection. Int. J. Artif. Organs; 2006, 29 343 –359.

[189] L. G. Harris and R. G. Richards. Staphylococci and implant surfaces: a review. Injury; 2006, 37 (Suppl. 1), S3 –S14.

[190] Michael Otto. Staphylococcus epidermidis the 'accidental' pathogen. Nat Rev Microbiol; 2009, 555–567.

[191] I. W. Sutherland. Biofilm exopolysaccharides: a strong and sticky framework; Microbiology. 2001 147 3 –9.

[192] C. Vuong and M. Otto. Staphylococcus epidermidis infections. Microbes. Infect; 2002, (4) 481 –489.

[193] P. S. Stewart and J. W. Costerton. Antibiotic resistance of bacteria in biofilms; Lancet, 2001, 358 135 –138.

[194] C.V. Raman, A new radiation, Indian J. Phys. 2; 1928, p.387.

[195] D.A. Long. Raman Spectroscopy. McGraw-Hill; 1977.

[196] Lewis – Edwards. Handbook of Raman Spectroscopy. Marcel Dekker Inc; 2001.

[197] Ivana Durickovic, Using Raman Spectroscopy for Characterization of Aqueous Media and Quantification of Species in Aqueous Solution, Intech; 2016, Chapter 19.

[198] A. Brillante, I. Bilotti, R.G. Della Valle, E. Venuti, A. Girlando, CrystEngComm; 2008, 10, 937-946.

[199] Ardalan Chaichi; Alisha Prasad Manas; Ranjan Gartia"Raman Spectroscopy and Microscopy Applications in Cardiovascular Diseases: From Molecules to Organs" Biosensors; 2008, 8, 107.

[200] Minsky M. Memoir on inventing the confocal scanning microscope, Scanning; 1988, 10: 128138.

[201] G.S. Kino, T.R. Corle. Confocal scanning optical microscopy and related imaging systems. Academic Press; 1996.

[202] R. Cozzi, P. Protti, T. Ruaro, “Analisi chimica strumentale – Metodi ottici; Zanichelli; 1997.

[203] W.D. Perkins, Fourier Transform-Infrared Spectroscopy. Part I: Instrumentation. Journal of Chemical Education; 1986, 63, A5.

[204] Bernard Valeu. Molecular Fluorescence Principles and Applications; 2001.

[205] Hermann Haken, Hans Christiph. Molecular Physics and Elements of Quantum Chemistry. 2002; 24-30.

[206] O.S. Wolfbeis. Anvanced Fluorescence Reporters in Chemisty and Biology III. Demchenko, Alexander P. (Ed.); 2011, 38-50.

[207] Sagar Aryal. Fluorescence Microscope- Principle, Instrumentation, Applications, Advantages, Limitations. 2018.

[208] Simon Gregersen. Flourescent peptide-stabilized silver-nanoclusters, a solid-phase approach for high-throughput ligand discovery. thesis Phd; 2004.

[209] Karen G. Porter Yvette S. Feig. The use of DAPI for identifying and counting aquatic microflora. Limnol. Oceanogr; 1980, 25(S), 943-948.

[210] Thermo Fisher Scientific. DAPI protocoll; 2017.

[211] Marker Gene Technologies. Inc; CFDA protocol; 2017.

[212] "Flow Cytometry Protocol for Analysis of Cell Viability using Propidium Iodide. Biomed. Phys. Eng; 2016, 34, 758-773.

[213] Thermo Fisher Scientific; protocol. Propidium Iodide; 2007.

[214] Eugenio Leonardo. Morfologia molecolare: principi generali di diagnostica e sistematica; 2007, 43-55.

[215] Peter V. HauschkaSteven A. Carr. Calcium-dependent .alpha.-helical structure in osteocalcin. Biochemistry; 1982; 2538-2547.

[216] Goldstein, G. I.; Newbury, D. E.; Echlin, P.; Joy, D. C.; Fiori, C.; Lifshin, E. Scanning electron microscopy and x-ray microanalysis. New York: Plenum Press 1981.

[217] Everhart, T. E.; Thornley, R. F. M. Wide-band detector for micromicroampere low-energy electron currents. Journal of Scientific Instruments; 1960, 37 (7): 246–248.

[218] Joseph Goldstein. Scanning Electron Microscopy and X-Ray Microanalysis 2003.

[219] C.S.Fadley. Basic Concepts of X-Ray photoelectron Spectroscopy, in Electron Spectroscopy, Theory, Techniques and Applications, Ed C.R.Brundle, A.D.Baker. Pergamon Press; 1978.

[220] Paul van del Heide. X-ray Photoelectron Spectroscopy: An introduction to Principles and Practices. Analytical Chemistry; 2012, 231-245.

[221] Siegfried Hofmann "Auger and X-Ray Photonelectron Spectroscopy. Materials Science; 2012, 5-20.

[222] Takimoto, K., Fukuta, A., Yamamoto, Y., Yoshida, N., Itoh, T., & Nonomura, S. Linear thermal expansion coefficients of amorphous and microcrystalline silicon films. Journal of non-crystalline solids; 2002, 299, 314-317.

[223] Tien, C. L., & Lin, T. W. Thermal expansion coefficient and thermomechanical properties of SiN x thin films prepared by plasma-enhanced chemical vapor deposition. Applied optics; 2012, 51(30), 7229-7235.

[224] Chen, H., Zhou, X., & Ding, C. Investigation of the thermomechanical properties of a plasma-sprayed nanostructured zirconia coating. Journal of the European Ceramic Society; 2003, 23(9), 1449-1455.

[225] Shin-ichi Kobayashi. IR Spectroscopic Study of Silicon Nitride Films Grown at a Low Substrate Temperature Using Very High Frequency Plasma-Enhanced. Chemical Vapor Deposition World Journal of Condensed Matter Phy sics; 2016, 6, 287-293.

[226] G. Scardera, T. Puzzer, G. Conibeer, and M. A. Green. Fourier transform infrared spectroscopy of annealed silicon-rich silicon nitride thin films. J. Appl. Phys; 2008, 104, 104310.

[227] K. Jhansirani, R.S. Dubey, M.A. More, Shyam Singh. Deposition of Silicon Nitride Films using Chemical Vapor deposition for Photovoltaic Applications; 2016, S2211-3797(16)30412-0.

[228] V. N. Antsiferov, V. G. Gilev, V. I. Karmanov. Infrared Spectra and Structure of Si_3N_4, Si2ON2, and Sialons. Refractories and Industrial Ceramics; 2003 44(2):108-114.

[229] Basahel SN, Ali TT, Mokhtar M, Narasimharao K. Influence of crystal structure of nanosized ZrO_2 on photocatalytic degradation of methyl orange; Nanoscale Res Lett. 2015, 18;10:73.

[230] Weifeng Li, Xuanyong Liu1, Anping Huang and Paul K Chu. Structure and properties of zirconia (ZrO_2) films fabricated by plasma-assisted cathodic arc deposition; J. Phys. D: Appl. Phys; 2007, (40), 2293–2299.

[231] D. Bersania, P. P. Lottici, G. Rangel, E. Ramos, G. Pecchi. R. Gómez, T. López. Micro-Raman study of indium doped zirconia obtained by sol–gel. Journal of Non-Crystalline Solids; 2004, Vol 345–346,p. 116-119.

[232] Naumenko, A. P., Berezovska, N. I., Biliy, M. M., & Shevchenko, O. V. Vibrational analysis and Raman spectra of tetragonal zirconia. Phys. Chem. Solid Stat; 2008, 9(1), 121-125.

[233] Katagiri, G. Direct determination by a Raman microprobe of the transformation zone size in Y2O3 containing tetragonal ZrO_2 polycrystals. Advances in ceramics; 1988, 24, 537-544.

[235] Honda, K., Yokoyama, S., & Tanaka, S. I. Assignment of the Raman active vibration modes of β-Si 3 N 4 using micro-Raman scattering. Journal of applied Physics; 1999, 85(10), 7380-7384..

[236] Andreas Zerr, Gerhard Miehe, George Serghiou, Marcus Schwarz, Edwin Kroke, Ralf Riedel, Hartmut Fueß, Peter Kroll & Reinhard Boehler. Synthesis of cubic silicon nitride. Nature; 1999, Vol 400, p. 340–342.

[237] J. Z. Jiang, Kenny Ståhl, Rolf W.Berg, P. X. Shi. Structural Characterization of Cubic Silicon Nitride. Europhys. Lett. 2007, 51(1):62.

[238] N. WADA, J. WONG, S. PROCHAZKA S.A. SOLIN. RAMAN AND IR ABSORPTION SPECTROSCOPIC STUDIES ON a, ~, AND AMORPHOUS Si_3N_4 Journal of Non-Crystalline Solids 43; 1981, 7-15.

[239] Alexander Bietsch. Electrical testing of gold nanostructures by conducting atomic force microscopy. Journal of Vacuum Science & Technology B: Microelectronics and Nanometer Structures Processing, Measurement, and Phenomena; 2000, 18, 1160.

[240] T. N. Wittberg, J. R. Hoenigman, W. E. Moddeman, C. R. Cothern, and M. R. Gulett. AES and XPS of silicon nitride films of varying refractive indices. Journal of Vacuum Science and Technology; 1978, 15, 348.

[241] Mark L. MillerRichard W. Linton. X-ray photoelectron spectroscopy of thermally treated silica (SiO2) surfaces.Anal. Chem; 1985, 57, 12, 2314-2319.

[242] P. E. Laibinis, C. D. Bain, R.G. Nuzzo, and G. M. Whitesides. 1995. Structure and Wetting Properties of w-Alkoxy-n-alkanethiolate Monolayers on Gold and Silver. J. Phys. Chem; 1999, 7663-7676.

[243] Yasuhiro Hara, Tomohiro Shimizu and Shoso Shingubara. Nitridation of Si surface at the bottom of submicron trench using nitrogen neutral beam. Japanese Journal of Applied Physics, 2015 Vol. 54, 6S1.

[244] Donley M.S. Baer D.R Stoebe T.G. Surface chemistry of silicon nitride powders: Electrokinetic behaviour and ESCA studies. Surf. Interface Anal. 1988; 11, 335.

[245] Yavor, Y., Goroshin, S., Bergthorson, J. M., & Frost, D. L. Comparative reactivity of industrial metal powders with water for hydrogen production. international journal of hydrogen energy; 2015, 40(2), 1026-1036.

[246] Shetty et al., "Raman spectroscopy: evaluation of biochemical changes in carcinogenesis of oesophagus," Br. J. Cancer; 2006, 94, 1460– 1464.

[247] S. Kolijenovic et al.," Detection of meningioma in dura mater by Raman spectroscopy," Anal. Chem; 2005, 77, 7958–7965.

[248] Francesco Boschetto, Elia Marin, Giuseppe Pezzotti. et al. Monitoring metabolic reactions in Staphylococcus epidermidis exposed to silicon nitride using i n s i t u timelapse Raman spectroscopy. Journal of Biomedical; 2018, Vol. 23(5).

[249] N.J. Klineand P.J. Treado,"Raman chemical imaging of breast tissue," J. Raman Spectrosc; 1997, 28, 119–124.

[250] Sandra Kloß et.al . Culture Independent Raman Spectroscopic Identification of Urinary Tract Infection Pathogens: A Proof of Principle Study. Anal. Chem; 2013, 85, 9610−9616.

[251] Giuseppe Pezzotti et al. Label-Free SERS Discrimination and In Situ Analysis of Life Cycle in Escherichia coli and Staphylococcus epidermidis. Biosensors; 2018, 8, 131.

[252] Pezzotti, G., McEntire, B. J., Bock, R., Boffelli, M., Zhu, W., Vitale, E., ... & Bal, B. S. Silicon nitride: a synthetic mineral for vertebrate biology. Scientific reports; 2.16, 6, 31717.

[253] Pezzotti, G. Silicon nitride: A bioceramic with a gift. ACS applied materials & interfaces; 2019, 11(30), 26619-26636.

[254] Pezzotti, G., Marin, E., Adachi, T., Lerussi, F., Rondinella, A., Boschetto, F., ... & Bock, R. M. Incorporating Si_3N_4 into PEEK to produce antibacterial, osteocondutive, and radiolucent spinal implants. Macromolecular bioscience. 2018, 18(6), 1800033.

[255] Unal, M., Jung, H., & Akkus, O. Novel Raman spectroscopic biomarkers indicate that postyield damage denatures bone's collagen. Journal of Bone and Mineral Research; 2016, 31(5), 1015-1025.

[256] De Gelder, J., De Gussem, K., Vandenabeele, P. & Moens, L. Reference database of Raman spectra of biological molecules. J. Raman Spectrosc; 2015, 38, 1133–1147.

[257] Giuseppe Pezzotti, Bryan J. McEntire, Ryan Bock, Wenliang Zhu, Francesco Boschetto, Alfredo Rondinella, Elia Marin, Yoshinori Marunaka, Tetsuya Adachi, Toshiro Yamamoto, Narisato Kanamura, and B. Sonny BalIn. In Situ Spectroscopic Screening of Osteosarcoma Living Cells on Stoichiometry-Modulated Silicon Nitride Bioceramic Surfaces. ACS Biomater. Sci. Eng; 2016, 2, 7, 1121-1134

[258] Jess, P. R. T.; Smith, D. D. W.; Mazilu, M.; Dholakia, K.; Riches, A. C.; Herrington, C. S. Early Detection of Cervical Neoplasia by Raman Spectroscopy. Int. J. Cancer; 2007, 121 (12), 2723−2728.

[259] Kast, R. E.; Serhatkulu, G. K.; Cao, A.; Pandya, A. K. Thakur, V. M.; Naik, R.; et al. Raman Spectroscopy Can Differentiate Malignant Tumors from Normal Breast Tissue and Detect Early Neoplastic Changes in a Mouse Model. Biopolymers; 2008, 89 (3), 235−241.

[262] Cheng W.T., Liu M.T., Liu H.N., Lin S.Y. Micro-Raman spectroscopy used to identify and grade human skin pilomatrixoma. Micrsc. Res. Tech. 2005: 68: 75–79.

[264] Stone, N.; Kendall, C.; Shepherd, N.; Crow, P.; Barr, H. NearInfrared Raman Spectroscopy for the Classification of Epithelial PreCancers and Cancers. J. Raman Spectrosc; 2002, 33 (7), 564−573.

[265] Penel G, Delfosse C, Descamps M, Leroy G. Composition of bone and apatitic biomaterials as revealed by intravital Raman microspectroscopy. Bone 2005; 36: 893-901.

[266] Ronen, S. M.; Stier, A.; Degani, H. NMR Studies of the Lipid Metabolism of T47D Human Breast Cancer Spheroids. FEBS Lett; 1990, 266 (1−2), 147−149.

[267] Naumann, D. Infrared and NIR Raman Spectroscopy in Medical Microbiology. Proc. SPIE 3257, Infrared Spectrosc. Proc. SPIE; 1998, 245−257.

[268] Hu, Y.; Shen, A.; Jiang, T.; Ai, Y.; Hu, J. Classification of Normal and Malignant Human Gastric Mucosa Tissue with Confocal Raman Microspectroscopy and Wavelet Analysis. Spectrochim. Acta, Part A; 2008, 69 (2), 378−82.

[269] Aksoy, C.; Severcan, F. Role of Vibrational Spectroscopy in Stem Cell Research. Spectroscopy; 2012, 27 (3), 167−184.

[270] Faoláin, E.Ó.; Hunter, M. B.; Byrne, J. M.; Kelehan, P.; McNamara, M.; Byrne, H. J.; Lyng, F. M. A Study Examining the Effects of Tissue Processing on Human Tissue Sections using Vibrational Spectroscopy. Vib. Spectrosc; 2005, 38 (1−2), 121−127.

[271] Stone, N.; Kendall, C.; Smith, J.; Crow, P.; Barr, H. Raman Spectroscopy for Identification of Epithelial Cancers. Faraday Discuss; 2004, 126 (0), 141−157.

[272] Lakshmi, R. J.; Kartha, V. B.; Murali Krishna, C.; Solomon, J. G. R.; Ullas, G.; Uma Devi, P. Tissue Raman Spectroscopy for the Study of Radiation Damage: Brain Irradiation of Mice. Radiat. Res; 2002, 157 (2), 175−182.

[273] Schulz, H.; Baranska, M. Identification and Quantification of Valuable Plant Substances by IR and Raman Spectroscopy. Vib. Spectrosc; 2007, 43 (1), 13−25.

[274] Calheiros, R.; Machado, N. F. L.; Fiuza, S. M.; Gaspar, A.; Garrido, J.; Milhazes, N.; Borges, F.; Marques, M. P. M. Antioxidant Phenolic Esters with Potential Anticancer Activity: A Raman Spectroscopy Study. J. Raman Spectrosc; 2008, 39 (1), 95−107.

[275] Orkoula, M. G. & Kontoyannis, C. G. Raman spectroscopy for the study of biological organisms (biogenic materials and biological tissues): a valuable analytical tool. Spectrosc. Europe; 2014, 26, 16–19.

[276] Morris, M. & Mandair, G. Raman assessment of bone quality. Clin. Orthop. Relat. Res; 2011, 469, 2160–2169.

[277] David R. Eyre1, MaryAnn Weis and Jyoti Rai. Analyses of lysine aldehyde cross-linking in collagen reveal that the mature cross-link histidinohydroxylysinonorleucine is an artifact. J. Biol. Chem; 2019, 294(38) 14163–14163.

[278] Oxlund H, Barckman M, Ortoft G, Andreassen TT. Reduced concentrations of collagen cross-links are associated with reduced strength of bone. Bone; 1995, 365S-371S.

[279] Vallet-Regi M and Navarette DA. Nanoceramics in clinical use: from materials to applications. 2nd ed. Cambridge: Royal Society of Chemistry; 2015.

[280] Wopenka B and Pasteris JD. A mineralogical perspective on the apatite in bone. Mater Sci Eng C; 2005, 25: 131–143..

[281] Nakamura M, Hiratai R, Hentunen T, et al. Hydroxyapatite with high carbonate substitutions promotes osteoclast resorption through osteocytelike cells. ACS Biomater Sci Eng; 2016, 2: 259–267.

[282] Eva Amenta, Helen E. King, Steven M. Tommasini and Carolyn M. Macica .Vibrational spectroscopic analysis of hydroxyapatite in HYP mice and individuals with X-linked hypophosphatemia. Ther Adv Chronic Dis; 2018, Vol. 9(12) 268 –281.

[283] McCreadie BR, Morris MD, Chen T-c, Rao DS, Finney WF, Widjaja E et al. Bone tissue compositional differences in women with and without osteoporotic fracture. Bone; 2006, 39:1190–1195..

[284] Penel, G., Delfosse, C., Descamps, M., Leroy, G. Composition of bone and apatitic biomaterials as revealed by intravital Raman microspectroscopy. Bone; 2005, 36, 893–901.

[285] McCreadie, B. R. et al. Bone tissue compositional differences in women with and without osteoporotic fracture. Bone; 2006, 39, 1190–1195.

[286] Legros, R., Balmain, N. & Bonel, G. Age-related changes in mineral of rat and bovine cortical bone. Calcif. Tissue Int; 1987, 41, 137–144 (1987).

[287] Mohamed Khalid, Tanujjal Bora, Ahmed Al Ghaithi, Sharanjit Thukral & Joydeep Dutta. Raman Spectroscopy detects changes in Bone Mineral Quality and Collagen Cross-linkage in Staphylococcus Infected Human Bone. Scientific Reports; 2018, 9417.

[288] Klein CPAT. Calcium phosphate implant materials and biodegradation. In: Academish Proefschrift. Vrije Universiteit te Ámsterdam; 1988.

[289] Davidenko N, Carrodeguas RG, Peniche C, Solís Y, Cameron RE. Chitosan/apatite composite beads prepared by in situ generation of apatite or Siapatite nanocrystals. Acta Biomaterialia; 2010, 6:466-76.

[290] Graham L. Cooper P.R. Cassidy N. Nor J.E. Sloan A.J. Smith A.J. The effect of calcium hydroxide on solubilisation of bio-active dentine matrix components. Biomaterials; 2006, 27, 2865.

[291] Taichi I. Yoshihiro S. Hidetaka K. Yasuhiko A. Satoru Y. SYNTHESIS AND CHARACTERIZATION OF HYDROXYAPATITECALCIUM HYDROXIDE FOR DENTAL COMPOSITE. Ceramics – Silikáty; 2011 55 (2) 123-126.

[292] Ossadnik, C., Vepřek, S., & Gregora, I. Applicability of Raman scattering for the characterization of nanocrystalline silicon. Thin Solid Films; 1999, 337(1-2), 148-151.

[293] Pezzotti, G., Marin, E., Adachi, T., Rondinella, A., Boschetto, F., Zhu, W., ... & Bal, S. B. Bioactive silicon nitride: A new therapeutic material for osteoarthropathy. Scientific reports; 2017, 7, 44848.

[294] Marin, E., Rondinella, A., Boschetto, F., Zanocco, M., McEntire, B. J., Bal, B. S., & Pezzotti, G. (2018). Understanding Silicon Nitride's Biological Properties: From Inert to Bioactive Ceramic. In Key Engineering Materials; 2018, Vol. 782, pp. 289-296.

[295] Pezzotti, G., McEntire, B. J., Bock, R., Boffelli, M., Zhu, W., Vitale, E., ... & Bal, B. S. (2016). Silicon nitride: a synthetic mineral for vertebrate biology. Scientific reports; 2016, 6, 31717.

[296] Zoch, M. L., Clemens, T. L., & Riddle, R. C. New insights into the biology of osteocalcin. Bone; 2006, 82, 42-49.

[297] Icer, M. A., & Gezmen-Karadag, M. The multiple functions and mechanisms of osteopontin. Clinical biochemistry; 2018, 59, 17-24.

[298] Dong, M., Jiao, G., Wang, Q. & Chen, Y. Biological silicon stimulates collagen type 1 and osteocalcin synthesis in human osteoblast-like cells through the BMP-2/Smad/RUNX2 signaling pathway. Biological trace element research; 2006, 173(2), 306-315.

[299] Jugdaohsingh, R Silicon and bone health. The journal of nutrition, health & aging; 2007, 11(2), 99.

[300] Arora, M., & Arora, E. The promise of silicon: bone regeneration and increased bone density. Journal of arthroscopy and joint surgery; 2017, 4(3), 103-105.

[301] Liu, X., Chu, P. K., & Ding, C. Formation of apatite on hydrogenated amorphous silicon (a-Si: H) film deposited by plasma-enhanced chemical vapor deposition. Materials chemistry and physics; 2007, 101(1), 124-128.

Acknowledgements

At the end of this journey that has allowed me to reach this goal, there are many people I would like to thank. Firstly, it is right to begin with those who have allowed this final work to be carried out and drafted. Professor Giuseppe Pezzotti, KIT referent, for my professional growth and the possibility to work for six months at the Kyoto Institute of Technology (Japan); Professor Alvise Benedetti, my supervisor at Ca' Foscari, for his availability.

Professor Elia Marin and PhD students Francesco and Matteo, for the support during my work and for the good times we spent together. Professor Zhu for helping me interpret the experimental results. In addition, together with them, I would like to thank the KIT students and all the people I met during my bike trips that made unique my life in Japan.

A sincere thank you is for old and new friends, who have always supported me giving me concrete help and also spending with me funny and nice moments.

The people who shared a stretch of road during my bike trip back from Japan: Mattia for having faced with me dangerous and dangerous moments and too strong uphill and my brother for not giving up.

To my girlfriend, Irene, for being close to me even from miles away, always proving to be a reference, bright and sunny.

Finally, to my parents and family for giving me a safe haven, to Anna and Angela, my two sisters, and Francesco, my brother, for a great future together.